



저작자표시-비영리-변경금지 2.0 대한민국

이용자는 아래의 조건을 따르는 경우에 한하여 자유롭게

- 이 저작물을 복제, 배포, 전송, 전시, 공연 및 방송할 수 있습니다.

다음과 같은 조건을 따라야 합니다:



저작자표시. 귀하는 원저작자를 표시하여야 합니다.



비영리. 귀하는 이 저작물을 영리 목적으로 이용할 수 없습니다.



변경금지. 귀하는 이 저작물을 개작, 변형 또는 가공할 수 없습니다.

- 귀하는, 이 저작물의 재이용이나 배포의 경우, 이 저작물에 적용된 이용허락조건을 명확하게 나타내어야 합니다.
- 저작권자로부터 별도의 허가를 받으면 이러한 조건들은 적용되지 않습니다.

저작권법에 따른 이용자의 권리는 위의 내용에 의하여 영향을 받지 않습니다.

이것은 [이용허락규약\(Legal Code\)](#)을 이해하기 쉽게 요약한 것입니다.

[Disclaimer](#)

공학박사학위논문

# **Mechanical and electrochemical degradation of Silicon anode for Li-ion batteries**

실리콘 음극재의 기계적 성능 및  
전기화학적 성능 저하에 관한 연구

2017년 2월

서울대학교 대학원

기계항공공학부

곽윤기



## **Abstract**

Silicon is one of a promising candidate for a conventional anode material of graphite to increase energy density as well as power density in LIB system. Silicon is abundant on earth and it has the ability to absorb large quantities of lithium. The theoretical electric capacity of Si is greater ten times than that of graphite. But a large amount of absorbed Li induces a large volume expansion which leads the fracture of silicon significantly. Consequently, the capacity degradation occurs within a few charge-discharge cycling.

In order to overcome this limitation and to enhance Si performance, experiment and simulation studies have been performed to understand the mechanics and kinetics of Si anode. For example, a variety of nanostructures of Si, such as nanowire, nanoparticle, and hollow nanoparticle have been developed and tested to enhance the mechanical stability. Furthermore, the electrochemical response of Si-based materials has been also studied extensively by assembling a half cell.

In computer-aided engineering (CAE) research, a chemo-mechanical model has been developed to analyze the internal stress evolution in host material during lithiation/delithiation process. And an electrochemical model was constructed to predict the electrochemical performance of Si anodes.

However, new phenomenon have been reported, and new technology has developed, advanced models are required to provide deeper insight into the mechanical and the electrochemical behavior of Si anode materials.

In this study, we suggest advanced models overcome the limitation of previous research and we investigate the mechanical and electrochemical degradation mechanisms of silicon anode material for lithium-ion batteries.

We first investigate the fracture behavior of crystalline silicon nanowires by combining of Li diffusion, larger deformation, and fracture mechanics. Based on the experimental observations, two phase Li diffusion model is employed to create a sequence of core-shell structures for the stress analysis. To account for large lithiation swelling, a chemo-mechanical model is constructed based on the nonlinear large deformation theory. We then analyze the fracture behavior of crystalline silicon nanowires by combining of a bilinear cohesive zone model. The crack is initiated from the surface of Si nanowires and it propagates to the center after the amount of Li inserted. Moreover, simulation results demonstrate that there is a critical size of the particle, below which fracture can be averted and there is a “safe state of charge (SOC)” depending on particle size.

Secondly, we investigate the electrochemical behavior of silicon anode material in Li-ion batteries within the multiscale framework because the

electrochemical performance of Si strongly depends on the interaction between atomic scale and microscale phenomena. In the atomic-scale, the stress-dependent energy barrier for the migration of lithium and the molar excess Gibbs free energy were calculated using density functional theory (DFT). In the micro-scale, we considered the coupled diffusion and large deformation model to determine the non-equilibrium cell potential. These simulation results demonstrate that the multi-scale model is consistent with experimental observations at different C-rates with constant diffusion coefficient.

Finally, we suggest an electrochemical degradation model with crack growth. This model is combined previous two modes including both the mechanical failure and the electrochemical response of the patterned Si. A crack in silicon is considered as the main reason for capacity reduction for lithium ion batteries due to the inhomogeneity of Li within the Si and the isolation of Si resulting from complete debonding. When Si size is large, a crack is formed in the silicon and it propagates during lithiation/delithiation, which hinders Li diffusion, resulting in the capacity loss. The mixed-mode failure is considered for the fracture behavior of the patterned Si and Butler-Volmer equation for electrode kinetics is used to obtain the cell's voltage and capacity. This study mainly investigates the relation between the electrochemical performance of LIB and the crack growth with taking into account the impacts of charge/discharge rate

condition.

Keyword: Lithium ion battery, Silicon anode, Diffusion induced stress, Cohesive zone model, Multi-scale model, Electrochemical response, Mechanical degradation.

Student Number: 2013-30768

# CONTENTS

## Abstract

## Chapter 1 Introduction 1

|  |   |
|--|---|
| 1.1 Lithium ion batteries overview             | 1 |
| 1.1.1 Lithium ion battery work principle       | 2 |
| 1.1.2 Degradation mechanism in LIBs            | 3 |
| 1.2 Silicon anode materials as novel electrode | 4 |
| 1.3 Scope and outline of the dissertation      | 5 |

## Chapter 2 Cohesive zone model for crack growth in a crystalline silicon anode material 8

|  |    |
|--|----|
| 2.1 Introduction   | 8  |
| 2.2 Methodology  | 11 |
| 2.2.1 Two phase diffusion in crystalline silicon         | 11 |
| 2.2.2 Large deformation theory in SiNWs                  | 13 |
| 2.2.2.1 Kinematics of multiplicative plasticity in SiNWs | 13 |
| 2.2.2.2 Elastic and flow plasticity in SiNWs             | 16 |
| 2.2.2.3 Mechanical equilibrium                           | 17 |
| 2.2.3 Cohesive zone model for crack propagation in Si    | 18 |
| 2.2.4 Boundary condition                                 | 21 |
| 2.3 Results and discussion                               | 22 |
| 2.3.1 Two phase Li diffusion                             | 22 |

|   |    |
|---|----|
| 2.3.2 Stress evolution in SiNWs (with cohesive zone, without cohesive zone) | 22 |
| 2.3.3 Crack propagation analysis in Si NWs                                  | 27 |
| 2.3.4 Size dependence fracture of Si NWs during lithiation                  | 28 |
| 2.4 Remarks   | 30 |

**Chapter 3 Multi-scale analysis of an electrochemical model including coupled diffusion, stress, and nonideal solution in a silicon thin film anode** 42

|   |    |
|---|----|
| 3.1 Introduction  | 42 |
| 3.2 Methodology   | 46 |
| 3.2.1 Multi-scale modeling of Li batteries                            | 46 |
| 3.2.2 Atomic-scale simulation of Li in Si                             | 47 |
| 3.2.2.1 Stress-dependent migration energy barrier for diffusion       | 48 |
| 3.2.2.2 The mixing enthalpy of amorphous $\text{Li}_x\text{Si}$ alloy | 50 |
| 3.2.3 Micro-scale simulation (diffusion and deformation)              | 52 |
| 3.2.3.1 Chemo-mechanical chemical potential                           | 52 |
| 3.2.3.2 Kinematics of large deformation                               | 54 |
| 3.2.4 Mesoscale simulation (Butler-Volmer kinetics)                   | 56 |
| 3.3 Results and discussion  | 60 |
| 3.3.1 Stress evolution (lithiation and delithiation)                  | 60 |
| 3.3.2 Atomic-scale simulation effects on Li diffusion                 | 61 |
| 3.3.3 Potential hysteresis  | 65 |
| 3.3.4 Comparison with experimental data                               | 67 |

|   |            |
|---|------------|
| 3.3.5 Comparison with the DIS model at different charge rates               | 69         |
| 3.4 Remarks   | 69         |
| <b>Chapter 4 Electrochemical response of patterned Si with crack growth</b> | <b>82</b>  |
| 4.1 Introduction  | 82         |
| 4.2 Methodology   | 84         |
| 4.2.1 Mixed-mode crack growth in the patterned Si                           | 84         |
| 4.2.1.1 Mixed-mode initiation criterion                                     | 84         |
| 4.2.1.2 Mixed-mode propagation criterion                                    | 86         |
| 4.2.1.3 Constitutive law  | 87         |
| 4.2.2 Li diffusion and crack's effect on the Li diffusion                   | 88         |
| 4.3 Results and discussion  | 89         |
| 4.3.1 Lithium distribution with & without the crack                         | 89         |
| 4.3.2 Debonding analysis during lithiation at different charge rate         | 90         |
| 4.3.3 Debonding analysis during delithiation at different charge rate       | 91         |
| 4.3.4 Time and state of charge to crack onset                               | 92         |
| 4.3.5 Crack length at different charge rate                                 | 92         |
| 4.3.6 Crack effects on the electrochemical response                         | 93         |
| 4.3.7 Breakthrough in the patterned Si                                      | 94         |
| 4.4 Remarks   | 95         |
| <b>Chapter 5 Conclusion</b>   | <b>110</b> |

|  |            |
|--|------------|
| <b>A. Appendix</b> .....   | 115        |
| A.1 Cohesive zone model for amorphous silicon (one phase diffusion) .. | 115        |
| A.2 Energy release rate partitions in cohesive zone model .....        | 117        |
| A.3 Effect of the shape of cohesive zone model .....                   | 119        |
| <br>   |            |
| <b>Bibliography</b>  | <b>126</b> |

## LIST OF FIGURES

|   |    |
|---|----|
| <b>Fig. 1.1</b> Schematic diagram of lithium ion battery cell, consisting of two electrodes and electrolyte .....   | 7  |
| <b>Fig. 1.2</b> Cracking of $\text{LiFePO}_4$ cathode material after 50 cycles and damage in $\text{LiCoO}_2$ cathode material .....  | 7  |
| <b>Fig. 2.1</b> Lithiation and cracking in a crystalline Silicon nanoparticle in situ TEM observation .....   | 32 |
| <b>Fig. 2.2</b> Schematic diagram of multiplicative decomposition of deformation gradient .....   | 33 |
| <b>Fig. 2.3</b> (a) Plot of the normal traction-separation relation, (b) bilinear CZM for the interfacial constitutive relations .....  | 34 |
| <b>Fig. 2.4</b> Radial Li distribution with a sharp phase boundary at different times during lithiation .....   | 35 |
| <b>Fig. 2.5</b> (a) Hoop stress evolution without cohesive zone and (b) hoop stress evolution with cohesive zone at selected time during lithiation in Si NWs ..  | 36 |
| <b>Fig. 2.6</b> Illustration of the two-phase lithiation in Si NWs with a structural evolution of pristine core (blue) and lithiated shell (red). (a) (1-5) evolution of hoop stress in a representative material element A without cohesive zone and (b) (1'-5') evolution of hoop stress in a representative material element A' with cohesive zone during lithiation ..... | 37 |
| <b>Fig. 2.7</b> Comparison of hoop stress evolution in a representative material element with/without cohesive zone model .....   | 38 |
| <b>Fig. 2.8</b> Relation between crack length and SOC of a c-Si NW with $R = 200\text{ nm}$ , phase lithiation in Si NWs with a structural evolution of pristine core (blue) and lithiated shell (red) .....  | 39 |

|  |       |
|--|-------|
| <b>Fig. 2.9</b> (a) Relation between the crack length and the SOC of a c-Si NW with different radius. (b) Plot of safe SOC at the onset of crack nucleation in c-Si of different radius .....  | 40    |
| <b>Fig. 2.10</b> Illustration of partially lithiated silicon nanowire, the pristine core Si acts as the mechanical backbone and electrical pathway for electrons .....   | 41    |
| <b>Fig. 3.1</b> Schematic of a multi-scale model of amorphous Si in a Li-ion battery .....   | 71    |
| <b>Fig. 3.2</b> (a) Migration energy barrier as a function of the internal stress field acting on the neighboring host atoms in the direction normal to diffusion. Tensile stress decreases the migration energy barrier, while compressive stress increases it. (b) Formation energy of a-Li <sub>x</sub> Si as a function of the molar fraction of Li at T = 0 K ..... | 72    |
| <b>Fig. 3.3</b> (a) Schematic of Si thin film. Biaxial stress evolution through the thickness of Si film for lithiation (b) and delithiation (c) at selected times ..  | 73    |
| <b>Fig. 3.4</b> Distributions of Li concentration: (a) Diffusion induced stress (DIS) model, (b) DIS coupled with stress-dependent migration energy barrier, (c) DIS coupled with concentration-dependent mixing enthalpy and (d) fully coupled model at short times (~250s) .....   | 74~75 |
| <b>Fig. 3.5</b> Time evolution of the distributions of Li concentration during lithiation for four models: (a) Diffusion induced stress (DIS) model, (b) DIS coupled with stress-dependent migration energy barrier, (c) DIS coupled with concentration-dependent mixing enthalpy and (d) fully coupled model .....  | 76~77 |
| <b>Fig. 3.6</b> Si electrode potential vs. capacity during lithiation and delithiation at a 1C rate for four different models .....  | 78    |

|  |         |
|--|---------|
| <b>Fig. 3.7</b> (a) Comparison of the multi-scale simulation result with the experimental data [95] for an a-Si thin film electrode (300nm) at C/8 (20.68 $\mu$ Ac <sub>m</sub> -2). And comparison of simulated curves (b) and the experiment results of Ref. [95] (c) corresponding to charge rates from C/2 to C/30 between 0 and 0.5 SOC ..... | 79~80   |
| <b>Fig. 3.8</b> Comparison of the DIS model with the multi-scale model at C/30, C/8, and C/2 between 0 and 0.5 SOC .....   | 81      |
| <b>Fig. 4.1</b> When there is a crack within the active material, the lithium needs to diffuse around the crack .....  | 96      |
| <b>Fig. 4.2</b> Mixed-mode delamination for the bi-linear traction-separation law  | 97      |
| <b>Fig. 4.3</b> Li distribution in a patterned Si during lithiation (a) and delithiation (b) .....   | 98      |
| <b>Fig. 4.4</b> The initial crack is present at the central and the surface of the patterned Si (a), Mode I and Mode II debonding variation at the central point and on the surface (b) ~ (d) .....  | 99~100  |
| <b>Fig. 4.5</b> During delithiation, Mode I (a) and Mode II (b) debonding variation and on the surface .....   | 101     |
| <b>Fig. 4.6</b> Time and SOC to crack onset at the central point with respect to the charge rate .....   | 102     |
| <b>Fig. 4.7</b> Crack length with respect to the charge rate: during lithiation (a), during delithiation (b) and during cycling (c) .....  | 103~104 |
| <b>Fig. 4.8</b> Electrochemical comparison of the patterned Si with different charge rate .....  | 105     |
| <b>Fig. 4.9</b> Capacity loss increases with a charge rate .....   | 106     |
| <b>Fig. 4.10</b> New shape of the patterned Si is proposed to overcome the identified drawbacks .....  | 107     |

|  |     |
|--|-----|
| <b>Fig. 4.11</b> Comparison of Mode I and Mode II debonding during lithiation, when there is a hollow space in the bottom or not .....   | 108 |
| <b>Fig. 4.12</b> Comparison of hollow structure model with “without crack” and “with crack” model .....  | 109 |
| <b>Fig. A1</b> (a) Radial Li distribution at selected time during lithiation in amorphous silicon, (b) corresponding hoop stress evolution .....   | 122 |
| <b>Fig. A2</b> Von-mises stress contours in the amorphous silicon nanowire of radius $R = 500 \text{ nm}$ , the crack is initiated from a center instead of a surface of nanowire and propagates toward the surface .....  | 123 |
| <b>Fig. A3</b> (a) Illustration of the embedded cohesive process zone, (b) Bilinear traction-separation constitution of cohesive zone model, it is composed of an intrinsic dissipation ( $G_{\text{int}}$ ) and an extrinsic dissipation ( $G_{\text{ext}}$ ) ..... | 124 |
| <b>Fig. A4</b> Variation of the shape of CZM according to the different shape factor .....   | 125 |
| <b>Fig. A5</b> The cohesive energy release rate as a function of lithiation time for $\Gamma = 0.11, 1, 1.67$ .....  | 125 |

## LIST OF TABLES

|  |    |
|--|----|
| <b>Table 3.1</b> Parameters used in modeling of Si thin film electrode ..... | 59 |
|--|----|



# Chapter 1

## Introduction

### 1.1 Lithium ion battery overview

A secondary electric battery is an electrochemical device to convert the chemical energy to electrical energy and vice-versa in a way of reversible process [1]. Among existing secondary batteries, lithium ion battery (LIB) have been widely used in electric power storage for mobile phones, laptop computers, ESS (Energy storage system), and EV (Electric vehicle) due to its large energy and high power density [2]. Especially, the utilization of Li-ion battery demands more for automobile applications in the future. Although modern electric vehicles are already being manufactured quite successfully, there are still challenges in order to be popular. For example, batteries with large energy density have to be developed to increase the driving range and the longer lifetime of battery system should be achieved in the automobile. Therefore, a variety of materials has been explored to

improve the performance of LIBs by means of experimental and simulation studies.

### 1.1.1 Lithium ion battery work principle

The lithium-ion battery consists of the anode as a negative electrode, the cathode as a positive electrode and electrolyte. The lithium ion participates in the relevant reaction. The electrolyte helps lithium ions move freely inside the battery as shown in Figure. 1.1. The anode has a large chemical potential of lithium relative to the cathode. Therefore, there is a driving force for lithium to transport from the anode to the cathode. The lithium in anode dissociates into lithium ion and electrons. By the potential difference between two electrodes, these lithium ions move from anode to the cathode, in the same time electrons go through the external electric circuit to maintain electroneutrality. Finally, they recombine within the cathode. The reproduced lithium resettle down between the original atomic structures of the cathode, which process is known as discharge. During the charging process, the external power source provides the electric energy that can this process is reversed.

The typical electrodes in a Li-ion battery are lithium graphite  $\text{Li}_x\text{C}_6$  with  $x$

ranging from 0 to 1, as an anode material and lithium manganese oxide  $\text{Li}_{1-x}\text{Mn}_2\text{O}_4$  as cathode material [3].

The reaction equation of above-mentioned material combination is



At the discharge process, lithium is oxidized at the graphite and reduced at the lithium manganese oxide.

### 1.1.2 Degradation mechanism in LIBs

Understanding of degradation mechanism in LIBs is essential to make durable LIBs. As expected for an electrochemical battery, a large part of this degradation mechanism is caused by nature of electrochemical reaction [4]. However, recently the mechanical degradation within active particles is also known to be reducing the lifetime of a Li-ion batteries. Some studies are focused on the interplay between diffusion and stress and mechanical failure within active particles. The fracture has been observed during cycling of a number of electrode materials, as shown in figure 1.2 [5, 6]. This mechanical failure ultimately results in isolating active particles and preventing Li diffusion within the active particle. Additionally unexpected

formation of solid electrolyte interphase (SEI) [7, 8] on newly opened surface of active particles reduces amount of available Li by side reactions with the electrolyte and prevents Li to reach the surface of the active particle, which results in increasing of electrical resistance in battery system [9, 10].

## **1.2 Silicon anode materials as novel electrode**

Fortunately, a number of candidate materials show better performance than conventional graphite that is a common anode material in lithium ion battery. For, example, silicon has a theoretical specific charge capacity that is ten times greater than the graphite [11-13]. However, during electrochemical lithiation, silicon undergoes large volume expansion up to ~ 320% leading to pulverization [14, 15]. As previously mentioned, this mechanical degradation results in the rapid capacity fade of silicon in a first few cycles and has been a bottleneck in commercializing silicon.

A Recent experiment shows that mechanical failure can be prevented by using nanostructured silicon anodes, such as nanoparticles, nanowires, hollow particles, and thin film [16-19]. These structures alleviate the stress by managing the

deformation. Unfortunately, a large surface to volume ratio in nano-size silicon inevitably forms worse SEI layer [20] and nanostructured silicon is expensive. Thus a fundamental understanding of the deformation, fracture, and electrochemical response in silicon is vital for the development of high-capacity lithium-ion batteries.

### **1.3 Scope and outline of the dissertation**

In this study, we seek a deeper understanding of the phenomena involving Li diffusion, deformation, fracture, the electrochemical response in silicon anode. It includes a thermodynamic description of Li transport in Si, a mechanical driving force for diffusion, chemical induced deformation, fracture mechanism, and electrochemical response.

In chapter 2, we investigate the fracture behavior of crystalline silicon nanowires by combining of Li diffusion, larger deformation, and fracture mechanics. Simulation results suggest a critical size of the particle, below which fracture can be averted and a “safe state of charge (SOC)” depending on particle size.

In chapter 3, we investigate the electrochemical behavior of silicon anode material in Li-ion batteries within the multiscale framework because the electrochemical performance of Si strongly depends on the interaction between atomic scale and microscale phenomena. These simulation results demonstrate that the multi-scale model is consistent with experimental observations at different C-rates with constant diffusion coefficient. Especially, a multi-scale model reflecting various phenomena should be considered at fast charge condition.

In chapter 4, we suggest an electrochemical degradation model with crack growth. This model is combined previous two modes including both the mechanical failure and the electrochemical response of Si. The mixed-mode failure is considered for the fracture behavior of Si film. This simulation permits us to study the effect of internal crack growth on the electrochemical performance at different charge rate.

In chapter 5, we conclude our work and give a quick outlook on how the model should be extended for future work.

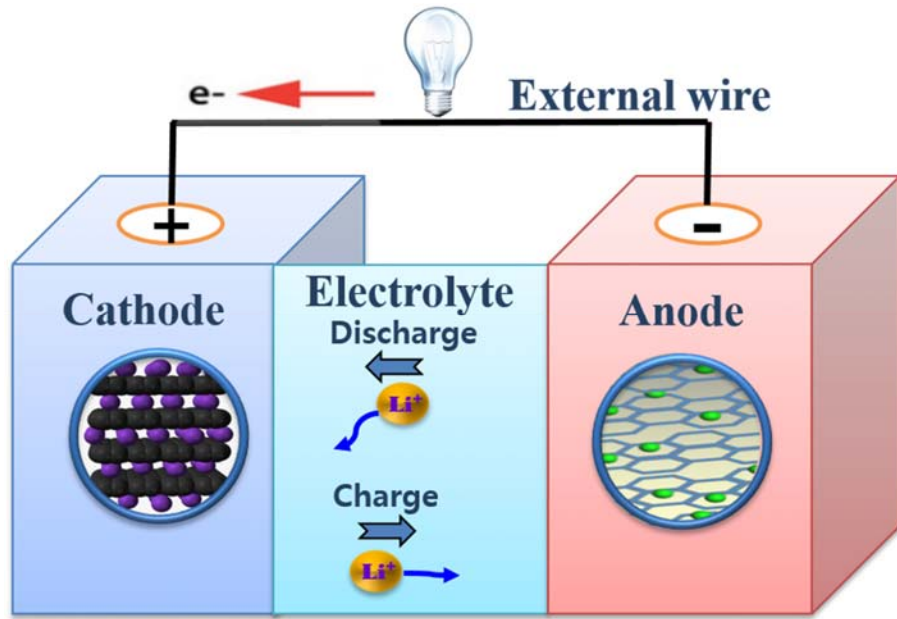


**Fig. 1.1** Schematic diagram of lithium ion battery cell, consisting of two electrodes and electrolyte.

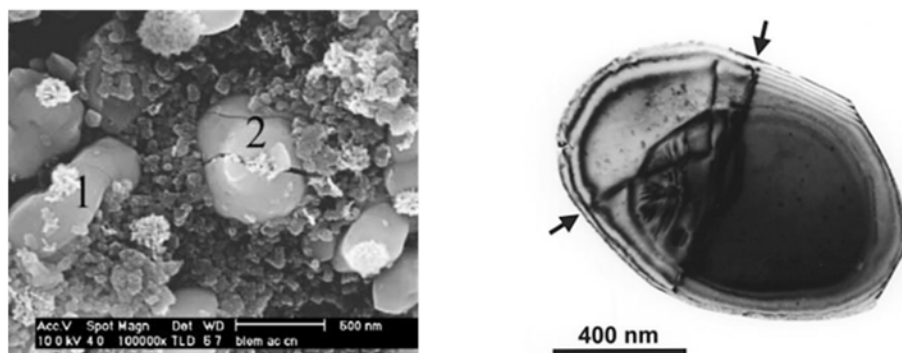


**Fig. 1.2** Cracking of LiFePO<sub>4</sub> cathode material after 50 cycles and damage in LiCoO<sub>2</sub> cathode material.

## **Chapter 2**

# **Cohesive zone model for crack growth in a crystalline silicon anode material**

### **2.1. Introduction**

Rechargeable lithium-ion batteries are widely used as electric power source for portable electronics and electric vehicles (EVs) due to its excellent characteristics such as improved cycle life and high energy density [21]. However, electronic isolation and unfavorable formation of unstable solid electrolyte interphase (SEI) on the cracked surface resulting from the active particle fracture is a potential degradation mechanism in lithium ion batteries. Massive volume expansion in active particle during the lithium insertion (lithiation) create the stresses which may induce cracking. Particularly silicon anode materials undergo volume changes of up to 310% due to very high theoretical reversible specific capacity (3579 mAh/g for  $\text{Li}_{15}\text{Si}_4$ ) at room temperature [12].

The Recent experiment reveals that lithiation in c-Si nanowires and nanoparticles is a two-phase reaction, with an atomically sharp phase boundary that separating the pristine c-Si core and the amorphous  $\text{Li}_{3.75}\text{Si}$  shell as shown in Fig. 2.1(a) [16, 22, 23]. There is a large lithium concentration gap between Li-poor (core) phase and Li-rich (shell) phase. Movement of phase boundary determines not only the local stress states at the phase boundary but also the stresses in materials behind the phase boundary [24, 25]. This effects on the fracture behavior caused by the development of tensile hoop stress in the surface layer as shown in Fig. 2.1(b).

In an effort to understand the stress evolution and fracture for crystalline Si, several authors have analyzed the stress evolution and deformation associated with interface reaction-controlled lithiation. Zhao et al. [26, 27] developed an analytical model to predict stresses and volume expansion of crystalline silicon during the lithiation. This study presents that the reaction is limited by the interface reaction rate and large plastic deformation of the lithiated silicon. Pharr et al. [28] developed a kinetic-based model for the anisotropic motion of phase boundaries by specifying phase boundary motion and computing morphology changes associated with lithiation, similar to those found experimentally. By adjusting the diffusivity

of lithium to simulate a sharp boundary, Yang et al. [29] also developed a model to show the anisotropic shape charges. In addition, McDowell et al. [30] have suggested a kinetics model account for the effect of stress on the interface reaction rate.

Going one step further, the diffusion induced model is used to investigate the critical condition under which electrode fracture is prevented. The crack nucleation condition of a pre-existing crack was investigated based on the linear elastic fracture mechanics [31, 32]. A modeling for finite deformation, diffusion, plasticity, and the fracture was described by Bower based on finite element method [33]. Peng Zuo. et al. [34] developed a phase field model to study coupling effect of diffusion-induced stress on the crack propagation in Si thin film.

In this study, we extend previous works on chemomechanical continuum model to have a deep insight into the diffusion-induced stress with fracture mechanism for crystalline silicon (c-Si) nanowires. A cohesive model of crack nucleation under diffusion-induced stresses in Si NWs developed to analyze the dynamic cracking behavior during lithiation. When the diffusion induced tensile stress exceeds the fracture threshold, a crack is initiated and propagate continuously inside the active particles. According to the morphology change, the stress distribution within the

active particle can be significantly affected. Moreover, we identify a critical electrode size to avoid crack nucleation under galvanostatic charging condition and we suggest a “safe state of charge (SOC)” depending on particle size.

## **2.2. Methodology**

Based on the experimental observations, we developed a coevolving model of Li diffusion and elastic-plastic deformation to account for both the evolution of a two-phase structure (Li-rich phase / Li-poor phase) and the large plastic deformation.

### *2.2.1 Two phase diffusion in crystalline silicon*

Two phase diffusion models are developed to create a sequence of core-shell structures for providing a basis of further stress analysis. It is noted that two-phase model is not a physical nature of dynamic lithiation due to lack of available material data for model calibration.

To simulate the phase evolution in lithiated SiNWs, a non-linear diffusion model is constructed. Li transport in Si is described by the classic diffusion equation in the entire domain in Eq. (2.1).

$$\frac{\partial c}{\partial t} = \nabla \cdot (D \nabla c) \quad (2.1)$$

where  $c$  is the concentration of Li which is normalized by the Li concentration at the fully lithiated state; namely,  $c = 0$  represents pure Si, while  $c = 1$  is  $\text{Li}_{3.75}\text{Si}$ , and  $D$  is the Li diffusivity.

To produce a sharp phase boundary, we assume Li diffusivity to be concentration dependent non-linear function in Eq. (2.2). From the free energy function of a regular solution,  $\psi = \alpha c(1-c) + [c \ln c + (1-c) \ln(1-c)]$ , diffusivity  $D$  in Eq. (2.2) can be derived according to a definition that can sharply raise diffusivity at the high Li concentration,  $D = -D_0 c d^2 \psi / dc^2$ .

$$D = D_0 [1/(1-c) - 2\alpha c] \quad (2.2)$$

where  $D_0$  is a diffusion constant and  $\alpha$  is a tunable constant to adjust the concentration profile near the interface [23]. This empirical concentration dependent diffusivity become small within the unlithiated Si core ( $c \approx 0$ ) and significantly large within the lithiated shell ( $c = 1$ ). To generate a numerically stable

core-shell structure, the diffusion properties are assigned as  $\alpha = 1.95$ ,  $D = 2.04 \times 10^{-17} \text{ (m}^2/\text{s)}$ . And we set  $D = D_{high} = 5 \times 10^{-9} \text{ (m}^2/\text{s)}$  to prevent numerical singularity associated with Li diffusion when the concentration at the  $\text{Li}_{3.75}\text{Si}$  is  $c \approx 1$ . The SiNWs are initially pristine and subjected to a constant Li flux  $I_0 = 6.75$  at the surface. Simulation for charging rate of  $I_0 = 13.5$  is also conducted to understand the charging rate effects.

### *2.2.2 Large deformation theory in SiNWs*

During the lithiation, SiNWs form a core-shell structure. The abrupt change of Li concentration at the phase boundary induces large chemical strains, consequently, the lithiated shell undergoes elastoplastic deformation [27].

#### *2.2.2.1 Kinematics of multiplicative plasticity in SiNWs*

To account for the lithiation induced large deformation of SiNWs, we adopt an elastic and perfectly plastic model. The kinematics for any material point in a continuum can be described by a continuous displacement field  $\mathbf{u}$  given by

$$\mathbf{u}(\mathbf{X}, t) = \mathbf{x} - \mathbf{X} \quad (2.3)$$

where  $\mathbf{u}$  is the displacement field,  $\mathbf{x}$  is the position of the material point at a time  $t$  in spatial configuration and  $\mathbf{X}$  is the initial position at  $t=0$  in reference configuration. The deformation gradient is defined as

$$\mathbf{F} = \frac{\partial(\mathbf{X} + \mathbf{u})}{\partial\mathbf{X}} = \mathbf{I} + \frac{\partial\mathbf{u}}{\partial\mathbf{X}} \quad (2.4)$$

In continuum mechanics, the large deformation flow theory of plasticity assumes that a multiplicative decomposition of the deformation gradient is typically based as

$$\mathbf{F} = \mathbf{F}^e \mathbf{F}^*, \quad \mathbf{F}^* = \mathbf{F}^p \mathbf{F}^c \quad (2.5)$$

where  $\mathbf{F}^c$  represents the compositional deformation gradient which is describing volumetric swelling (de-swelling) due to an insertion (extraction) of lithium in the silicon material with stress-free volume with a concentration of  $c$ .

$$\mathbf{F}^c = (J^c)^{1/3} \mathbf{I}, \quad J^c = 1 + \eta c \quad (2.6)$$

where  $J^c$ ,  $\mathbf{I}$ ,  $\eta$ ,  $c$  are the compositional Jacobian, identity tensor, coefficient of compositional expansion, and the molar concentration of lithium.  $\mathbf{F}^p$  and  $\mathbf{F}^e$  are the plastic and elastic part of the total deformation gradient respectively.  $\mathbf{F}^p$

represents a local irreversible plastic deformation such as the motion of dislocation.

$\mathbf{F}^e$  represents a subsequent elastic distortion of this swollen and plastic deformation. It is considering mapping of reference configuration to intermediate configuration by inelastic deformation  $\mathbf{F}^*$  and mapping of intermediate configuration to spatial configuration by  $\mathbf{F}^e$  as shown in Fig 2.2.

The total Jacobian,  $J = J^e J^p J^c = \det(\mathbf{F})$  also obeys multiplicative decomposition into the elastic part,  $J^e = \det(\mathbf{F}^e) > 0$ , plastic part  $J^p = \det(\mathbf{F}^p) > 0$ , and stress-free expansion part,  $J^c = \det(\mathbf{F}^c) > 0$ . In this study, we assume that plastic flow is incompressible, so that  $J^p = \det(\mathbf{F}^p) = 1$ , hence the total Jacobian is  $J = J^e J^c$ .

The velocity gradient in the spatial configuration from the above multiplicative decomposition can be obtained as

$$l = \nabla_x \mathbf{v} = \dot{\mathbf{F}}\mathbf{F}^{-1} = \dot{\mathbf{F}}^e\mathbf{F}^{e-1} + \mathbf{F}^e\dot{\mathbf{F}}^p\mathbf{F}^{p-1}\mathbf{F}^{e-1} + \mathbf{F}^e\dot{\mathbf{F}}^c\mathbf{F}^{c-1}\mathbf{F}^{e-1} = l^e + \mathbf{F}^e(\mathbf{L}^p + \mathbf{L}^c)\mathbf{F}^{e-1} \quad (2.7)$$

with  $l^e = \dot{\mathbf{F}}^e\mathbf{F}^{e-1}$ ,  $\mathbf{L}^p = \dot{\mathbf{F}}^p\mathbf{F}^{p-1}$ , and  $\mathbf{L}^c = \dot{\mathbf{F}}^c\mathbf{F}^{c-1}$ .

where  $\mathbf{L}^p$  is a plastic velocity gradient defined in an intermediate stress-free configuration (incompatible). The symmetric part of  $\mathbf{L}^p$  is the plastic rate of deformation,  $\mathbf{D}^p$  and the skew-symmetric part of  $\mathbf{L}^p$  is the plastic spin,  $\mathbf{W}^p$ .

$$\mathbf{D}^p = \frac{1}{2} \left[ \mathbf{L}^p + (\mathbf{L}^p)^T \right], \quad \mathbf{W}^p = \frac{1}{2} \left[ \mathbf{L}^p - (\mathbf{L}^p)^T \right] \quad (2.8)$$

It is widely assumed that the plastic flow is irrotational,  $\mathbf{W}^p = \mathbf{0}$  [35], then  $\mathbf{L}^p = \mathbf{D}^p$ .

#### 2.2.2.2 Elastic and flow plasticity in SiNWs

The elastic behavior in SiNWs can be measured using an elastic right Cauchy-Green deformation tensor

$$\mathbf{C}^e = (\mathbf{F}^e)^T \cdot \mathbf{F}^e \quad (2.9)$$

For finite plasticity, the symmetrized Mandel stress tensor is defined as

$$\mathbf{M}^e = \frac{1}{2} (\mathbf{C}^e \cdot \mathbf{S} + \mathbf{S} \mathbf{C}^e) \quad (2.10)$$

where  $\mathbf{S}$  is the second Piola-Kirchhoff stress.

The flow rule in terms of the plastic part of velocity gradient as

$$\mathbf{L}^p = \mathbf{D}^p = \dot{\lambda} \frac{\partial f}{\partial \mathbf{M}^e} \quad (2.11)$$

where  $\dot{\lambda}$  is a plastic strain rate constant and  $f$  is a yield function which describes the potential function governing plastic evolution that depends on Mandel stress tensor. The yield function with the perfectly plastic considered as

$$f(\mathbf{M}^e) = \sqrt{\frac{3}{2}(\mathbf{M}^e)^d : (\mathbf{M}^e)^d} - \sigma_Y = 0 \quad (2.12)$$

where  $(\mathbf{M}^e)^d$  is the deviatoric part of the  $\mathbf{M}^e$ ,  $\sigma_Y$  is the yield stress.

According to the Kuhn-Tucker condition, loading-unloading can be expressed as

$$\dot{\lambda} \geq 0, \quad f \leq 0, \quad \dot{\lambda} f = 0 \quad (2.13)$$

to which is appended the consistency condition  $\dot{\lambda} \dot{f} = 0$  when  $f = 0$ .

### 2.2.2.3 Mechanical equilibrium

As time required for the Li diffusion in the solid is much larger compared to

that required for the mechanical equilibrium, a kinematics of deformation can be considered as the quasi-static state at any time, i.e.

$$\nabla_{\mathbf{x}} \cdot \mathbf{P}(\mathbf{X}) = 0, \quad \nabla_{\mathbf{x}} \cdot \boldsymbol{\sigma}(\mathbf{X}) = 0, \quad \mathbf{P} = J\mathbf{F}^{-1} \cdot \boldsymbol{\sigma} \quad (2.14)$$

where  $\mathbf{P}$  is the first Piola-Kirchhoff stress tensor,  $\boldsymbol{\sigma}$  is the Cauchy stress tensor. In the spatial configuration. The boundary condition involves traction-free at the surface for mechanical equilibrium is given as

$$\mathbf{n} \cdot \boldsymbol{\sigma} = 0 \quad \text{on } S \quad (2.15)$$

where  $\mathbf{n}$  and  $S$  are the outward normal of the outer surface of the Si and Si outer surface respectively.

### 2.2.3 Cohesive zone model for crack propagation in Si

To characterize the fracture process in SiNWs, cohesive zone model is implemented using the finite element method. The idea of cohesive zones for modeling crack propagation was first introduced by Dugdale[36] and Barenblatt[37] in order to alternate singularity driven fracture approach, and was later adapted within a finite element framework by Needleman [38].

For the cohesive zone model, the interfacial potential is defined as

$$\Phi(\Delta_n, \Delta_t) = \Phi_n + \Phi_n \exp(-\Delta_n / \delta_n) \left\{ \begin{aligned} & \left[ 1 - r + \Delta_n / \delta_n \right] \left[ (1-q) / (r-1) \right] - \\ & \left[ q + [(r-q) / (r-1)] \Delta_n / \delta_n \right] \exp(-\Delta_t^2 / \delta_t^2) \end{aligned} \right\}$$

$$q = \frac{\Phi_t}{\Phi_n}, \quad r = \frac{\Delta_n^*}{\delta_n} \quad (2.16)$$

where  $\Phi_n$ ,  $\Phi_t$ ,  $\Delta_n$  and  $\Delta_t$  are work of normal and shear separation and normal and shear displacement jumps respectively.  $\delta_n$  and  $\delta_t$  are interface characteristic-lengths;  $\Delta_n^*$  is the value of  $\Delta_n$  after complete shear separation under the condition of normal tension being zero. [39]

From Eq. 2.16, the interfacial normal traction can be obtained as

$$T_n = \frac{\partial \Phi}{\partial \Delta_n} = - \left( \frac{\Phi_n}{\delta_n} \right) \exp \left( \frac{-\Delta_n}{\delta_n} \right) \left\{ \left( \frac{\Delta_n}{\delta_n} \right) \exp \left( \frac{-\Delta_t^2}{\delta_t^2} \right) + \left[ \frac{(1-q)}{(r-1)} \right] \left[ 1 - \exp \left( \frac{-\Delta_t^2}{\delta_t^2} \right) \right] \left( r - \frac{\Delta_n}{\delta_n} \right) \right\}$$

$$\Phi_n = \sigma_{\max} \delta_n \exp(1) \quad (2.17)$$

With  $\Delta_t = 0$ , the normal traction relation is shown in Fig. 2.3.

In this study, we assume the bilinear CZM for the interfacial constitutive relations. Cohesive zone elements are zero-thickness elements that are used to mesh regions where the material degrades monotonically towards complete failure

to advance the crack. Figure 2.3(b) presents a schematic of the linear softening traction-separation law that was used in our simulation. CZM is described by two independent parameters, cohesive energy,  $G_{ic}$  and either of the cohesive strength  $N_s$  or the complete separation length  $\delta^f$ . A cohesive zone model relates the separation length ahead of a crack tip to the traction  $T$  that resists to the fracture. The initial portion of the line is linear-elastic up to the damage initiation length,  $\delta^0$ . Beyond the damage initiation length, damage accumulates within the cohesive zone in an irreversible manner, while their stiffness linearly decreases to zero, until the complete separation,  $\delta^f$  is reached. Complete delamination of the cohesive interface is considered when there is not effective traction at the interface vanishes. The area beneath the traction-separation law represents the surface energy of the material, which is equal to the cohesive energy,  $G_{ic}$  required to propagate a crack. In bilinear softening assumption, the initial response of the cohesive zone is linear until a damage initiation criterion is satisfied. The penalty stiffness  $K$  of the bilinear traction-separation law is defined as

$$K = \frac{N_s}{\delta^0} \quad (2.18)$$

The irreversible bilinear softening constitutive behavior for Mode I loading is defined as

$$T = \begin{cases} K\delta, & \delta < \delta^0 \\ (1-d)K\delta, & \delta^0 < \delta < \delta^f \\ 0, & \delta \geq \delta^f \end{cases} \quad (2.19)$$

$$d = \frac{\delta^f (\delta - \delta^0)}{\delta (\delta^f - \delta^0)}$$

In order to prevent interpenetration of the crack face, additional condition is introduced as  $T = K\delta$ ,  $\delta \leq 0$

#### 2.2.4 Boundary condition

Initial boundary conditions are set as follows: the initial value of concentration on the SiNWs is zero at  $t = 0$  to simulate the charging process. For the stress analysis, the free stress boundary condition and undeformed state are taken as the initial state. The governing equation is solved using COMSOL Multiphysics via the general PDE modes and structure mode.

## **2.3. Results and Discussion**

### *2.3.1. Two phase Li diffusion*

Figure 2.4 shows the representative results of radial Li distribution with a sharp phase boundary using Eq. (2.2). As Li fluxes from the surface, the phase boundary moves toward the center. Since this study is focused on the rate-dependent limit of elastic and perfectly plastic deformation, the movement of phase boundary forms the particle surface to its center increase.

In diffusion simulation, the normalized Li concentration behind the phase boundary quickly attains slightly below 1 (Fully lithiated), while those ahead of the phase boundary layer remain nearly zero. The Li concentration changes abruptly at the interface. This sharp phase boundary is consistent with experimental observation.

### *2.3.2. Stress evolution in SiNWs (with cohesive zone, without cohesive zone)*

In the current work, in order to account for the changes in the elastic modulus of crystalline silicon as it is alloyed, we adopted Li concentration dependent material properties such as Young's modulus based on the Density Functional

Theory calculations studied by Shenoy et al [40]. The material properties used in the simulations are as follows:  $E_{Si} = 185 \text{ GPa}$ ,  $\nu_{Si} = \nu_{Li_xSi} = 0.22$ ,  $\sigma_{Y,Si} = 7 \text{ GPa}$ ,  $E_{Li_xSi} = 35 \text{ GPa}$ ,  $\sigma_{Y,Li_xSi} = 1 \text{ GPa}$  [30].

We assumed that the lithiation strain induced by the insertion of Li is isotropic dilatational in all directions, (e.g.,  $(r, \theta, z)$  directions) in a cylindrical coordinate system. The lithiation expansion coefficients are  $\beta_r = \beta_\theta = \beta_\phi = 0.26$  is assumed to yield a lithiation volume increase by 100% because the physical assignment of lithiation is not yet possible due to the lack of experimental measurement [24]. As the phase boundary passed, the material undergoes elastic and or plastic deformation. Plastic strain is governed by the  $J2$  flow rule based on the Mises yield criterion, and the simulation use traction-free boundary conditions.

Hoop stress evolution without cohesive zone corresponding to the Li concentration profile in Fig. 2.4 are presented in Fig. 2.5(a). At the beginning of lithiation, high compressive hoop stress is generated within the lithiated phase due to the large difference in volume change between c-Si and  $Li_xSi$ . The Si core experience homogenous tensile hoop stress that increase in magnitude as lithiated. Further lithiation, the core is subjected to compressive hoop stress because of the buildup of hoop tension in the surface layer. While the hoop stress near the surface

become less compressive and becomes tensile, which is induced by “push-out” effect as a result of the volume expansion of newly lithiated material near the phase boundary [24, 26]. Additionally, the hoop stress in the shell at the interface is more compressive than in the core because the volume increase in the shell is constrained by the unlithiated Si core.

In order to investigate the fracture effects on the stress, we compare these results to those obtained when the fracture have been neglected. Figure 2.5(b) shows hoop stress evolution with a cohesive zone within the silicon nanowire during lithiation. Only Mode I is considered since most cracks propagate perpendicular to the diffusion direction. The hoop stresses before cracking due to the Li diffusion shows similar results. However, the tensile hoop stresses along the fracture surface are released after crack initiation. Eventually, hoop stresses are vanished, which indicates complete debonding. The most salient feature is the development of tensile hoop stress at the phase boundary in the late stage of lithiation ( $t \approx 20s$ ). Such hoop tension results from the normal cohesive traction at the crack tip. Another important contribution is that the overall stress states are much lower when considering the fracture in Si NWs.

To understand the stress generation in physical phenomena, we present the evolution of the hoop stress at representative elements, **A** (without cohesive zone) and **A'** (with cohesive zone), i.e.,  $r = 160\text{nm}$  in Fig. 2.6. Here the phase boundary is described by a sharp interface between pristine core (blue) and growing lithiated shell (red). The shell is assumed to be fully lithiated with a maximum Li concentration. The lithiation strain is generated mainly near the core-shell interface, where the Li concentration change abruptly.

Hoop stresses at the element **A** versus time curve show the hoop stress evolution during lithiation in Fig. 2.6(a). At the beginning of lithiation, the newly lithiated layer at the phase boundary expands more toward the surface than toward the center. The larger area in the hoop direction at longer radial distance produces this asymmetric expansion which generates the hydrostatic tension in element **A** located within the pristine core part as shown in stage (1). As the phase boundary approaches to the element **A**, an additional dilatational lithiation strain restrained by surrounding materials develops local compressive stresses, so that element **A** experiences tensile elastic unloading, compressive elastic loading sequentially in stage (2). When the reaction takes place in element **A**, compressive plastic yielding occurs in the hoop direction as represented by stage (3). As the phase boundary

crosses the element A, newly lithiated strain in inner part continuously pushes out the element A in outward radial direction, simultaneously it leads to the hoop stretch in this element. Therefore, the representative element undergoes compressive elastic unloading in stage (4). Further lithiation, the element A experiences tensile elastic loading and tensile plastic yielding, which correspond to stage (5). It is important that this tensile hoop stress explains the surface cracking in Si NWs as observed in in-situ experiments.

In the case of with cohesive zone as shown in Fig. 2.6(b), the representative element A' exhibits similar behavior before initiation of crack (1'-2'). When the reaction takes place in element A', it shows relatively low compressive stress due to the crack propagation from the surface in stage (3'). This compressive stress also becomes tensile as the phase boundary approaches to the center (4'). In particular, the hoop tensile stress at the representative element with cohesive zone dramatically decrease during crack propagation and then it becomes zero after the complete fracture (5').

In order to explore the hoop stress within the cohesive surface in details, the evolution of the hoop stress at the radius = 160 nm of the Si NW with respect to the lithiation time is plotted in Fig. 2.7. Under two cases, one of which (the green

solid line) is plotted without cohesive zone surface in Si NW, the another one (the red dashed line) is plotted with cohesive zone surface. Hoop stress at the both representative elements increases gradually with lithium concentration in each case at the initial stage. When the reaction takes place in the representative element, tensile hoop stress quickly becomes compressive stress. This is obvious that the compressive hoop stress in element **A'** with the cohesive zone is lower than that in the element **A** without the cohesive zone because the stress is relaxed by the initiation of the crack at the surface as discussed above. Further lithiation changes this compressive stress to tensile stress by the “push-out” effect. At the late stage of lithiation, in contrast to high tensile stress in the element **A**, the magnitude of tensile stress of element **A'** decreases and become zero.

### *2.3.3 Crack propagation analysis in Si NWs*

Figure 2.8 shows the evolution of the concentration, phase boundary movement and crack length for nanowire of radius  $R = 200\text{ nm}$  according to the lithiation time. Recent experiments have revealed that the cracking of c-Si nanoparticles, nanopillars, and nanowires occurs during lithiation [16, 41, 42]. And in-situ TEM experiments show that once a crack is initiated at the surface, it grows rapidly to

the center [29, 30]. This behavior was consistent with our cohesive zone model. During early stage lithiation, a crack does not occur because the development of high compressive stress at the surface does not provide the driving force for fracture and Si could sustain tensile stress due to the strength of internal bonds. However, the increasing tensile hoop stress on the external curved surface of the lithiated region leads to fracture of nanowire during continuous lithiation. The crack is initiated at  $t = 15s$  and fast crack growth is observed towards the center of the particle. But, as the crack approach to the phase boundary, the crack growth velocity decrease. This is because that a neighboring compressive stress at the phase boundary influences on the crack growth behavior.

#### *2.3.4 Size dependence fracture of Si NWs during lithiation*

Recent studies show that improved cyclic performance and reduction in the capacity fade are achieved using nanoscale materials which have the capability to accommodate large stress without any crack during lithiation. In nanoscale structures, the mechanical failure is mitigated by managing the deformation patterns through geometric restrictions and shape and size optimization [43-45]. To investigate the critical size of nanowire below which there is not crack growth or

the growth is too small to measure, we perform simulations with varying the radius, whose results are shown in Fig. 2.9(a) First, the particle radius is 200nm. For the other four cases, the radius decreases as 150nm, 100nm, 80nm, 50nm respectively. One can observe that the smaller radius is the larger attainable SOC, before the crack is initiated and below the radius of 50nm, the fracture can be completely mitigated. In Fig. 2.9(b), safe SOC is plotted for different radius of Si NWs. For the nanowire with a radius of  $R = 200\text{nm}$ , the safe SOC is 0.58. While the nanowire with a radius of  $R = 50\text{nm}$  sustain upon full lithiation.

When the lithium is inserted within a safe range of SOC depending on the radius, the electrochemical response and the cyclability of the battery will be improved because the core Si acts as the mechanical backbone for electrode material and the electrical pathway for electrons from the substrate to the lithiated Si.

When we compare our results with the statistical experimental results taken from [46], where they reported that critical diameter for fracture of crystalline Si pillar is between 150nm and 200nm. There are several reasons why the critical sizes obtained from experiment and simulation is different. First, 2D simulation cannot reflect experimental conditions identically, for example, the plane strain assumption in 2D model neglect geometric constraints, while nanopillars used in

the experiment are fixed to the substrate. Secondly, the lower fracture energy is considered in our model. When we consider the fracture energy release rate as  $G_{lc} = 14.9(\text{J}/\text{m}^2)$  in ref [47], the estimated critical size will increase. Moreover, a different electrochemical reaction rate is considered. Si NWs in the simulation are lithiated for tens of seconds, whereas Si nanopillars are lithiated for 10 hours. The electrochemical reaction rate is a significant factor in a diffusion induced modeling for fracture analysis. Since our works provide an intuitive guideline regarding a safe SOC according to the nanowire size, it contributed to the development of durable, high-capacity anodes for advanced lithium ion battery.

## **2.4. Remarks**

Based on large deformation theory and cohesive zone model, the chemo-mechanical continuum model is constructed to investigate the stress evolution and dynamic cracking behavior in crystalline silicon (c-Si) nanowires during lithiation. The developed large hoop tensile on the surface of nanowire induces the crack which propagates to the center and relaxes the internal stress comparing to the model without cohesive zone. But, as the crack approach to the phase boundary, the crack growth velocity decrease. This is because that a neighboring compressive

stress at the phase boundary influences on the crack growth behavior. Moreover, we identify a critical electrode size to avoid crack nucleation under galvanostatic charging condition and we suggest a “safe state of charge (SOC)” depending on particle size. Below critical radius of  $\sim 50\text{nm}$ , the silicon particle can sustain without fracture, which is having reasonable agreement with experimental observations. In addition, when the lithium is inserted within a safe range of SOC depending on the radius, the electrochemical response and the cyclability of the battery will be improved because the core Si acts as the mechanical backbone for electrode material and the electrical pathway for electrons from the substrate to the lithiated Si. Therefore, it is necessary to understand stress evolution and fracture behavior of silicon anodes for the development of high-performance LIBs.

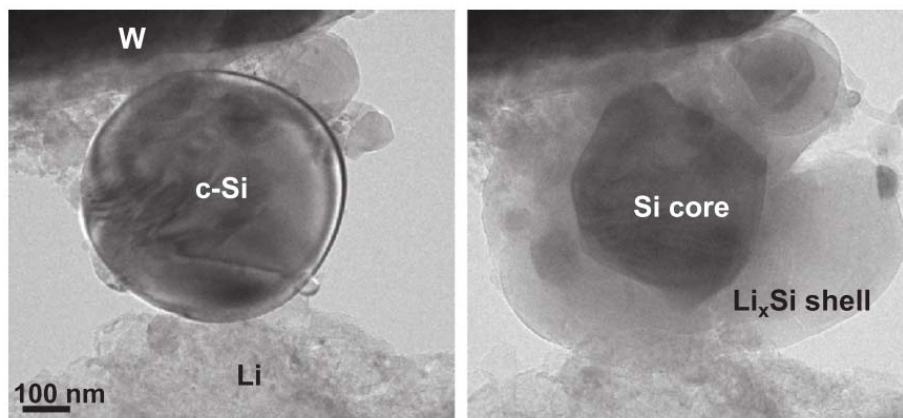


**Fig. 2.1** Lithiation and cracking in a crystalline Silicon nanoparticle in situ TEM observation

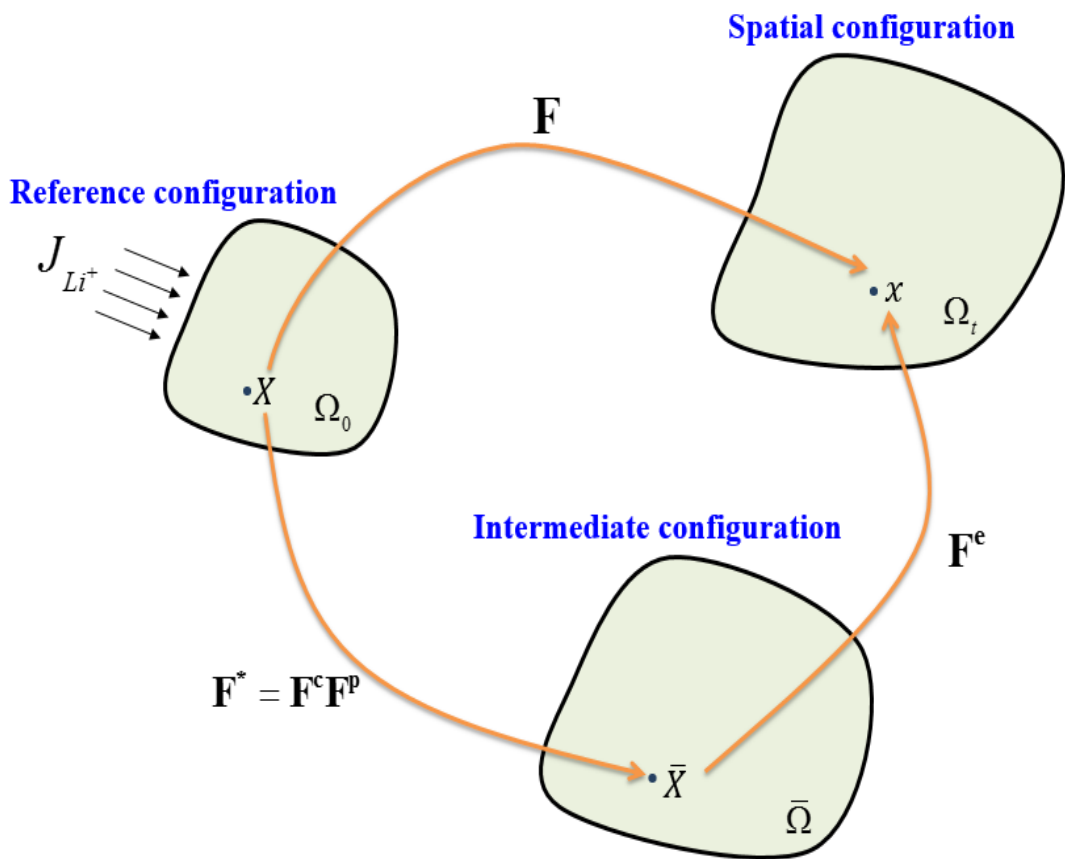
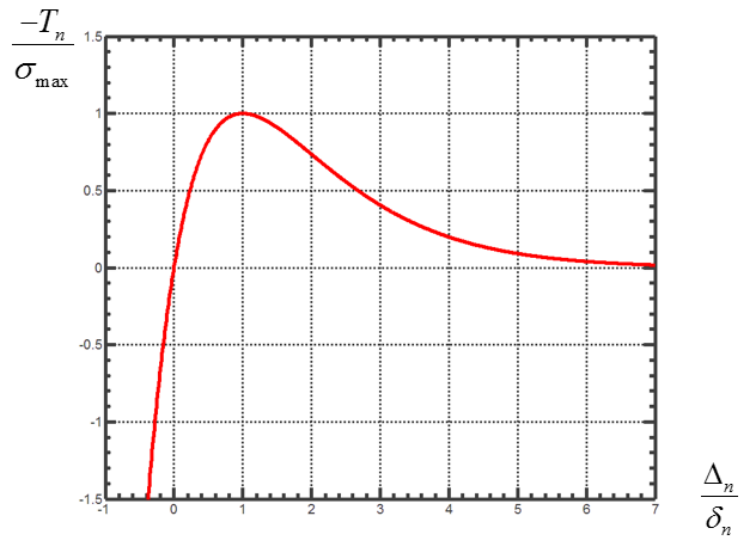


**Fig. 2.2** Schematic diagram of multiplicative decomposition of deformation gradient

**(a)**



**(b)**

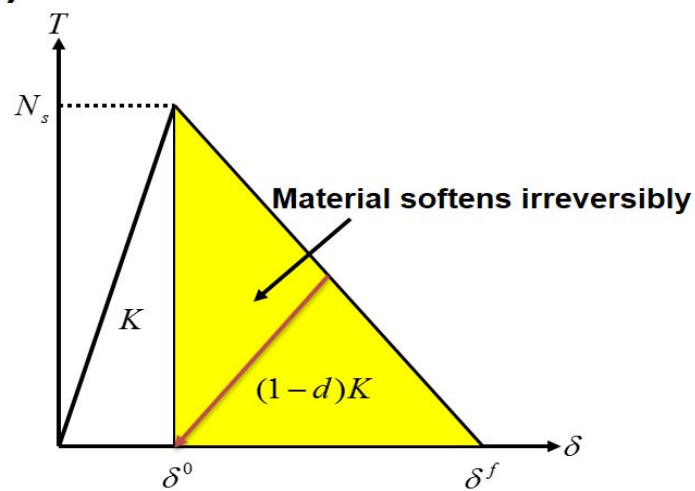


**Fig. 2.3** (a) Plot of the normal traction-separation relation, (b) bilinear CZM for the interfacial constitutive relations

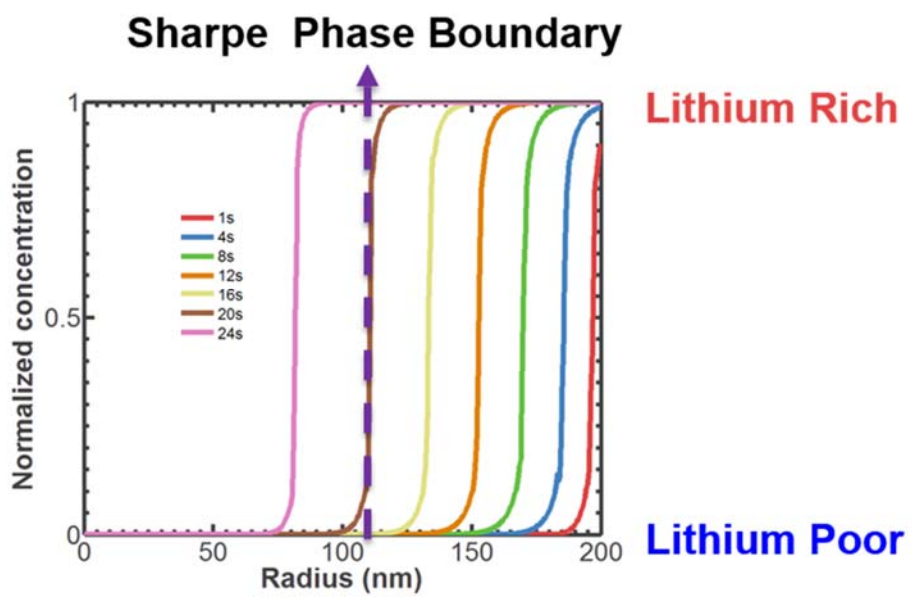


**Fig. 2.4** Radial Li distribution with a sharp phase boundary at different times during lithiation

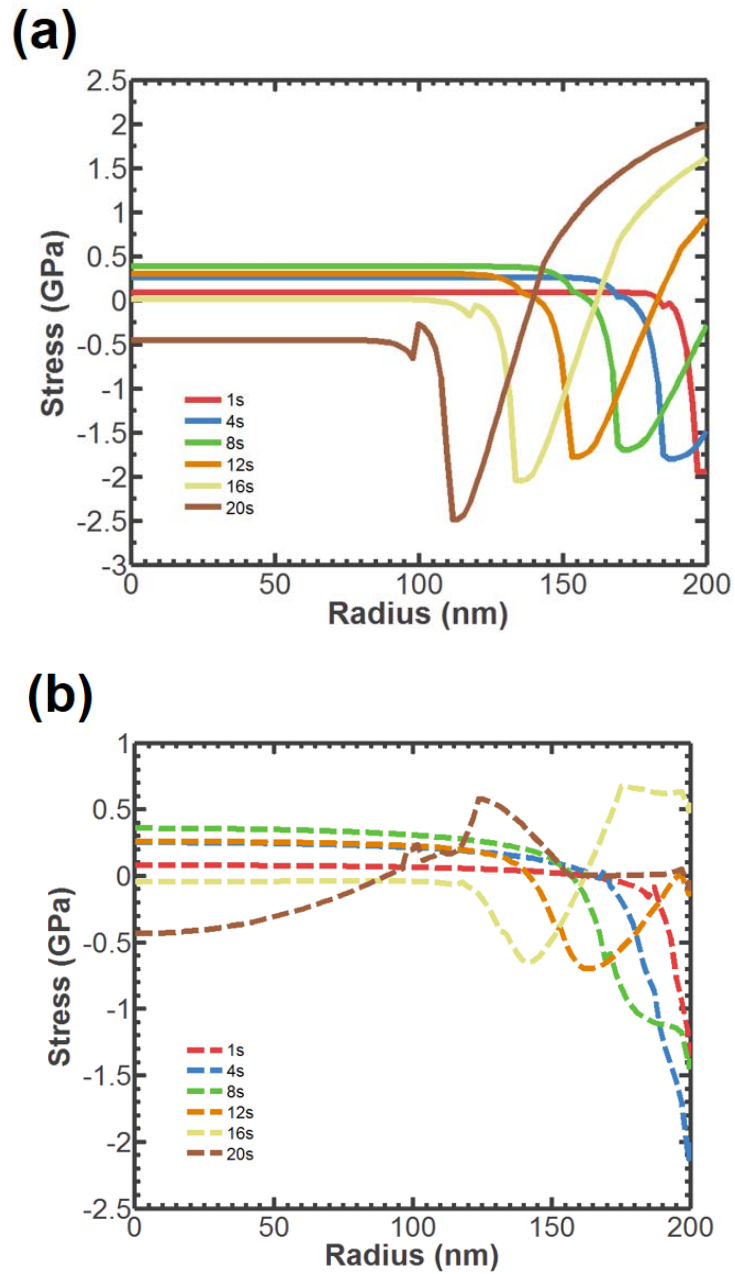


**Fig. 2.5** (a) Hoop stress evolution without cohesive zone and (b) hoop stress evolution with cohesive zone at selected time during lithiation in Si NWs

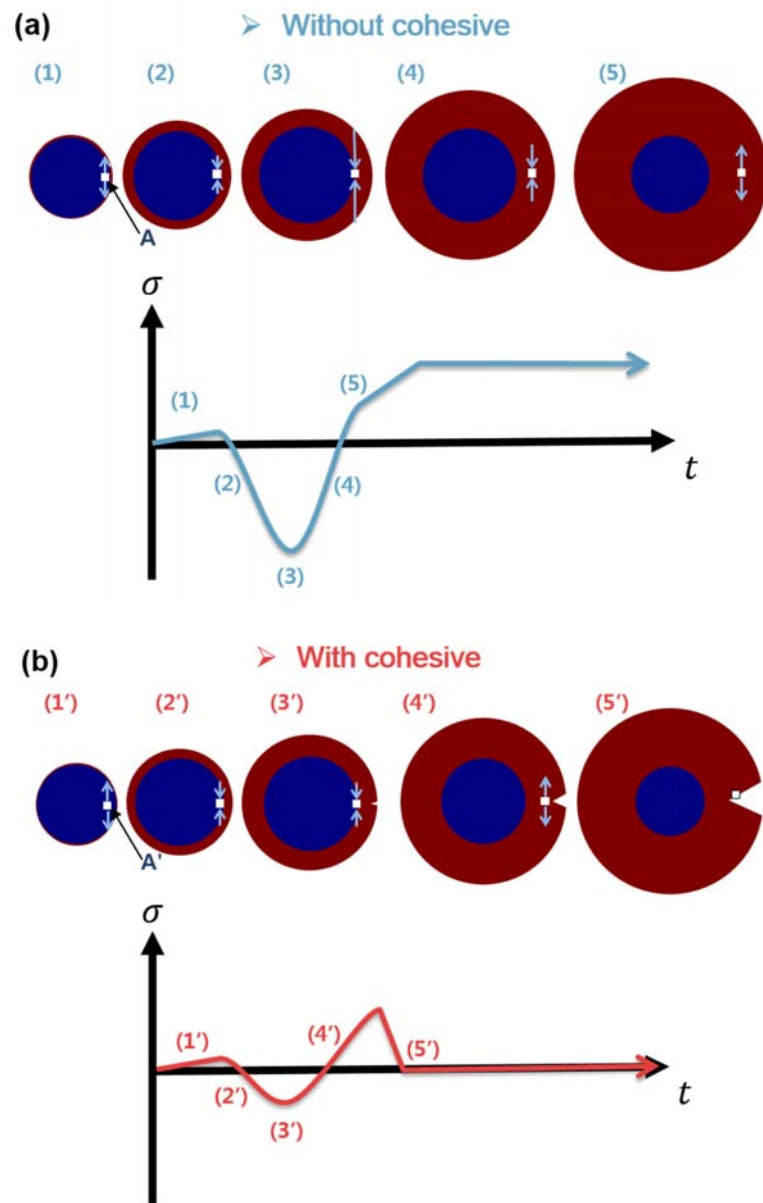


**Fig. 2.6** Illustration of the two-phase lithiation in Si NWs with a structural evolution of pristine core (blue) and lithiated shell (red). (a) (1-5) evolution of hoop stress in a representative material element A without cohesive zone and (b) (1'-5') evolution of hoop stress in a representative material element A' with cohesive zone during lithiation

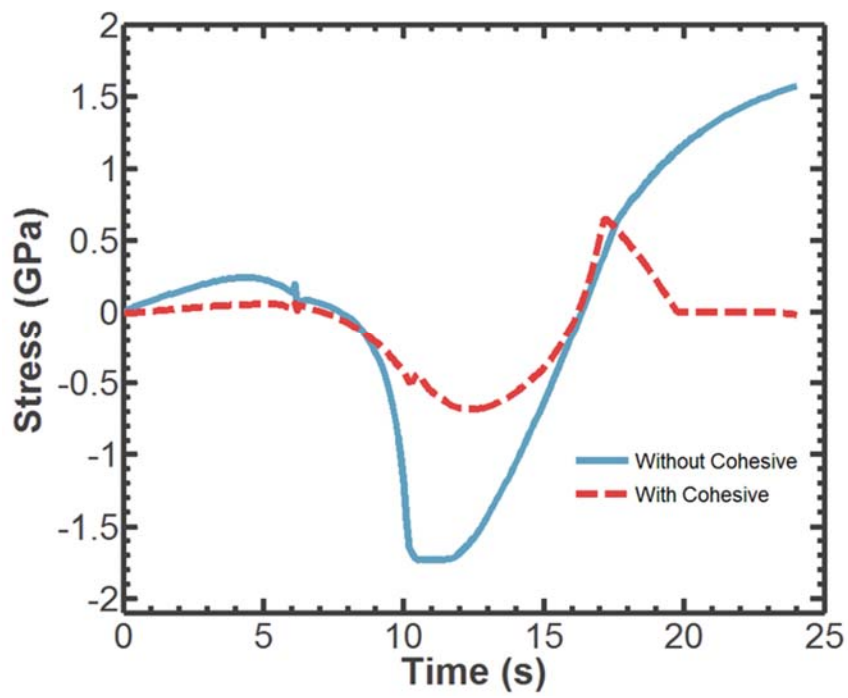


**Fig. 2.7** Comparison of hoop stress evolution in a representative material element with/without cohesive zone model

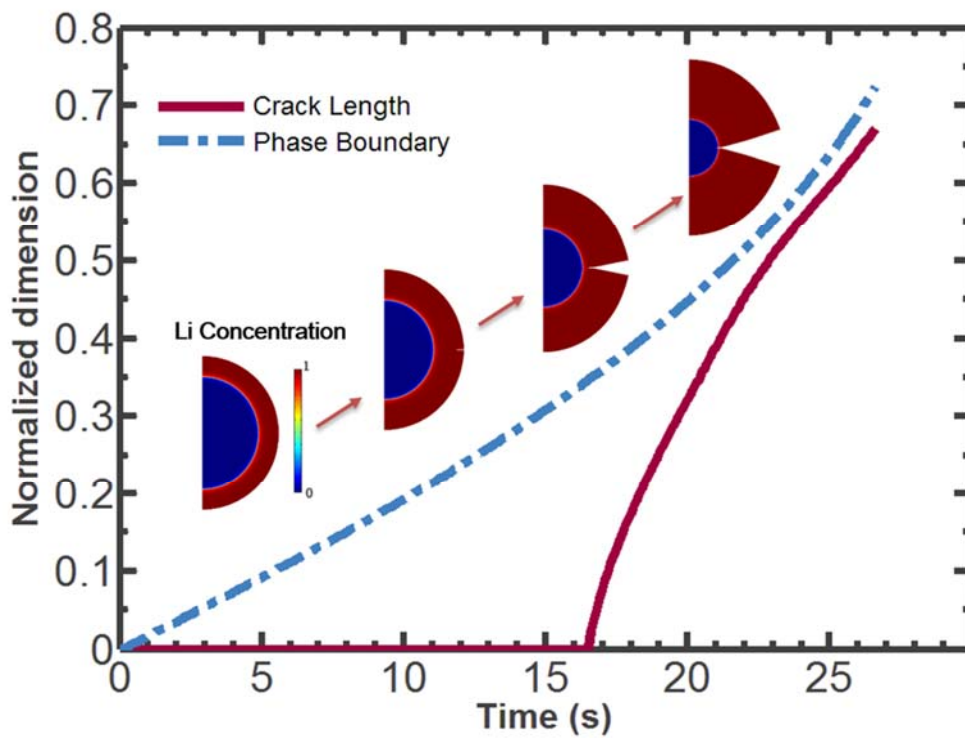


**Fig. 2.8** Relation between crack length and SOC of a c-Si NW with  $R = 200 \text{ nm}$ . phase lithiation in Si NWs with a structural evolution of pristine core (blue) and lithiated shell (red)

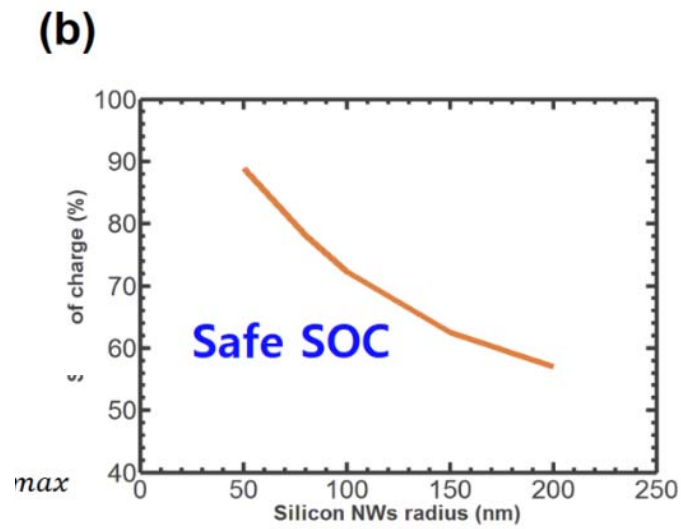
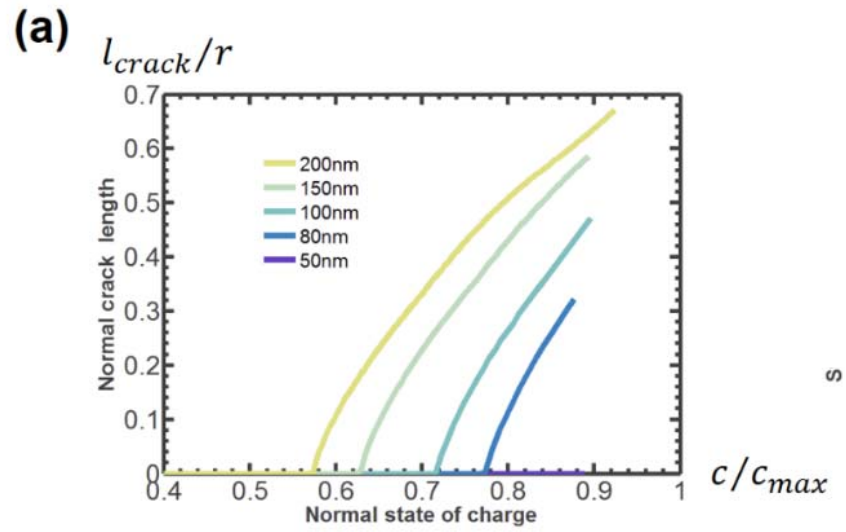


**Fig. 2.9** (a) Relation between the crack length and the SOC of a c-Si NW with different radius. (b) Plot of safe SOC at the onset of crack nucleation in c-Si of different radius

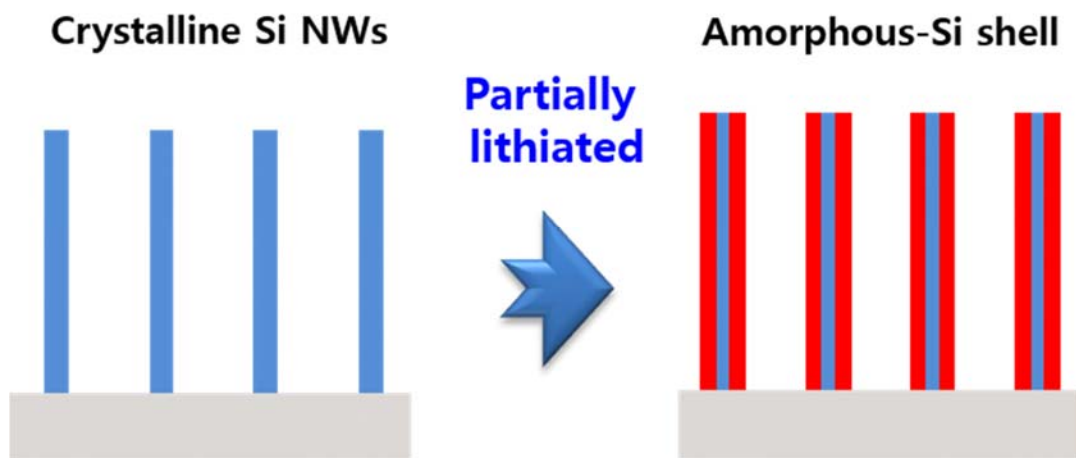


**Fig. 2.10** Illustration of partially lithiated silicon nanowire, the pristine core Si acts as the mechanical backbone and electrical pathway for electrons

## Chapter 3

# Multi-scale analysis of an electrochemical model including coupled diffusion, stress, and nonideal solution in a silicon thin film anode

### 3.1 Introduction

Silicon has attracted much attention in the development of high-energy-density Li-ion batteries (LIBs) for use in energy storage systems (ESS) and electric vehicles (EV) [48, 49]. Compared to the conventional carbon-based anode, amorphous silicon (a-Si) shows a remarkable ability to absorb Li ( $3580 \text{ mAhg}^{-1}$ ), forming  $\text{Li}_{3.75}\text{Si}$  [11, 50]. This high absorption capacity, however, causes undesirable volume expansion that results in the mechanical pulverization of electrodes [51, 52]. As a consequence, electrodes can fracture, triggering electrical contact loss and the formation of a solid electrolyte interface (SEI) on the fractured

surface. This result eventually leads to a significant irreversible capacity loss [8, 53]. This loss is one of the main drawbacks for the commercial use of Si as an anode material in LIBs. Many strategies have been proposed to reduce this large electrochemically related stress so that the cycle performance of the Si anode can be improved. In particular, nanostructured Si materials such as nanowires, nanotubes, nanofilms and porous structures have been studied to enhance the mechanical stability of Si anodes by managing deformation patterns through geometric restrictions and shape optimizations [18, 54, 55].

In addition to experimental studies, theoretical work has been carried out to understand the kinematics of large deformations during lithiation/delithiation [28, 42, 56, 57]. Zhao et al. [58] proposed a reactive flow model that considers the concurrent non-equilibrium process of the Li insertion reaction and the plastic flow of electrodes. Recently, Bower et al. [59] proposed a theory involving finite deformation, diffusion, plastic flow, and electrochemical reactions. First-principles calculations were conducted to gain a better understanding of the electrochemical kinetics and deformation from a fundamental perspective. The kinetics of Li insertion into a-Si has been investigated by Moon et al. [60, 61]. Moon et al. reported the concentration-dependent diffusivity of Li in  $\text{Li}_x\text{Si}$  compounds. Shenoy

et al. calculated mechanical properties such as Young's modulus, shear modulus, and Poisson's ratio that show elastic softening during lithiation. Shenoy et al. explained that elastic softening occurs due to structural evolution that causes the formation of weak Li-Si bonds from strong Si-Si covalent bonds [62]. Several other models have been developed for which various aspects of Li-ion cell behavior have been reported [63-66]. Most previous battery cell models employed the classic Fick's second law to describe Li transport in battery systems. Fick's second law is a reasonable approximation to fit experimental observations of potential versus capacity [67]. Potential profiles of high charge rate (C-rate) conditions, however, have shown large discrepancies between model predictions and experimental data. Existing models simply fail to describe accurately the physical phenomena that actually occur. Jagannathan et al. incorporated charge rate-dependent diffusion coefficients in the classic Fick's law model in an attempt to overcome these issues. This model, however, is not a physics-based model and neglects important physical phenomena such as diffusion-induced stress, concentration-dependent material parameters, and Li-Si mixing enthalpy. These properties must be taken into account to describe the variation of potential hysteresis [68]. For this reason, multi-scale physical modeling techniques need be considered to provide a deeper insight into a physics-based battery model that properly describes material behavior. The

continuum theory of diffusion-induced stress should be extended to an atomic-scale analysis in which the local thermodynamic interactions between Li and Si influence macroscopic mechanical behavior.

Therefore, the objective of this study is to propose a multi-scale model to characterize the electrochemical and mechanical response of a-Si thin film. In a multi-scale framework, the diffusion-induced stress (DIS) model [69] on a cell-scale includes atomic-scale effects of internal stress on the migration energy barrier and concentration-dependent mixing enthalpy. These effects contribute significantly to the nonlinear distribution of Li concentration. In order to investigate these atomic-scale physical and chemical effects on the overall Li diffusion and discharge/charge potential hysteresis, we split the multi-scale model into four different models: (1) diffusion-induced stress (DIS) model, (2) DIS coupled with stress-dependent migration energy barrier, (3) DIS coupled with concentration-dependent mixing enthalpy, and (4) DIS coupled with all of these effects. Each of these models was analyzed for individual atomic-scale effects. We then demonstrated that our multi-scale analysis was quantitatively consistent with the experimental observations of Si thin film at different C-rates. The results show that the macroscopic kinetics of silicon anode materials in Li-ion batteries are

highly affected by the stress induced by lithiation/delithiation, and the mixing formation energy of  $\text{Li}_x\text{Si}$ .

## **3.2 Methodology**

### 3.2.1 Multi-scale modeling of Li batteries

The electrochemical performance of Si-based materials depends on the interaction between atomic-scale and micro-scale phenomena that occur at the electrodes [70]. The electrochemical reaction of Li with Si occurs on a nanometer-scale. This reaction, of course, depends on the molar fraction of each reactant and their mixing energies. Li transfer and the mechanical deformation of the host material, however, depends on the physical properties of each material. The mechanisms for the manifestation of these are strongly and nonlinearly coupled over the nano and micro scales, which affects the macroscopic behavior of LIBs [71].

Figure. 3.1 shows a multi-scale model of a LIB. In the atomic-scale simulation (sub-nanoscale diagram), the migration energy barrier to lithium diffusion and the excess molar Gibbs free energy representing a deviation from an ideal solution

were calculated using density functional theory (DFT). We incorporated the results of the atomic-scale simulation into the continuum model (microscale model) that accounts for the diffusion-coupled elastic-plastic deformation in the cell-scale (mesoscale). In the mesoscale model, we determined the non-equilibrium cell potential as a function of surface lithium concentration using Butler-Volmer kinetics.

### 3.2.2 Atomic-scale simulation of Li in Si

Ab-initio calculations were performed using the DFT method with generalized gradient approximation (GGA) [72, 73]. We used the projector augmented wave (PAW) method with a plane wave basis set as implemented in the Vienna Ab-initio Simulation Package (VASP) [74]. The valence configuration for Li ( $1s^2 2s^1$ ) and Si ( $3s^2 3p^2$ ) were employed. The energy cutoff for the plane wave basis set was kept fixed at a constant value of 500 eV. A k-point mesh in the Monkhorst-Pack scheme was set to  $3 \times 3 \times 3$ . The amorphous Si structure contained 64 Si atoms with periodic boundary conditions. The geometries of  $\text{Li}_x\text{Si}$  ( $0 \leq x \leq 4$ ) were optimized using the conjugated gradient method until the residual forces on constituent atoms become smaller than  $0.01\text{eV}/\text{\AA}$ . For the ab initio molecular dynamics simulation, the k-

point was only sampled at the gamma point. Amorphous structures of  $\text{Li}_x\text{Si}$  were made using the ab initio MD (AIMD) simulation avoiding crystalline configurations at 2200 K. A time step of 3.0 fs, and overall simulation steps of 2000 were used. To study Li kinetics in a Si environment, diffusion pathways and barriers were determined using the climbing image nudged elastic band (NEB) method [75].

### 3.2.2.1 Stress-dependent migration energy barrier for diffusion

Diffusivity  $D$  is related to mobility according to Eq. (3.1).

$$\tilde{D} = D_0 e^{-\Delta E_a/RT} \quad (3.1)$$

where  $M$  is the mobility of the diffusion component, and  $R$  and  $T$  are the universal gas constant and the absolute temperature, respectively.

Here we consider the effect of the internal stress field on the migration energy barrier of diffusion, as follows. On the atomic-scale, the diffusion of a solute particle in an atomic lattice is described as a sequence of jumps from one interstitial site to an adjacent site, during which the diffusing particles must surmount the energy barrier caused by its interactions with the surrounding host atoms. Atomic

simulations show that this energy barrier is strongly affected by the internal stress field acting on the neighboring host atoms in the direction normal to the diffusion, suggesting a dependence on the biaxial stress on the thin film. Denoting the change in the migration energy due to the internal stress by  $\Delta E_a$ , the modified diffusivity,  $\tilde{D}$ , is expressed in Eq. (3.2).

$$D = MRT \quad (3.2)$$

where  $D_0$  is the stress-free diffusivity.

We assume a linear dependence of  $\Delta E_a$ , (i.e.,  $\Delta E = -\alpha\beta_{Si}\sigma_b$ ) around the zero stress value, so Eq. (3.2) can be rewritten as Eq. (3.3) [34, 35].

$$\tilde{D} = D_0 e^{-\alpha\beta_{Si}\sigma_b/RT} \quad (3.3)$$

where  $\alpha$  is a positive dimensionless coefficient, and  $\beta_{Si}$  and  $\sigma_b$  are the partial molar volume of Si and the biaxial stress, respectively.

We simulated the Li migration energy barrier in a Si  $2 \times 2 \times 2$  supercell that contains 64 Si atoms. Li interstitial defects have only one migration pathway through a tetrahedral  $\rightarrow$  hexagonal  $\rightarrow$  tetrahedral trajectory. The calculated result using NEB shows a migration energy barrier of 0.602 eV, which is in good agreement with other reported results and our previous work [18]. To capture the

stress effects on Li migration, Li migration energy barriers are calculated as a function of the stress applied to a supercell. When Si is compressed, the Li migration energy barrier increases leading to slower diffusion. In contrast, Li diffusion is faster when Si is expanded. Using migration energy under zero stress,  $E_a(0)$  as the reference value, we can compute  $\Delta E_a(\sigma_b) = E_a(\sigma_b) - E_a(0)$ . To incorporate the continuum model, the simulation results are fit to a bilinear curve to derive the value of  $\alpha$  under compressive (0.0824) and tensile (0.1401) conditions, as shown in Fig. 3.2(a).

### 3.2.2.2 The mixing enthalpy of amorphous $\text{Li}_x\text{Si}$ alloy

We compute the compositional energetics of  $\text{Li}_x\text{Si}$  phases as follows. The  $\text{Li}_x\text{Si}$  structures are composed of 64 Si atoms with Li atoms occupying the most stable tetrahedral site. For each composition, several possible uniform distributions (5 samples) of Li atoms are examined to reduce the inhomogeneity and sampling error. We obtain the amorphous phase from MD simulations by first heating to 2000 K, which is sufficiently higher than the melting point of Si. These structures are subsequently equilibrated for 10 ps and then quenched to 0 K. Finally, the quenched structures are fully relaxed until the residual force components are within 0.1

eV/nm. For the mixing enthalpy of a-Li<sub>x</sub>Si, the formation energy of the resulting amorphous phases is calculated using Eq. (3.4) [76].

$$E_f(x) = E_{Li_xSi} - (xE_{Li} + E_{c-Si}) \quad (3.4)$$

where  $x$  is the molar fraction of Li per one mole of Si.  $E_{Li_xSi}$ ,  $E_{c-Si}$  and  $E_{Li}$  are the energies for the Li<sub>x</sub>Si phases, the crystalline Si structure the Li metal bcc structure, respectively.

Figure 3.2(b) shows that the formation energies of amorphous Li<sub>x</sub>Si. At  $x=0$ , the amorphous phase is more unstable than crystalline Si. The associated formation energies are positive until  $x=0.5$ . With increasing  $x$ , however, the formation energy decreases monotonically, reaching a global minimum at  $x=3.5$ . From the profile of formation energy, the Li content is expected to increase homogeneously because the formation energy of a-Li<sub>x</sub>Si is convex throughout the compositional range.

The energy of Li<sub>x</sub>Si composition is defined as [77, 78].

$$\psi(x, T) = \left[ x\mu_0^{Li}(T) + \mu_0^{Si}(T) + RTx_{\max} \left\{ \tilde{c} \ln \tilde{c} + (1 - \tilde{c}) \ln(1 - \tilde{c}) \right\} + \psi^{exc}(x) \right] \quad (3.5)$$

where  $\mu_0^{Li}$  and  $\mu_0^{Si}$  are the standard chemical potential of Li and Si and  $x_{\max}$  is the maximum solubility of Li in a mole of Si and  $\tilde{c}$  is the normalized concentration (i.e.,  $\tilde{c} = x/x_{\max}$ ). The third term represents the mixing entropy

based on ideal mixing from the solution theory. In a thermodynamic view, diffusion of Li particle from a high concentration to lower concentration leads to an increase in entropy of the system. The last term,  $\psi^{exc}$  is the molar excess energy per mole of Si, which describes the energy of new chemical bond formation as a function of the local concentration. This excess free energy can be expressed as Eq. (3.6) based on the Margules model [77, 79-81] which represent the result of the expanding of the equation describing the excess Gibbs free energy of a binary mixture in the form of the Redlich-Kister expansion.

$$\psi^{exc}(x) = x_{\max} \tilde{c}(1-\tilde{c}) [A_0 \tilde{c} + B_0(1-\tilde{c})] \quad (3.6)$$

where the empirical parameters,  $A_0$  and  $B_0$  are derived from the excess free energy which is representing the mixing enthalpy of  $\text{Li}_x\text{Si}$  by using DFT calculation.

### 3.2.3 Micro-scale simulation (diffusion and deformation)

#### 3.2.3.1 Chemo-mechanical chemical potential

In the continuum modeling of diffusion in solids, we introduce a chemo-mechanical potential  $\mu^*$  that derives from the stress-independent chemical potential (i.e.,  $\mu = \partial\psi(x,T)/\partial x$ ) and stress dependent chemical potential. It includes

the effect of the entropy of the system, the mechanical work, and the concentration-dependent mixing enthalpy. The mechanical work is associated with the elastic energy for the insertion (removal) of Li into (from) the Si host under hydrostatic stress, that can give rise to an additional driving force for Li diffusion [82]. Hence  $\mu^*$  is given by Eq. (3.7).

$$\mu^* = \mu_0^{Li} + RT \ln\left(\frac{\tilde{c}}{1-\tilde{c}}\right) - \Omega\sigma_h + 2(A_0 - 2B_0)\tilde{c} - 3(A_0 - B_0)\tilde{c}^2 + B_0 \quad (3.7)$$

where  $\Omega$  and  $\sigma_h$  are the partial molar volume of Li and the hydrostatic stress ( $\sigma_h = (\sigma_{11} + \sigma_{22} + \sigma_{33})/3$ ), respectively. With a chemo-mechanical potential, the diffusion flux,  $\vec{j}$ , in the host material is given in Eq. (3.8).

$$\vec{j} = -Mc\nabla\mu^* \quad (3.8)$$

where  $M$  and  $c$  are the mobility of the diffusing component Li and the molar concentration of Li (mole/m<sup>3</sup>).

Based on Eqs. (3.3, 3.7, 3.8), the mass conservation law with a modified diffusivity becomes Eq. (3.9).

$$\frac{\partial c}{\partial t} = -\nabla \cdot \vec{j} = \nabla \cdot \left[ \tilde{D} \left\{ \left( \frac{c_{\max}}{c_{\max} - c} \right) \nabla c - \frac{\Omega c \nabla \sigma_h}{RT} + \left( \frac{2(A_0 - 2B_0)}{RT} \left( \frac{c}{c_{\max}} \right) + \frac{-6(A_0 - B_0)}{RT} \left( \frac{c}{c_{\max}} \right)^2 \right) \nabla c \right\} \right] \quad (3.9)$$

where  $c_{\max}$  is the maximum molar concentration of Li corresponding to the maximum molar fraction of Li per mole of Si (i.e.,  $\text{Li}_{x_{\max}}\text{Si}$ ).

The boundary conditions are set as an initial Li concentration of zero (i.e.,  $c=0$  for  $t=0$ ) and the Li flux at steady state. The electrochemical reaction is related to the applied discharge/charge current density through Faraday's law,  $j=i/F$ , where  $i$  is the current density and  $F$  is the Faraday constant.

### 3.2.3.2 Kinematics of large deformation

For this analysis, we consider a two-dimensional Si thin film electrode, which undergoes a large deformation due to the process of lithiation and delithiation in the LIB. The kinematics of deformation model is assumed to simplify the elastic-perfectly plastic model [83]. As lithium atoms migrate in (or out) of the silicon electrode, the deformation is characterized by the sum of the contributions from the reversible elasticity, compositional swelling, and irreversible plasticity. The total strain increment can be written as Eq. (3.10) [23].

$$d\boldsymbol{\varepsilon}_{ij} = d\boldsymbol{\varepsilon}_{ij}^e + d\boldsymbol{\varepsilon}_{ij}^c + d\boldsymbol{\varepsilon}_{ij}^p \quad (3.10)$$

In Eq. (3.10), the increment of elastic strain,  $d\boldsymbol{\varepsilon}_{ij}^e$ , obeys the classical Hooke's law with two elastic properties (See Eq. (3.11)).

$$d\varepsilon_{ij}^e = \frac{1}{E(c)} [(1 + \nu(c))d\sigma_{ij} - \nu(c)d\sigma_{kk}\delta_{ij}] \quad (3.11)$$

where  $E(c)$  and  $\nu(c)$  are the Li concentration-dependent Young's modulus and Poisson's ratio for the a-Li<sub>x</sub>Si from 90GPa to 40GPa, and from 0.28 to 0.24, respectively [62], and  $\sigma_{ij}$  and  $\delta_{ij}$  are the Cauchy stress and the Kronecker delta, respectively.

We assume that the increment of the compositional strain,  $d\varepsilon_{ij}^c$ , is proportional to the increase of the Li concentration, and the compositional strain is dilatational without spin (See Eq. (3.12)).

$$d\varepsilon_{ij}^c = \frac{\Omega dc}{3} \delta_{ij} \quad (3.12)$$

The increment of the plastic strain,  $d\varepsilon_{ij}^p$ , in Eq. (3.10) is assumed to obey the classic J<sub>2</sub>-flow theory. When the von Mises stress equivalent stress ( $\sigma_{von} = \sqrt{3\sigma'_{ij}\sigma'_{ij}/2}$ ) equals the yield strength,  $\sigma_Y$ , plastic yielding occurs.  $\sigma'_{ij}$  is the deviatoric stress ( $\sigma'_{ij} = \sigma_{ij} - \sigma_{kk}\delta_{ij}/3$ ).  $d\varepsilon_{ij}^p$  then becomes that represented in Eq. (3.13).

$$d\varepsilon_{ij}^p = \dot{\lambda} \sigma'_{ij} \quad (3.13)$$

where  $\dot{\lambda}$  is a scalar coefficient that can be determined by solving the boundary value problem. We set the yield strength,  $\sigma_Y$ , to be 1.75 GPa [27].

As the time required for Li-ion diffusion in the solid is much longer compared with that required for achieving mechanical equilibrium, a kinematics deformation can be considered as the quasi-static state at any time when a boundary condition involves traction-free at the surface (See Eqs. (3.14) and (3.15)).

$$\sigma_{ij,j} = 0 \quad \text{in } V \quad (3.14)$$

$$n_i \sigma_{ij} = 0 \quad \text{on } S \quad (3.15)$$

where  $V$  and  $S$  are the volume and the surface of the Si thin film, respectively, and  $\mathbf{n}$  is the outward normal of the outer surface of the Si thin film.

The above finite element models of a coupled problem were constructed and analyzed using COMSOL Multiphysics 5.0.

#### 3.2.4 Mesoscale simulation (Butler-Volmer kinetics)

The Butler-Volmer kinetics is employed to obtain the expected potential and capacity of an a-Si anode during lithiation and delithiation. The half-cell consists of a Si thin film, which is attached to a current collector together and a Li counter electrode. The two electrodes are separated by an electrolyte and are connected

through an external circuit. We assume that the overall cell potential is taken as the summation of the activation overpotential at the interface between the electrolyte and the surface of a-Si thin film and electrode open-circuit potential, because the activation overpotential at the Li/electrolyte interface and the overpotential associated with the mass transport of  $\text{Li}^+$  within the electrolyte are relatively low [84, 85]. Electrochemical kinetics considering both a cathodic and anodic reaction is expressed by the Butler-Volmer equation (Eq. (3.16)).

$$i = i_0 \left[ \exp\left(\frac{\alpha_a F \eta}{RT}\right) - \exp\left(\frac{\alpha_c F \eta}{RT}\right) \right] \quad (3.16)$$

where  $i_0$ ,  $\alpha_a$ ,  $\alpha_c$ , and  $\eta$  are the exchange current density, anodic transfer coefficient, cathodic transfer coefficient, and activation overpotential at the interface, respectively.

The activation overpotential,  $\eta$ , is defined as

$$\eta = \Phi_1 - \Phi_2 - U_{OCP} \quad (3.17)$$

where  $\Phi_1$ ,  $\Phi_2$ , and  $U_{OCP}$  are the electrode potential, electrolyte potential, and open circuit potential for the Si thin film, respectively. The electrolyte potential is assumed to be zero at the interface [85]. The open circuit potential as a function of the state of charge has been measured previously by T. D. Hatchard et al. [86]. The

exchange current density is given by Eq. (3.18).

$$i_0 = Fk(c_{\max} - c_{surf})^{0.5}(c_{surf})^{0.5}(c_{el})^{0.5} \quad (3.18)$$

where  $k$ ,  $c_{surf}$ , and  $c_{el}$  are the Li lithiation/delithiation reaction rate constant, the surface concentration of Li in the electrode, and the Li-ion concentration in the electrolyte, respectively. The galvanostatic discharge/charge operation is assumed. Thus, the current density,  $\dot{i}$ , is applied as a boundary condition depending on the C-rate.

**Table. 3.1** Parameters used in modeling of Si thin film electrode.

| Parameter            | Value   |
|----------------------|---|
| $T$                  | 300 K   |
| $R$                  | $8.314 \text{ J K}^{-1} \text{ mol}^{-1}$                               |
| $F$                  | $9.649 \times 10^4 \text{ C mol}^{-1}$                                  |
| $D_0$                | $10^{-17} \text{ m}^2 \text{ s}^{-1}$ [87]                              |
| $k$                  | $1.55 \times 10^{-13} \text{ m s}^{-1} (\text{mol m}^{-3})^{-0.5}$ [88] |
| $\alpha_a, \alpha_c$ | 0.5   |
| $c_{\max}$           | $3.125 \times 10^5 \text{ mol m}^{-3}$ [89]                             |
| $c_{el}$             | $1000 \text{ mol m}^{-3}$ [90]  |
| $\Omega$             | $4.24559 \times 10^{-6} \text{ m}^3 \text{ mol}^{-1}$                   |
| $\alpha$             | 0.0824 (Compressive), 0.1401 (Tensile)                                  |
| $\beta_{Si}$         | $1.2 \times 10^{-5} \text{ m}^3 \text{ mol}^{-1}$ [91]                  |
| $x_{\max}$           | 3.75 [92]   |
| $A_0$                | $-4.277 \times 10^4 \text{ J/mol}$                                      |
| $B_0$                | $-1.504 \times 10^4 \text{ J/mol}$                                      |
| $\nu(c)$             | 0.28 (Initial), 0.24 (Fully lithiation) [62]                            |
| $E(c)$               | 90 GPa (Initial), 40 GPa (Fully lithiation) [62]                        |

---

---

### 3.3 Results and discussion

#### 3.3.1 Stress evolution (lithiation and delithiation)

We simulate the stress evolution in an a-Si thin film electrode (150nm) subjected to a lithiation and delithiation cycle by employing a constant current density of  $140 \mu\text{Acm}^{-2}$  (ca. 1C-rate), as shown in Fig. 3.3(a). The film is amorphous even before lithiation and thus we don't have to explain the phase transitions observed in crystalline Si.

We constrain the in-plane deformation of the a-Si thin film in order to simulate the behavior of an a-Si thin film bonded to a thick substrate. Hence, the lithiation-induced volume change occurs only by out-of-plane expansion. Figure 3.3(b) and 3.3(c) show the biaxial stress evolution through the thickness of Si film for lithiation and delithiation at selected times, respectively. During lithiation, the compressive stress increases sharply in the initial stage, indicating an elastic response. Then the stress reaches an elastic limit of  $\sim 1.75$  GPa at  $t \approx 50$  s. With further lithiation, compressive plastic deformation occurs at the outer part of the film and continuously propagates to the interior region of the a-Si thin film to accommodate additional volume expansion. Upon delithiation, Si unloading is initially elastic (up to  $\sim 250$ s). The stress experiences compressive elastic unloading,

tensile elastic loading, and tensile plastic yielding sequentially, reaching a tension of  $\sim 1.75$  GPa due to the plasticity of delithiated silicon. This stress evolution of  $\text{Li}_x\text{Si}$  thin films influences the chemical potential and migration energy barrier for Li diffusion.

### 3.3.2 Atomic-scale simulation effects on Li diffusion

The multi-scale model split into four different models so that we can investigate the stress and mixing enthalpy effects on the distribution of Li in the a-Si electrode. The four models are (1) the diffusion-induced stress (DIS) model, (2) DIS coupled with stress-dependent migration energy barrier, (3) DIS coupled with concentration-dependent mixing enthalpy, and (4) DIS coupled with both models just mentioned.

Before considering the effects of the various physical phenomena, we first check the DIS model driven by the chemo-mechanical potential. (i.e.,  $c/c_{\max} \ll 1$ ,  $A_0 = B_0 = \alpha = 0$  in Eq. (3.9)). Figure 3.4(a) shows the thickness variation of Li at different times. During Li insertion, the Li concentration continuously increases with time and, concurrently, the concentration of Li in the interior region also

slightly increases, which is responsible for the compressive hydrostatic stress gradient in the electrode. To assess the effect of the stress-dependent migration energy barrier, the modified diffusivity,  $\tilde{D}$ , for Li is added to the DIS model. As shown in Fig. 3.4(b), the concentration profiles are overestimated in the surface region compared with the DIS model. This overestimation occurs because the diffusivity (migration energy barrier) near the film surface is reduced (increased) by the developed compressive stress. Thus, additional Li atoms accumulate near the thin film surface, and the elastic stress contribution squeezing Li atoms into the interior region is relatively weak. We next examine the influence of the concentration-dependent mixing enthalpy on Li diffusion by setting  $\alpha = 0$  in Eq. (3.9). The surface concentration at the initial stage is lower compared with the previous two models, and the concentration gradient decreases. The predicted concentration profile becomes substantially more uniform, as shown in Fig. 3.4(c), because the mixing enthalpy of Li and Si accelerates the chemical driving force for lithiation that acts in the same direction as the concentration gradient. In the fully coupled model, the effects of migration energy and enthalpy contribution alter the Li concentration profiles shown in Fig. 3.4(d). The migration energy contribution decreases the Li diffusivity due to compressive stress elastically and plastically, whereas mixing enthalpy enhances the chemical potential as the Li concentration

increases. Thus, it appears that both effects are incorporated into the model for the Li concentration distribution.

As lithiation proceeds to the last stage, Figure 5 shows that the evolution of the Li concentration profile is a function of dimensionless time,  $\tau = t / t_{total}$ , where  $t_{total}$  is the total lithiation time. The surface Li concentration at the end of lithiation is less than the theoretical maximum Li concentration,  $c_{max}$  because we adopt a cutoff potential of 0.01V on the surface of the thin film. First, in Fig. 3.5(a), the gradient of the Li concentration simulated by the DIS model shows a steady state profile as lithiation progressed (i.e., at  $\tau > 0.3$ ). This steady state profile means that the hydrostatic stress effect on the chemical potential does not increase as lithiation progresses due to the fully developed plastic deformation within Si thin film. Hence, the overall concentration distribution follows profiles simulated by the classical Fick's law for diffusion. In Fig. 3.5(b), the Li concentration gradient is extremely steep due to the decrease in Li diffusivity caused by biaxial stress. Therefore, although at the last step the surface Li concentration reaches a maximum, a state of charge (SOC) in the Si thin film is about 0.48 compared to the maximum SOC, which means that a considerable portion of available lithiation Li is yet to be lithiated. In contrast, the contribution of mixing enthalpy effect generates a

substantially uniform Li concentration profile in the late stage, as shown in Fig. 3.5(c). This is expected because the mixing formation energy of Li and Si prefers to spread Li atoms. This result suggests that the mixing enthalpy contribution to the chemical potential gradually increases as the Li concentration increases. From DFT calculation results, the mixing formation energy of a-Li<sub>x</sub>Si for all composition is smaller than the mixing energy of Li metal and a-Si. a-Li<sub>x</sub>Si phase grows stably leading to a homogenous phase evolution, which is in good agreement with our continuum analysis. However, note that in crystalline Si, the initial incorporation with Li is unfavorable leading to phase separation of c-Si (Crystalline Silicon) and c-Li<sub>x</sub>Si (or a-Li<sub>x</sub>Si) due to the positive mixing formation energy of Li and c-Si [93]. However, in this paper, we do not explain this situation in any more detail. In the fully coupled model, we can clarify the role of the various effects on Li diffusion in the a-Si thin film. In the early stage of lithiation, the contribution of migration energy and mixing enthalpy are compatible, as we already discussed. When lithiation continues, the mixing enthalpy effect is dominant in the concentration profiles as shown in Fig. 3.5(d).

### 3.3.3 Potential hysteresis

The electrode potential is obtained using Eqs. (3.16-3.18). The parameters used for this simulation are listed in Table. 3.1. Figure 3.6 shows the predicted capacity vs. potential curves for the four different models at a 1C-rate. As the Li concentration at the Si surface increases, its electric potential relative to the counter electrode decreases during the discharge process. This discharge processes of each model are stopped when the cell potential reaches 0.01 V and the external current is reversed (charge process). During charging, as the Li concentration decreases, its potential increases. This charging process is also terminated once the potential of the cell reaches 1.0 V. The calculated capacity is determined by the total amount of Li inserted into the Si thin film.

The dotted curve (DIS model) in Fig. 3.6, does not reproduce the potential evolution on discharge. The predicted capacity is less than that of the fully coupled model because the discharge cut-off potential is reached earlier. Hence, this model requires an adjustment of diffusivity to fit the experimental data [68, 94]. For the dashed - dotted curve corresponding to the second model, the surface Li concentration reaches its maximum concentration very rapidly because the distribution of Li is highly inhomogeneous, as discussed above. At the end of

lithiation, not much lithium has been inserted into the Si electrode, so the expected capacity is low and the cell performance is underestimated by the diffusion limitations. These results are not in good agreement with the experimental results. On the other hand, the third model (dashed curve) is sufficient to describe the half-cell during the discharge process. This model allows adequate time for Li diffusion to nearly homogenize the Li distribution before the Li concentration on the surface of the electrode reaches the maximum value (A). However, during the charging process, the capacity of the last step of delithiation corresponding to the potential of 1.0 V is relatively small compared with the experimental results. In the fully coupled model (solid line), even though the mechanical stress contributes the potential drop at the beginning of lithiation (shown in Fig. 3.6 inset) due to the high Li concentration at the surface by the reduction of diffusivity (B), the mixing enthalpy contribution minimizes the potential drop for a while (C), producing a larger-than-expected capacity. Moreover, the charge capacity also increases by the reduced migration energy barrier resulting from the tensile stress in the Si thin film (D). Based on the present observations, we conclude that this multi-scale approach should be employed for a more accurate simulation of the half-cell during discharging and charging.

### 3.3.4 Comparison with experimental data

Potential hysteresis as a function of capacity obtained using the fully coupled model compared with experimental data corresponding to the discharge/charge behavior of Si thin film electrode (300nm) at C/8 rate ( $20.68 \mu\text{Acm}^{-2}$ ) between 1.0 and 0.01 V vs. Li/Li<sup>+</sup>, to validate the multi-scale model. As shown in Fig. 3.7(a), the cycling behavior of the simulated result is very similar to that obtained from an experimental measurement [95]. However, the slight difference in the potential evolution at the end of discharge is observed that may be attributed to the open circuit potential estimation. And the simulated charging curve does not show good agreement with the experimental data even using the multi-scale model, which suggests that some physics were not considered in our model for charging process that may play an important role during delithiation. Nevertheless, the multi-scale simulation captures well the dominant feature of potential behavior.

We also simulate the cell potential during galvanostatic discharge and charge of the a-Si thin film at different C-rates (C/2, C/4, C/8, C/15, and C/30). The 1C-rate for the a-Si thin film is  $165.44 \mu\text{Acm}^{-2}$  at a thin Si film thickness of 300 nm. The simulation is conducted between an upper cut-off potential of 1.0 V vs. Li/Li<sup>+</sup> and 0.5 SOC, the same conditions as Ref. [95]. The potential is plotted as a function

of normalized SOC.

Figure 3.7(b) represents the multi-scale model predictions, while Fig. 3.7(c) shows the experimental data in Ref [95]. The multi-scale model agrees very well with experimental results over a wide range of C-rates. The increase in the Li flux (higher C-rate) develops a comparatively large concentration gradient in the thin film leading to a sharp decrease in the potential and a significantly increased Li concentration at the surface. Concurrently a reduction in diffusivity caused by the migration energy barrier also instigates an ohmic drop in simulation (A). However, as lithiation is progressed, the mixing enthalpy contribution is gradually taken into account, and the potential is invariant at different C-rates at a given 0.5 SOC (B). That could be indicative of a battery operating near thermodynamic equilibrium. Furthermore, it can be seen that the C-rate has very little impact on the potential offset between lithiation and delithiation, similar to the rate capability data reported on Si nanowires and amorphous Si thin film [12, 96]. These reports also show that the potential for discharge occurs over a larger range of C-rates than those for charging, similar to the experimental results shown in Refs. [12, 96].

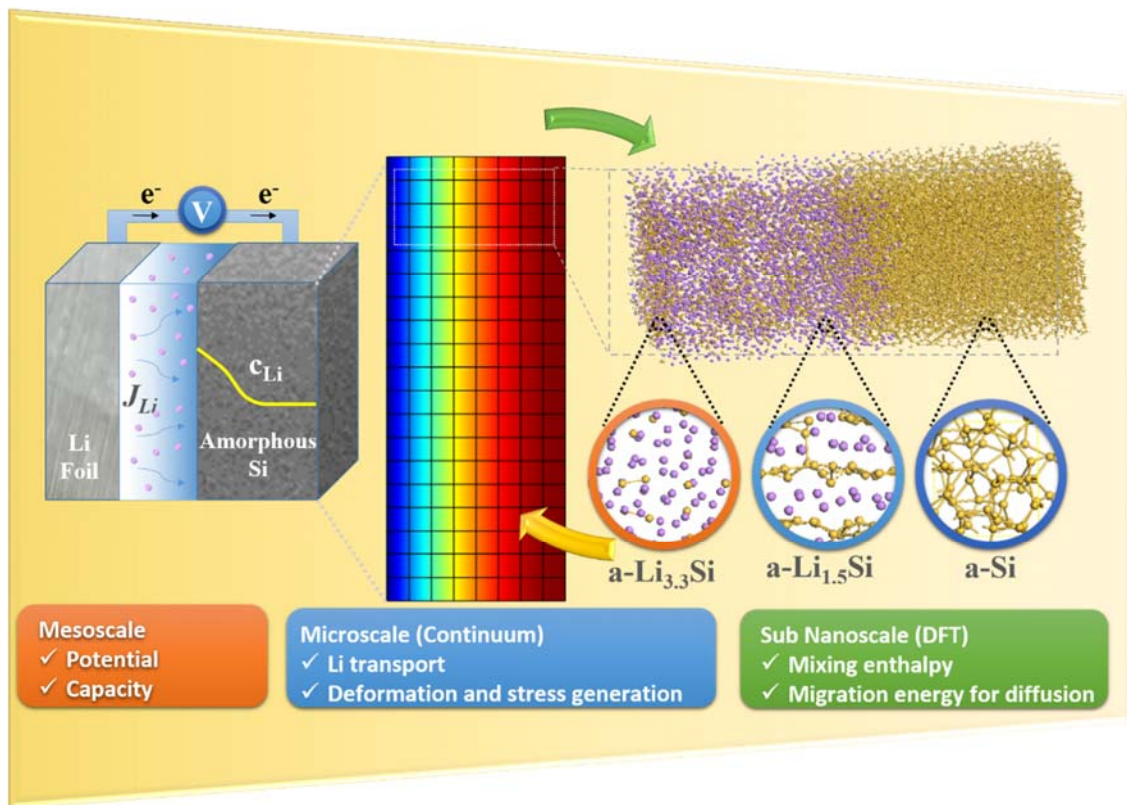
### 3.3.5 Comparison with the DIS model at different charge rates

Figure 3.8 shows comparisons of the multi-scale model with the DIS model at  $C/2$ ,  $C/8$ , and  $C/30$ . The DIS model shows a similar behavior with the multi-scale model at low C-rate, but the discrepancy between the two models increases at higher C-rates. This fact demonstrates that the DIS model is a reasonably good model for a half-cell at low rates because the concentration gradient across the thin film is small and the effects of atomic-scale physics are minimal. The DIS model is unsatisfactory as the C-rate increases, however. At higher C-rates, the diffusion limitation in Si thin films becomes more severe, which clearly leads to the reduction of the expected capacity. Additionally, the DIS model gives less satisfactory results as the thickness of the cell increase for the same reason. Therefore, it is noted that atomic-scale physics should be taken into account in half-cell modeling for the proper description of transport in a system at high C-rate conditions and for thick electrodes.

## 3.4 Remarks

We have proposed and discussed a multi-scale model to simulate the

electrochemical behavior of Si thin film anodes during discharge/charge cycling. The stress-dependent migration energy barrier and the molar excess Gibbs free energy of Si and Li were calculated using DFT and incorporated into the continuum DIS model. These effects significantly influence the nonlinear distribution of the Li concentration and macroscopic kinetics (i.e., potential vs. capacity hysteresis). In the multi-scale framework, during lithiation, compressive stress increases the migration energy barrier, which results in Li atom accumulation near the thin film surface, and leads to a potential drop. However, upon further lithiation, the mixing enthalpy enhances the chemical potential, resulting in a substantially uniform Li concentration profile. This uniform profile contributes to reducing the potential drop for the remaining lithiation time. Hence, the anode exhibits a reasonable discharge capacity. On the other hand, during delithiation, the reduction of the migration energy barrier resulting from the tensile stress in the Si thin film facilitates achieving a larger-than-expected charge capacity. Accordingly, we have demonstrated that our multi-scale model predicts the hysteresis of a potential capacity of a-Si thin film anode, matching well with the experimental data. Our multi-scale model is especially applicable to a high-capacity anode undergoing a high C-rate condition. Therefore, atomic-scale physics should be taken into account to accurately model half-cell.



**Fig. 3.1** Schematic of a multi-scale model of amorphous Si in a Li-ion battery.

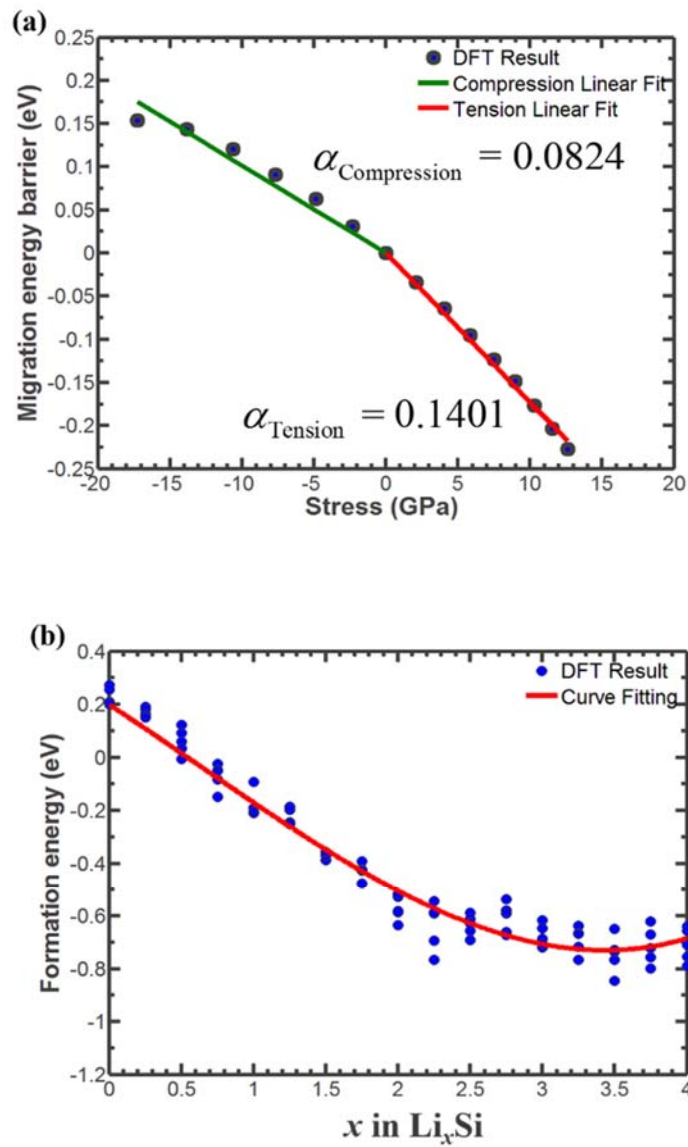


**Fig. 3.2** (a) Migration energy barrier as a function of the internal stress field acting on the neighboring host atoms in the direction normal to diffusion. Tensile stress decreases the migration energy barrier, while compressive stress increases it. (b) Formation energy of a- $\text{Li}_x\text{Si}$  as a function of the molar fraction of Li at  $T = 0$  K.

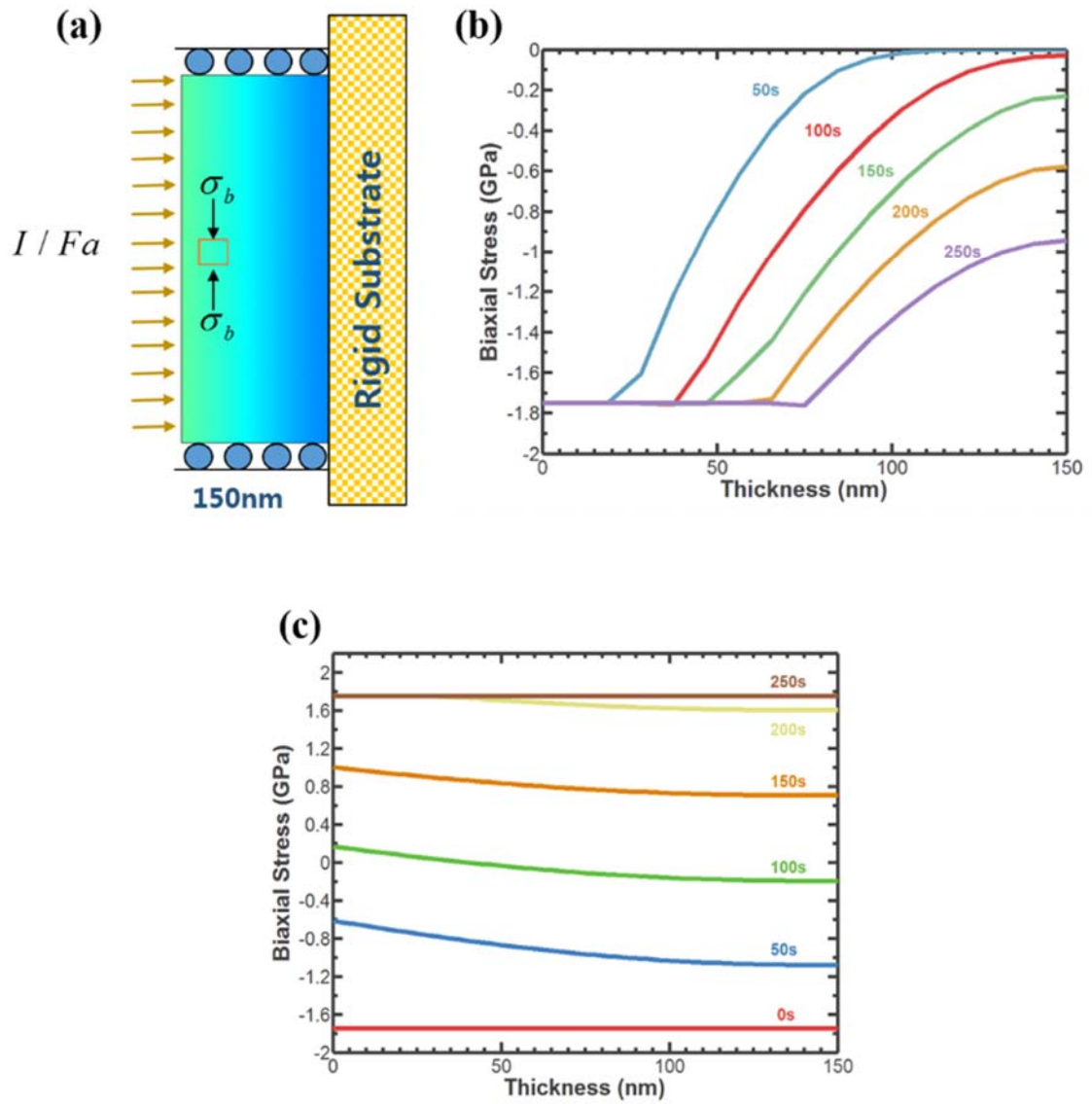


**Fig. 3.3** (a) Schematic of the a-Si thin film. Biaxial stress evolution through the thickness of the a-Si film for lithiation (b) and delithiation (c) at selected times.

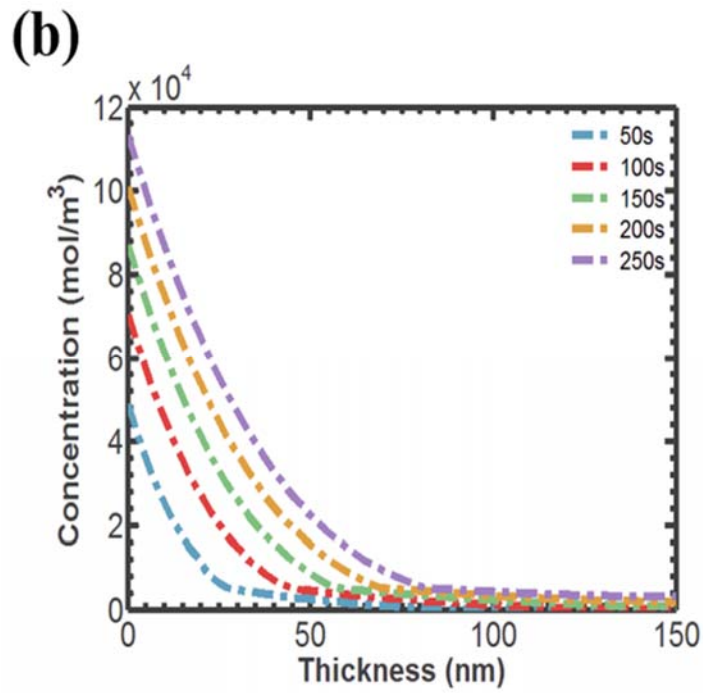
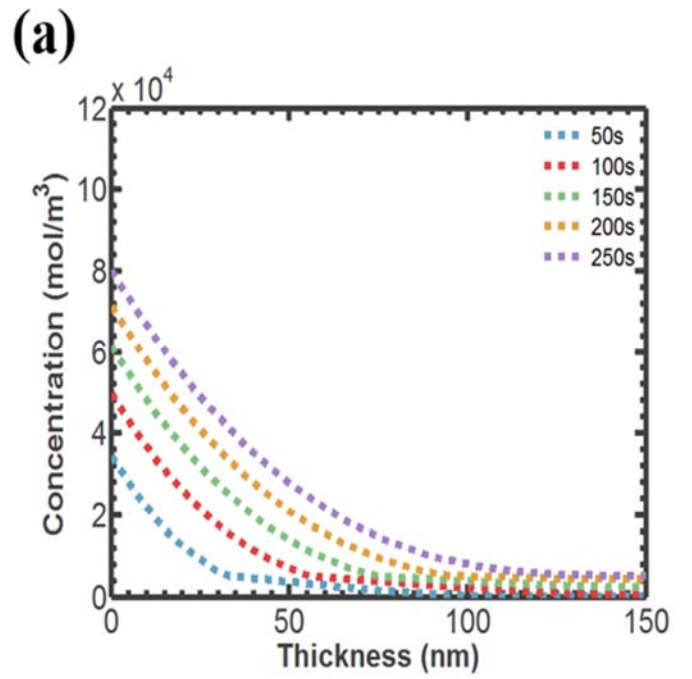


**Fig. 3.4** Distributions of Li concentration: (a) Diffusion induced stress (DIS) model, (b) DIS coupled with stress-dependent migration energy barrier.

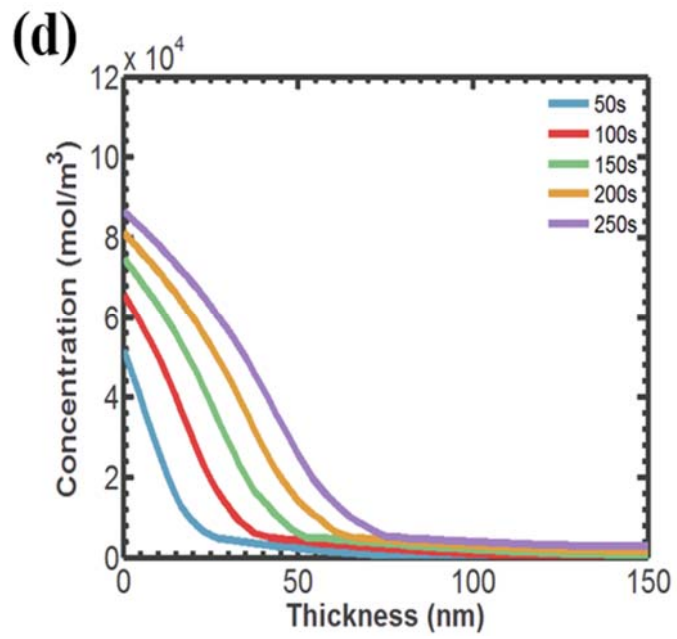
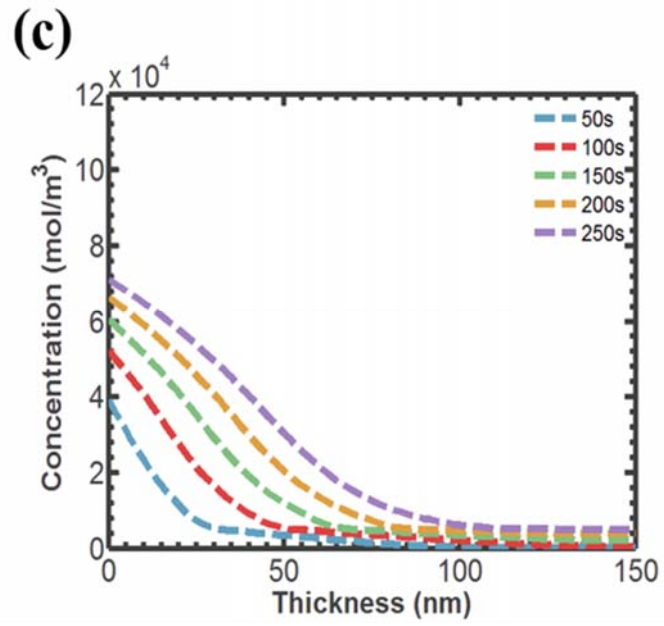


**Fig. 3.4** Distributions of Li concentration: (c) DIS coupled with concentration-dependent mixing enthalpy and (d) fully coupled model at short times ( $\sim 250\text{s}$ ).

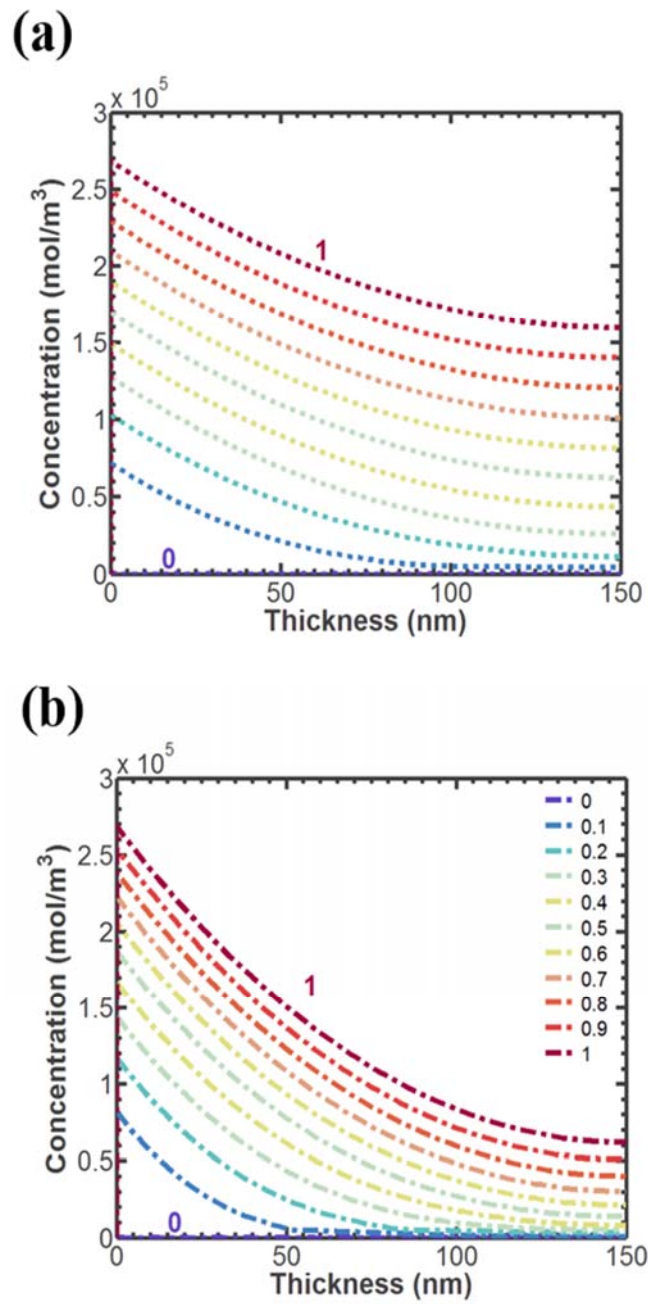


**Fig. 3.5** Time evolution of the distributions of Li concentration during lithiation for four models: (a) Diffusion induced stress (DIS) model, (b) DIS coupled with stress-dependent migration energy barrier.

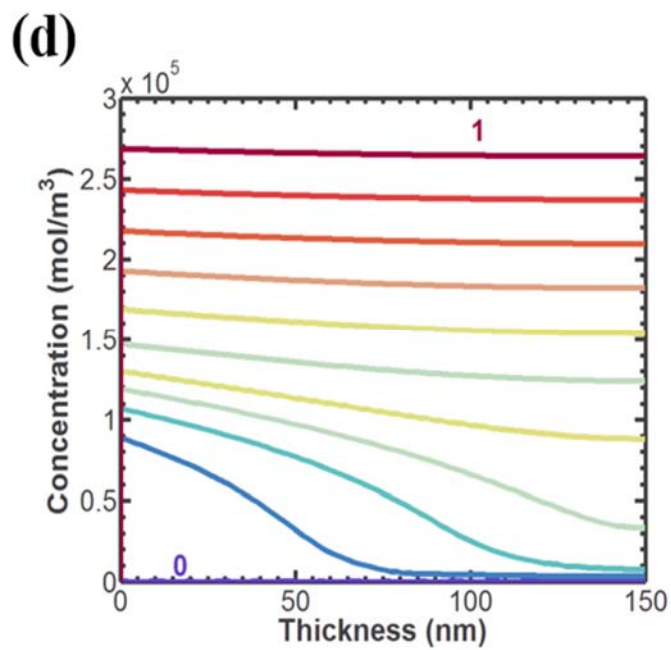
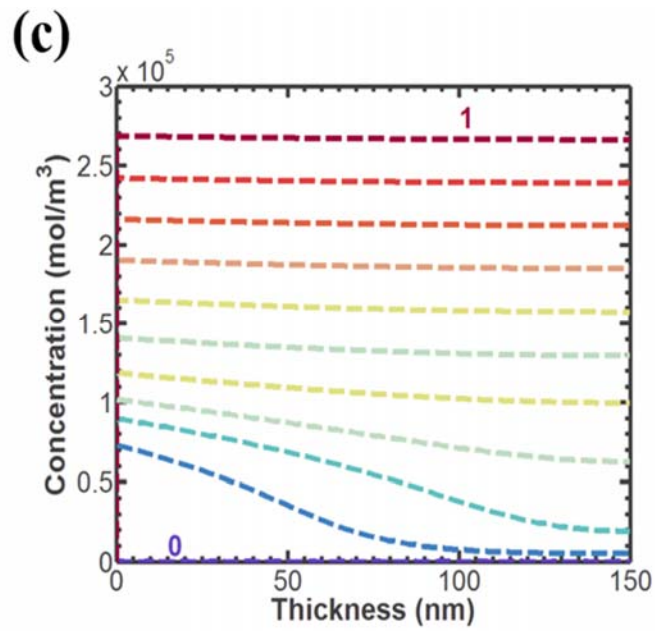


**Fig. 3.5** Time evolution of the distributions of Li concentration during lithiation for four models: (c) DIS coupled with concentration-dependent mixing enthalpy and (d) fully coupled model.

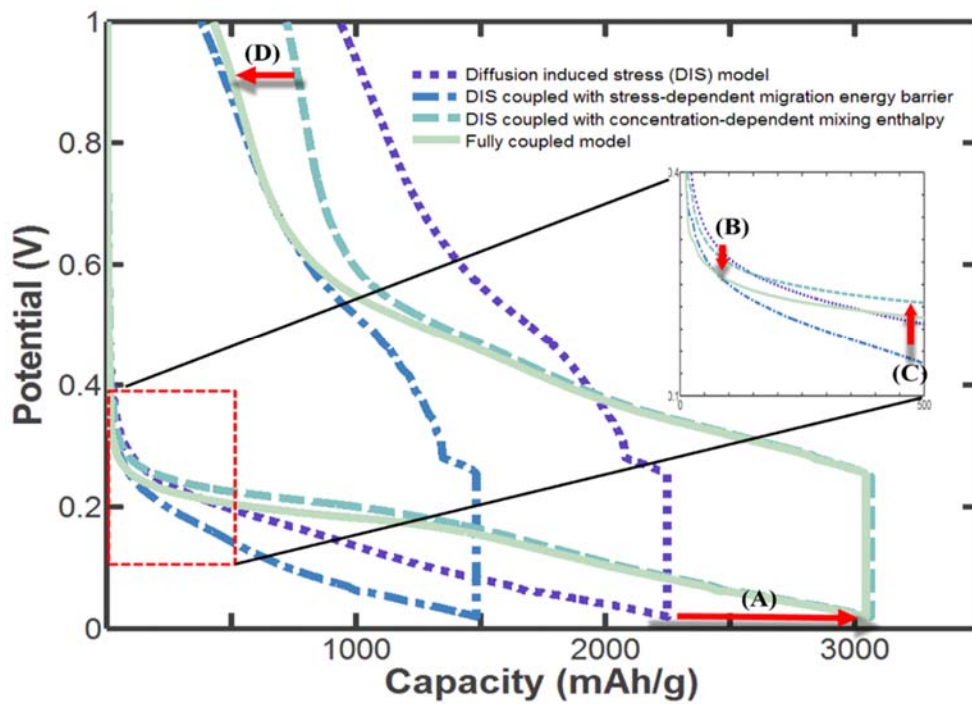


**Fig. 3.6** Si electrode potential vs. capacity during lithiation and delithiation at a 1C rate for four different models.

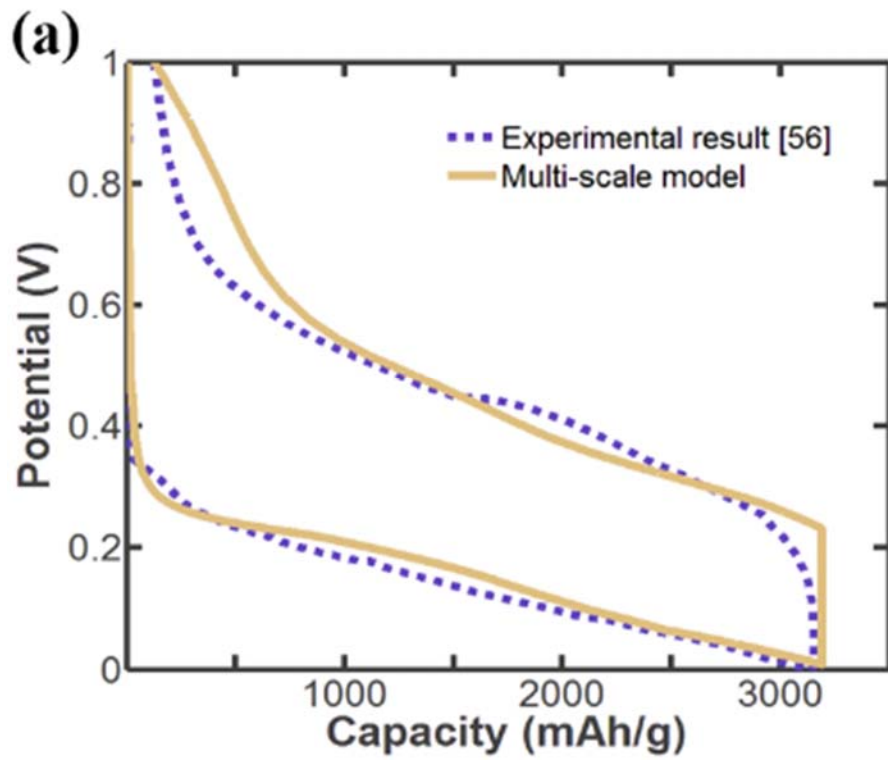


**Fig. 3.7 (a)** Comparison of the multi-scale simulation result with the experimental data [95] for an a-Si thin film electrode (300nm) at C/8 ( $20.68 \mu\text{Acm}^{-2}$ ).

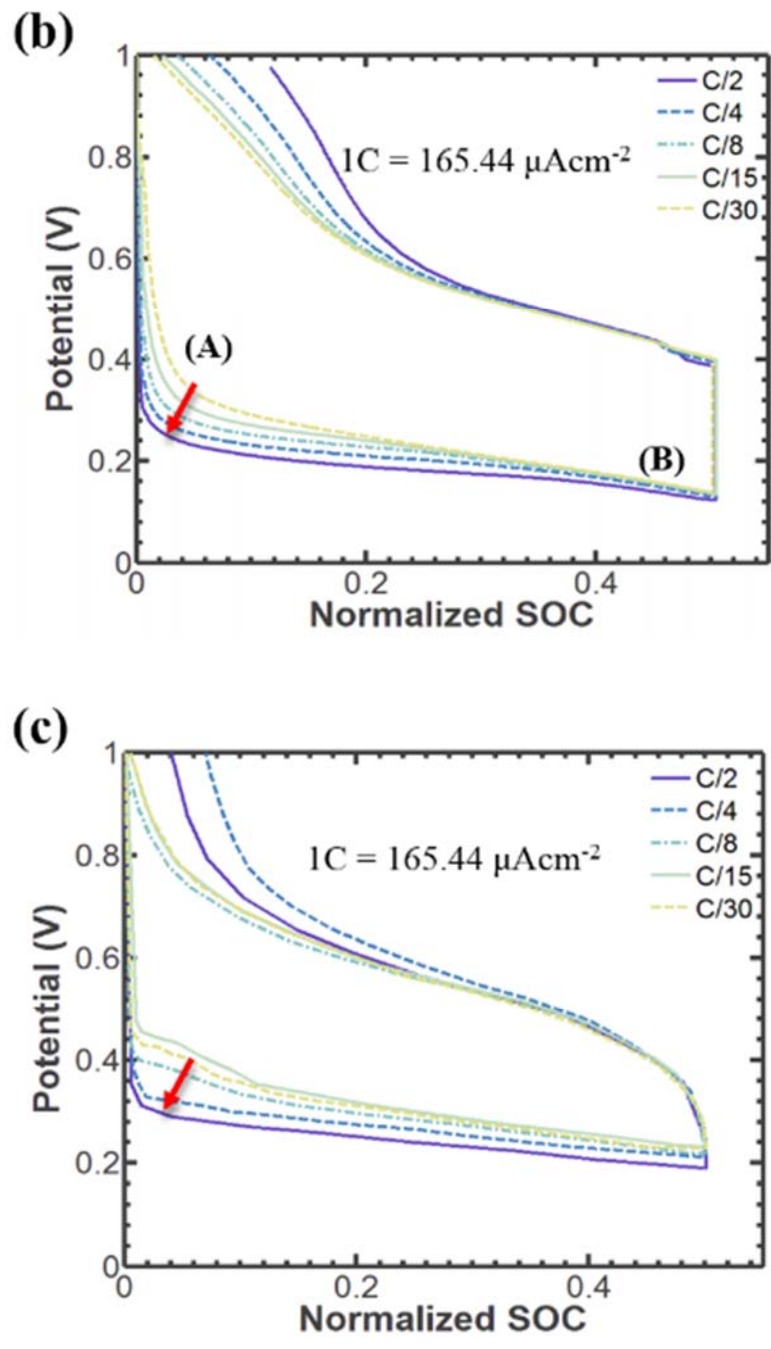


**Fig. 3.8** Comparison of simulated curves (b) and the experiment results of Ref. [95] (c) corresponding to charge rates from C/2 to C/30 between 0 and 0.5 SOC.

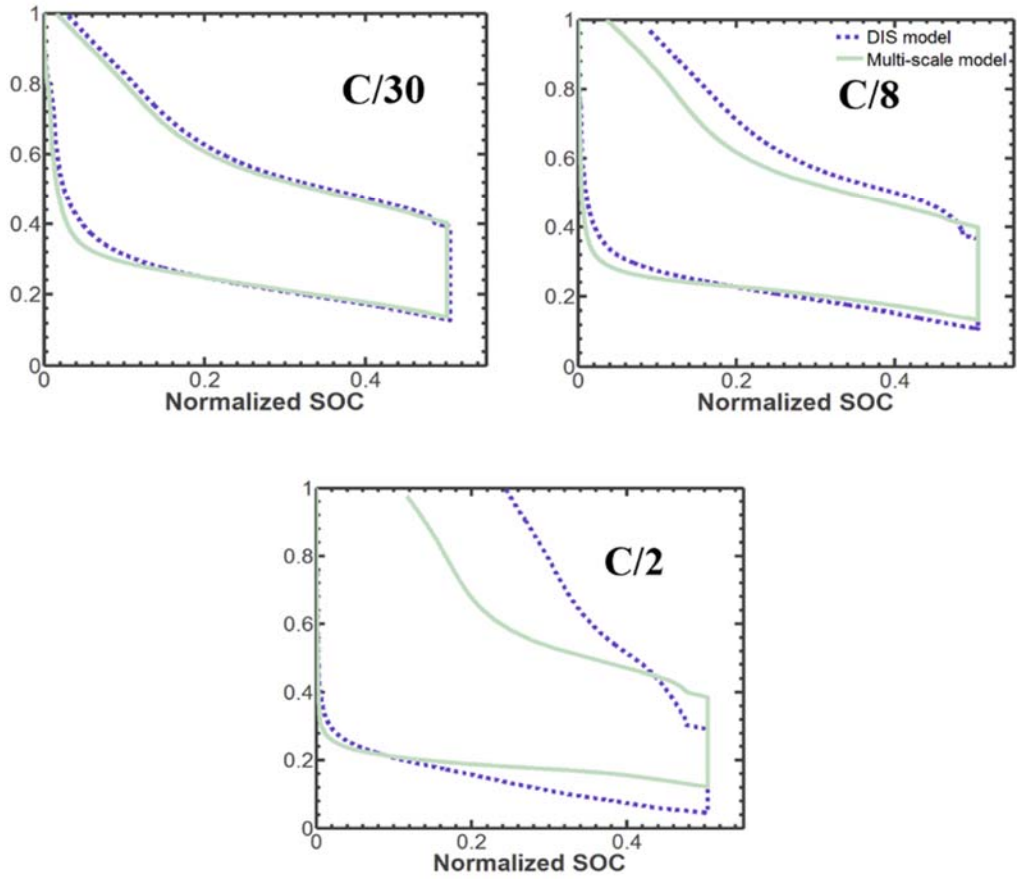


**Fig. 3.9** Comparison of the DIS model with the multi-scale model at C/30,C/8m and C/2 between 0 and 0.5 SOC.

## **Chapter 4**

# **Electrochemical response of patterned Si with crack growth**

### **4.1 Introduction**

The capacity fade during the charge-discharge cycle is the most important issue in advanced lithium-ion batteries developing [97]. The electrode damage such as a crack is one of the primary causes of the battery degradation. The stresses resulting from the electrode volumetric change induce the crack within electrode during lithiation and delithiation[13]. The silicon anode absorbing a large amount of Li shows severe cracking associated with the large volume change by Li insertion/extraction [98].

When the charge rate is high and the size of Si increase, an increase in the damage rate is observed easily [16, 31, 42, 99]. To prevent the electrode damage and enhance the cyclic performance of the LIBs consequently, nanosized Si

materials are systematically investigated, for example, nanoparticle, nanowire, and thin film [12, 23, 52, 100-102]. However, the fabrication of nanomaterials utilizing the tools of nanotechnology is expensive. Moreover, high surface to volume ratio in nanostructure inevitably increases unexpected SEI layer [20]. In comparison, a limited amount of experiments has been carried out, so that the mechanical and electrochemical behavior of micro-sized Si is not explored well. Of course, because of its large size, the mechanical failure has been known as one of the most critical factors in the battery degradation [103].

Previous studies have focused on the delamination growth between Si thin film and substrates for the Si thin film [104-106]. Hamed Haftbaradaran et al. proposed a method to deduce the critical size for interfacial delamination of patterned thin film electrodes and Bo Lu et al. suggest the state of charge and the time to delamination onset and critical size for delamination. While this study explores the size and charge rate-dependent mechanical and electrochemical behavior of patterned Si thin films. As the film thickness increases, the internal cracking is not avoidable and this crack affects the Li diffusion [107]. Unlike the lithium diffuses freely through the host material, when there is a crack within the host material, Li diffuses around the crack as shown in Fig 4.1. As a result, the Li concentration

homogeneity in host material during lithiation/delithiation increases with crack density, i.e., the effective diffusivity is lower. Consequently, the crack affects the electrochemical response of Si thin film. Therefore, we propose an electrochemical model with crack growth which is utilizing the cohesive zone model. This study mainly investigates the relation between the electrochemical performance of LIB and crack growth with taking into account the impacts of Si size and charge/discharge rate condition.

## **4.2 Methodology**

### *4.2.1 Mixed-mode crack growth in the patterned Si*

The internal crack growth in the Si thin film is likely to occur under the mixed-mode debonding. In this condition, more than one mode is taken into account simultaneously, the damage is initiated even before any of the traction for pure modes reach their respective maximum value.

#### *4.2.1.1 Mixed-mode initiation criterion*

The interaction of the traction components in the initiation of the crack can be specified through different criteria. Herein, the initiation of the crack depends on

the current traction as shown in Fig. 4.2.

The total mixed-mode relative displacement  $\delta_m$  is defined as:

$$\delta_m = \sqrt{\langle \delta_n \rangle^2 + \delta_s^2} \quad (4.1)$$

where  $\delta_n$  and  $\delta_s$  are the normal relative displacement and the shear relative displacement. The operation  $\langle \cdot \rangle$  is the Macaulay bracket defined as  $\langle x \rangle = \max(0, x)$ ,  $x \in \mathbb{R}$ .

The traction before crack initiation with same penalty stiffness  $K$  in Mode I, II and III are

$$T_i = K\delta_i, \quad i = 1, 2, 3 \quad (4.2)$$

It is assumed that the initiation of crack can be predicted using the quadratic delamination criterion [108, 109]. When a quadratic interaction function of involving nominal stress ratio become one, the damage is initiated as defined below.

$$\left( \frac{\langle T_n \rangle}{N} \right) + \left( \frac{T_s}{S} \right) = 1 \quad (4.3)$$

where  $N$  and  $S$  are the mode I and mode II maximum allowable tractions.

The single mode relative displacement at crack initiation are

$$\delta_n^0 = \frac{T_n}{K} \quad (4.4)$$

$$\delta_s^0 = \frac{T_s}{K} \quad (4.5)$$

The mixity is defined as the ratio

$$\beta = \frac{\delta_s}{\delta_n} \quad (4.6)$$

Based on the above equations, the mixed-mode damage initiation is governed by

$$\delta_m^0 = \begin{cases} \delta_n^0 \delta_s^0 \sqrt{\frac{1 + \beta^2}{(\delta_s^0)^2 + (\beta \delta_n^0)^2}}, & \delta_n > 0 \\ \delta_s^0, & \delta_n \leq 0 \end{cases} \quad (4.7)$$

Single modes are particular cases of proposed formulation, as Mode I for  $\beta = 0$  and Mode II for  $\beta = \infty$ .

#### 4.2.1.2 Mixed-mode propagation criterion

The mixed-mode propagation criterion using energy based Benzeggagh and Kenane fracture criterion seems to deliver an adequate description of fracture for a wide range of materials (B-K criterion) [110]. The critical energy release rate,  $G_c$  in the B-K criterion, is evaluated based on the cohesive energy of the Mode I and Mode II and a parameter  $\eta$  which is determining the mixed-mode ratio. Normally ( $1 \leq \eta \leq 2$ ).

$$G_c = G_{Ic} + (G_{IIc} - G_{Ic}) \left( \frac{G_{II}}{G_I + G_{II}} \right)^\eta \quad (4.8)$$

The cohesive energy absorbed by each mode in a mixed-mode loading is

$$G_I = \frac{K \delta_{nm}^0 \delta_{nm}^f}{2} \quad \text{and} \quad G_{II} = \frac{K \delta_{sm}^0 \delta_{sm}^f}{2} \quad (4.9)$$

where  $\delta_{nm}^0$  and  $\delta_{sm}^0$  are the normal and shear relative displacement corresponding to the initiation of crack under mixed-mode loading. And  $\delta_{nm}^f$  and  $\delta_{sm}^f$  are normal and shear relative displacement corresponding to the complete separation under mixed-mode loading as shown in Fig. 4.1.

From Eq. (4.1) and Eq. (4.6) ~ Eq. (4.9), the total relative displacement corresponding to the complete separation under mixed-mode loading can be obtained as

$$\delta_m^f = \begin{cases} \frac{2}{K \delta_m^0} \left[ G_{Ic} + (G_{IIc} - G_{Ic}) \left( \frac{\beta^2}{\beta^2 + 1} \right) \right]^\eta, & \delta_n > 0 \\ \delta_s^f, & \delta_n \leq 0 \end{cases} \quad (4.10)$$

#### 4.2.1.3 Constitutive law

Only the maximum mixed-mode relative displacement  $\delta_m^{\max} = \max \{ \delta_m^{\max}, \delta_m \}$  at each point on the interface is used to track the damage. The damage evolution

function can be defined as

$$d = \frac{\delta_m^f (\delta_m^{\max} - \delta_m^0)}{\delta_m^{\max} (\delta_m^f - \delta_m^0)} \quad (4.11)$$

The irreversible bilinear softening constitutive behavior for mixed-mode loading for the shear component is defined as

$$K_{II} = \begin{cases} K & (\delta_m^{\max} \leq \delta_m^0) \\ (1-d)K & (\delta_m^0 < \delta_m^{\max} \leq \delta_m^f) \\ 0 & (\delta_m^f < \delta_m^{\max}) \end{cases} \quad (4.12)$$

For the normal component

$$K_I = \begin{cases} K_{II} & (0 < \delta_n) \\ K & (\delta_n < 0) \end{cases} \quad (4.13)$$

#### 4.2.2 Li diffusion and crack's effect on the Li diffusion

If there is an internal damage on the Si thin film, the diffusion of Li ions encounter obstructions and Li ions need to take a tortuous pathway around the crack. Therefore, it reduces the effective diffusivity of Li ions and increases Li inhomogeneity within Si thin film.

The description of the Li diffusion and crack's effect on Li diffusion are given as,

$$\mu^* = \mu_0^{Li} + RT \ln\left(\frac{\tilde{c}}{1-\tilde{c}}\right) - \Omega \sigma_h + 2(A_0 - 2B_0)\tilde{c} - 3(A_0 - B_0)\tilde{c}^2 + B_0 \quad (4.14)$$

$$j = \begin{cases} -Mc \nabla \mu^*, & \delta_m^{\max} \leq \delta_m^f \\ 0, & \delta_m^{\max} > \delta_m^f \end{cases} \quad (4.15)$$

When the total relative displacement,  $\delta_m^{\max}$  exceeds the complete of separation,  $\delta_m^0$  under mixed mode loading, it signifies the separation of Li diffusion region, so at which the Li flux becomes zero.

## 4.3 Results and discussion

### 4.3.1 Lithium distribution with & without the crack

Figure 4.3 shows the Li distribution in a patterned Si during lithiation (a) and delithiation (b). An electrochemical reaction occurs on the exposed side of the patterned Si and Li evenly diffuses into the Si and distribute homogeneously when there is no crack. In a cohesive zone model, an internal crack is observed at the internal region of the pattern Si in the early lithiation stage thus Li-ion needs to move in a tortuous pathway around the crack. The inhomogeneity of Li distribution gradually increases. During the delithiation, the internal crack also impedes diffusion of Li out of the Si, and thereby the electrochemical reaction is stopped

before a large amount of Li are extracted.

#### *4.3.2 Debonding analysis during lithiation at different charge rate*

The initial crack is present at the central and the surface of the patterned Si and the cohesive element is inserted, leading to the creation of new surface as shown in Fig. 4.4(a). Crack within a cohesive element is taken to occur if the total mixed mode relative displacement,  $\delta_m$  in an element has reached a value equal to the mixed-mode damage initiation displacement,  $\delta_m^0$ .

Mode I and Mode II debonding behavior from an initial crack at the internal point and surface is investigated. In an early lithiation, Mode I debonding suddenly increases in the central region and induces the crack growth from this crack tip in Fig. 4.4(b). This failure hinders Li diffusion in the Si. However, the relative displacement in Mode I decreases as further lithiation takes place near the crack because the additional chemical strain is placed on there and reduces the relative displacement. At the surface points Mode I debonding does not occur in an early lithiation due to the volume expansion, but according to the increase of the internal strains such as the elastic, plastic and chemical strains, push-out effects develop on the surface, hence the Mode I debonding is induced and increase with lithiation in Fig. 4.4(c). As the charge rate is higher, the relative displacement in Mode I at both

points increase and the rate dependency of the debonding in the central point is more prominent than that seen on the surface.

Mode II debonding is not observed in central point due to the symmetric Li flux, while Mode II debonding on the surface increases, decreases, and increases subsequently with lithiation. Initially, the lateral expansion of the upper part in crack interface caused by the more Li raises the Mode II debonding, but the crack of the internal region results in a circumvention of Li and an increase of the lateral expansion of the lower part, thus both lateral expansion along the crack interface become compatible. During the further lithiation, the lateral expansion difference between two parts is getting larger reversely. The relative displacement in Mode II also increases as the charge rate is higher. In summary during the lithiation, the Mode I debonding is dominant mechanism to create the crack in internal region and relative displacement of Mode I is comparable to that of Mode II on the surface.

#### *4.3.3 Debonding analysis during delithiation at different charge rate*

In the early stage of delithiation, Mode I debonding also develops on the surface. As show in Fig. 4.5, when the charge rate like 1.68 (mA/cm<sup>2</sup>) and 1.96 (mA/cm<sup>2</sup>) cases is sufficient to generate complete debonding near the surface, Mode I and Mode II debonding grow markedly. This rapid crack growth near the

surface is associated with the discontinuity of Li concentration.

#### *4.3.4 Time and state of charge to crack onset*

The time to crack onset at the central point with respect to the charge rate is illustrated in Fig. 4.6(a). The time to crack onset is a monotonical decrease with the function of charge rate. In contrast, in Fig.4.6(b), the SOC (state of charge) to crack onset at the central point keeps almost constant value no matter what charge rate are imposed thus SOC determines the condition for the initiation of a crack. This means that high charge rate does not necessarily influence on the crack onset during the lithiation. And the very small amount of Li plays a critical role in the crack onset.

#### *4.3.5 Crack length at different charge rate*

During the lithiation, the crack is initiated at the center of the patterned Si where Mode I debonding is the most common and typically the dominant mode of failure. The crack and propagates to the surface rapidly and the total crack length during the lithiation is directly proportional to the charge rate which is described by Fig. 4.7(a). While during the delithiation, the complete debonding on the surface is found at only high charge rate condition such as 1.68 (mA/cm<sup>2</sup>) and 1.96

(mA/cm<sup>2</sup>) as shown in Fig.4.7(b). As mentioned in the previous paragraph, the Li concentration discontinuity is strongly correlated with the crack advance in the Si. For that reason, once the crack develops, it accelerates additional crack propagation mechanism. So it is important the crack is not revealed in the first place by controlling charge rate or Si morphology. At highest charge rate, 1.96 (mA/cm<sup>2</sup>), the patterned Si shows complete debonding along the length of cohesive element and it is generally considered the huge capacity loss factor resulting from the active particle loss.

#### *4.3.6 Crack effects on the electrochemical response*

Figure 4.8 shows the electrochemical response of the patterned Si with different charge rate. Even though the internal crack exists within the Si, the capacity loss is not significant because Li-ion can move around the crack and Li is inserted (extracted) from every exposed surface of the body. This observation suggests that huge capacity loss during electrochemical cycling is associated with the complete debonding. Nevertheless, the electrochemical degradation (Capacity loss) increases with a charge rate as shown in Fig. 4.9

#### *4.3.7 Breakthrough in the patterned Si*

Based on our simulation results, we propose a new shape of the patterned Si as shown in Fig. 4.10. It can overcome the identified drawbacks. A Large amount of Li are trapped inside the patterned Si after 1 cycle and high charge rate operation condition induces a large crack within the Si so that the capacity fade is inevitable. To conclude, the proposed hollow-core cube shape enhances the mechanical and the electrochemical performance of patterned Si. First, the hollow structure relaxed the internal stress and prevent the crack generation during the lithiation and delithiation.

In Fig.4.11, Mode I and Mode II debonding during lithiation are compared when there is a hollow space in the bottom or not. Especially Mode I debonding at the central point decreases significantly during the lithiation, which brings favorable influence on a whole debonding mechanism.

Furthermore, new shape reduces the Li trapping within the Si by decreasing in the transfer path of the lithium, so that the specific capacity of the battery is increased during the charge and the discharge as shown in Fig. 4.12. Even if compared with the “without crack” case, it shows that the expected capacity in the hollow structure is larger in the specific capacity.

#### **4.4 Remarks**

We investigate the mechanical and electrochemical degradation in the patterned Si. The mixed-mode failure is considered for the fracture behavior of the patterned Si and Butler-Volmer equation for electrode kinetics is used to obtain the cell's voltage and capacity. In an early lithiation, Mode I debonding suddenly increases in the central region and induces the crack growth from this crack tip. This failure hinders Li diffusion in the Si and increases the inhomogeneity of Li within the Si. Taking into account the impacts of charge/discharge rate condition, the SOC (state of charge) to crack onset at the central point keeps almost constant value no matter what charge rate are imposed thus SOC determines the condition for the initiation of a crack. However, the total crack length during the lithiation is directly proportional to the charge rate. In an electrochemical response of the patterned Si with different charge rate, even if the internal crack exists within the Si, the capacity loss is not significant because Li-ion can move around the crack and Li is inserted (extracted) from every exposed surface of the body.

Based on our simulation results, we propose a new shape of the patterned Si that enhances the mechanical and electrochemical.

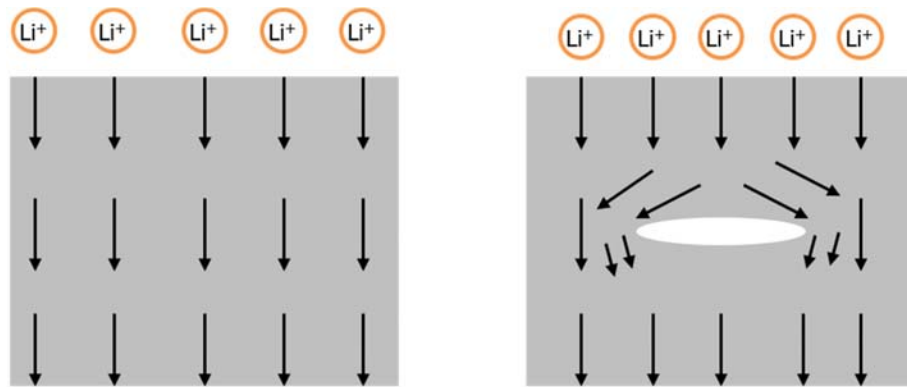


**Fig. 4.1** When there is a crack within the active material, the lithium needs to diffuse around the crack.

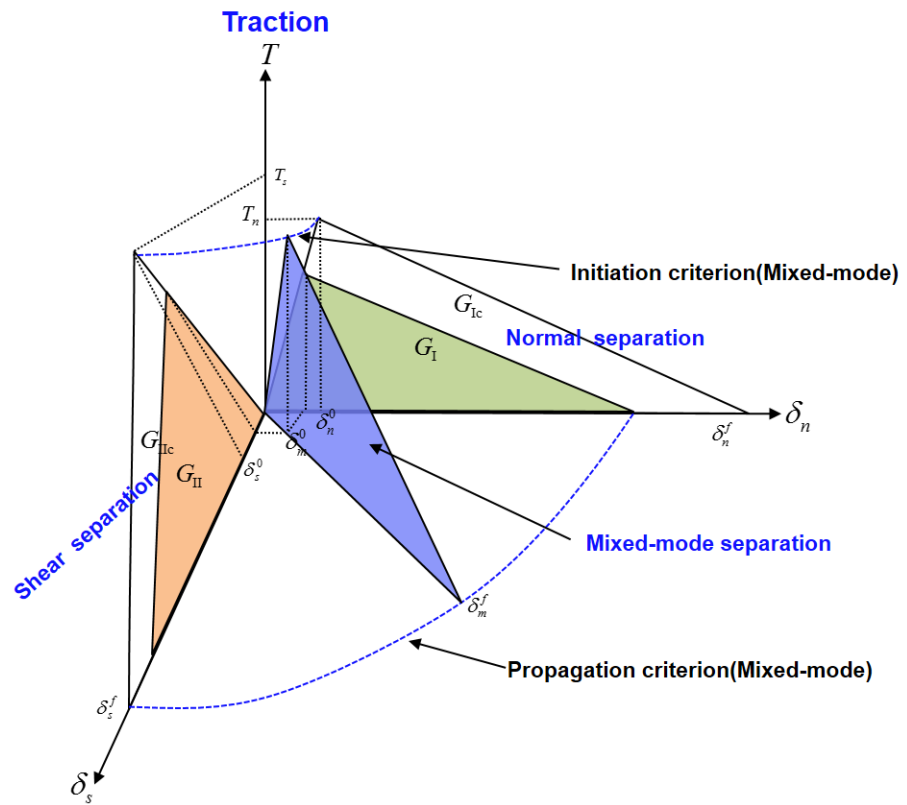


**Fig. 4.2** Mixed-mode delamination for the bi-linear traction-separation law.

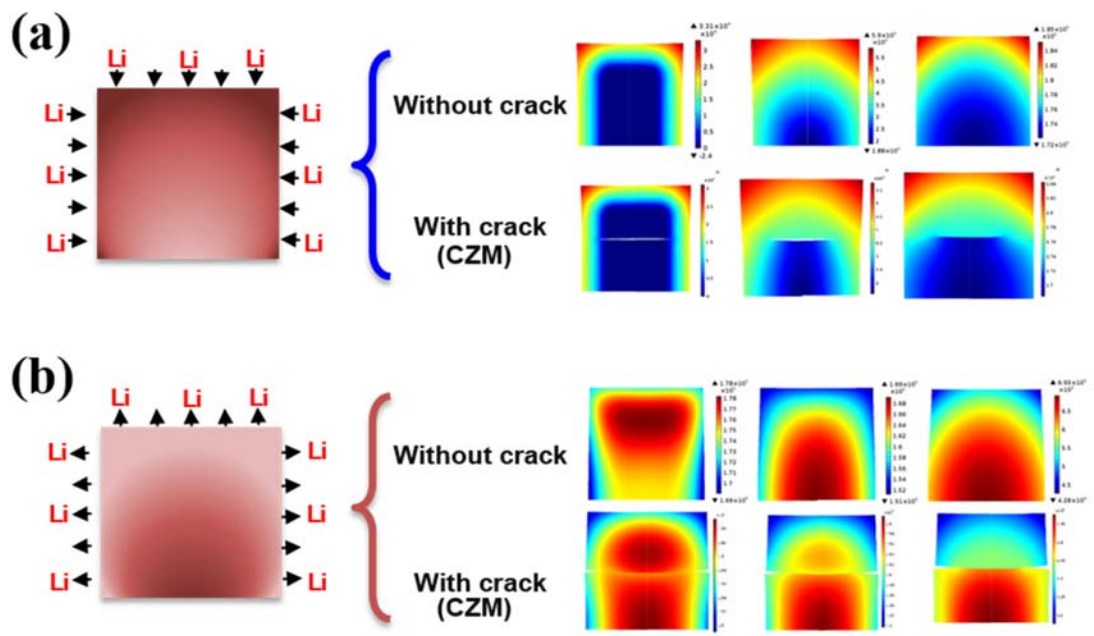
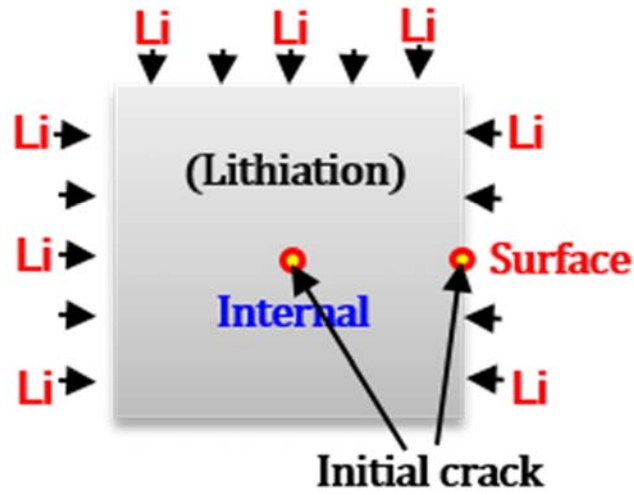
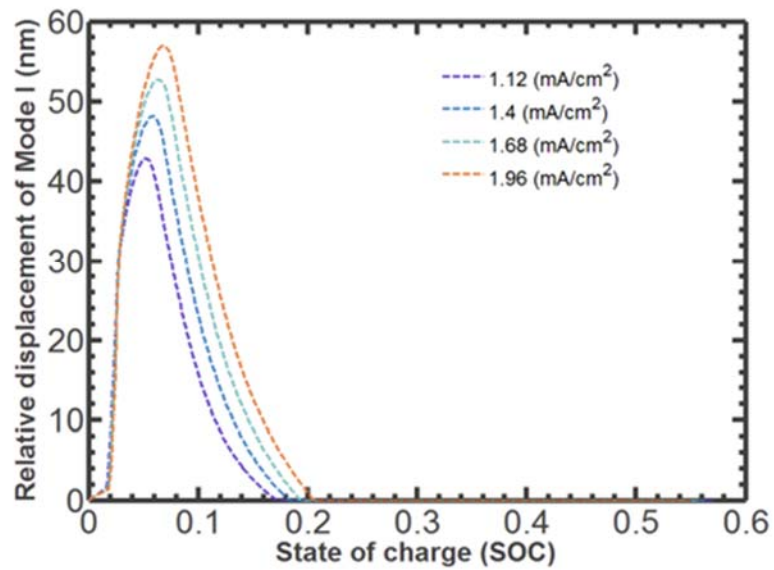


Fig. 4.3 Li distribution in a patterned Si during lithiation (a) and delithiation (b).

(a)



(b)



**Fig. 4.4** The initial crack is present at the central and the surface of the patterned Si (a), Mode I and Mode II debonding variation at the central point and on the surface (b) ~ (d).

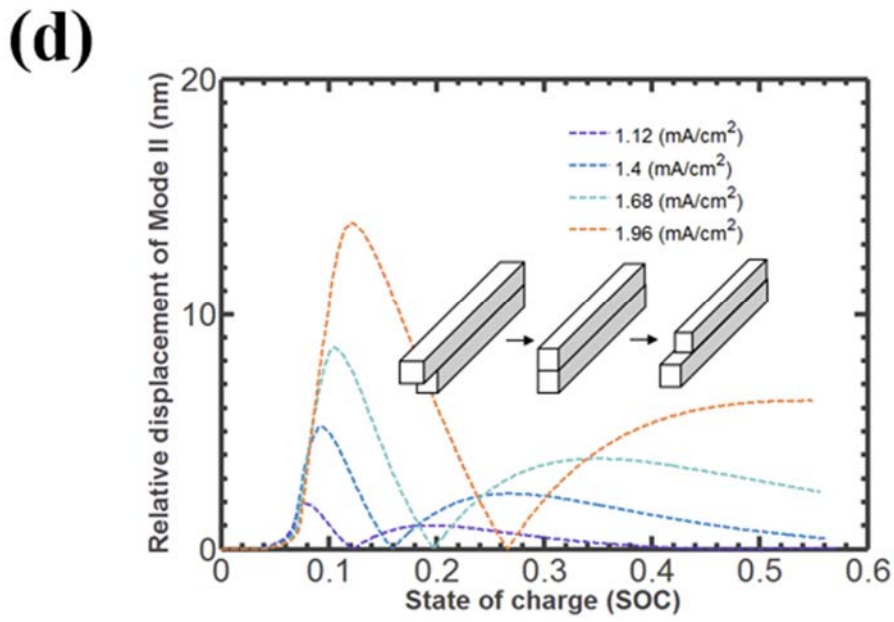
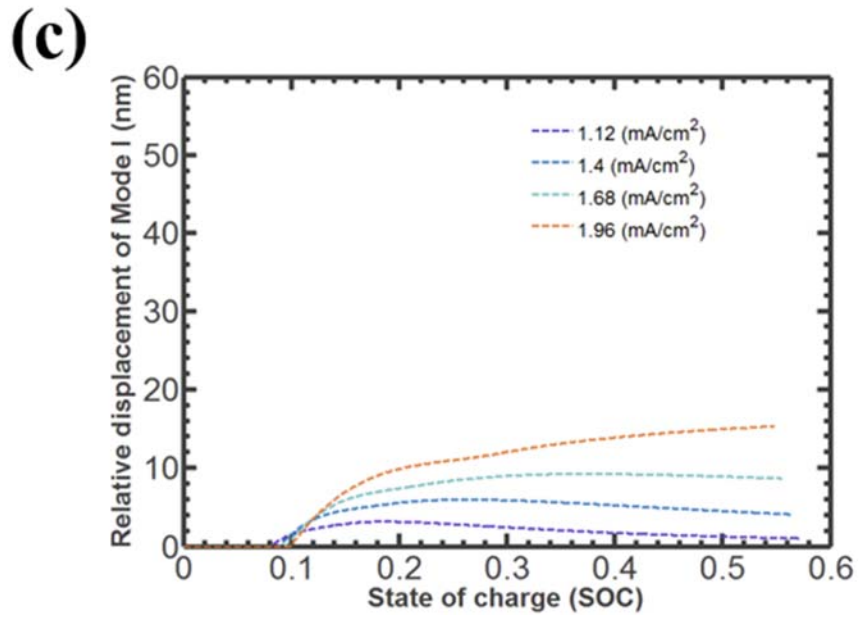


**Fig. 4.4** The initial crack is present at the central and the surface of the patterned Si (a), Mode I and Mode II debonding variation at the central point and on the surface (b) ~ (d).

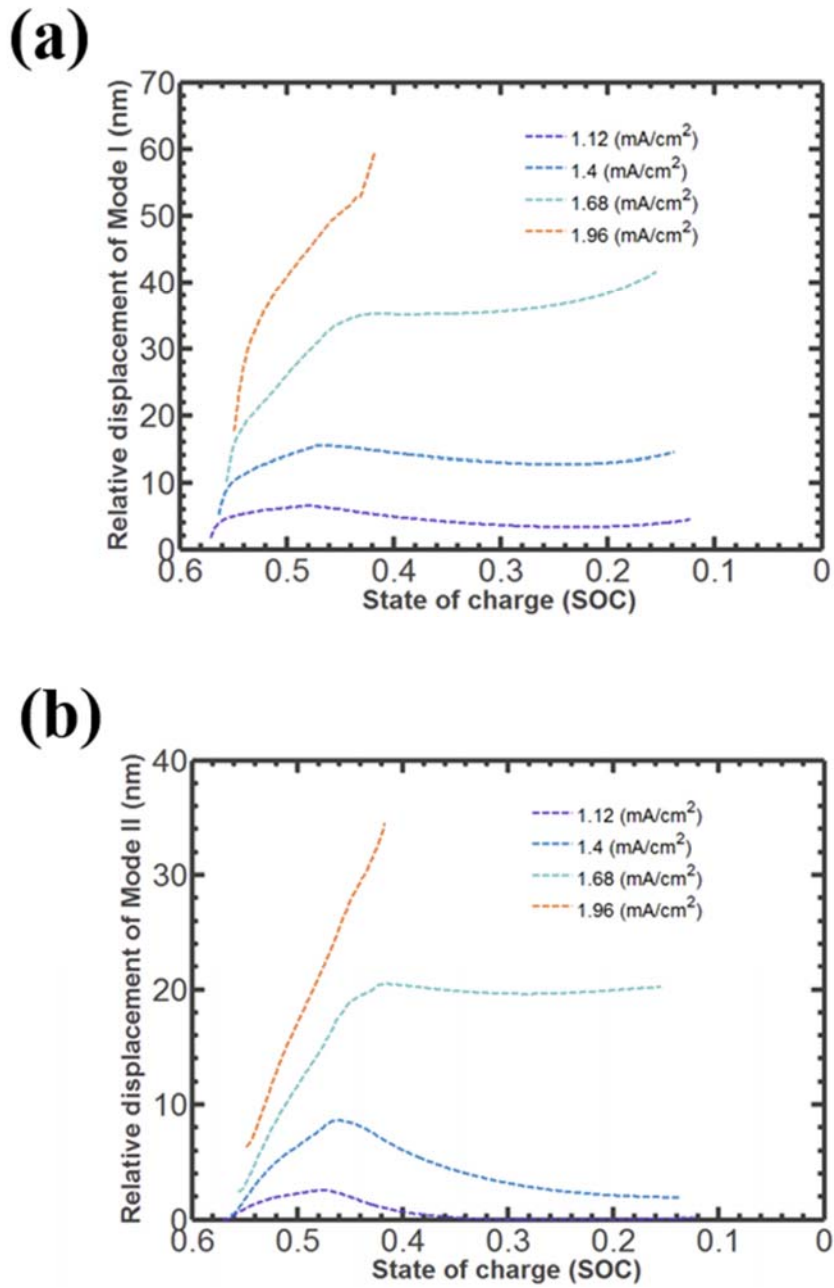


**Fig. 4.5** During delithiation, Mode I (a) and Mode II (b) debonding variation and on the surface.

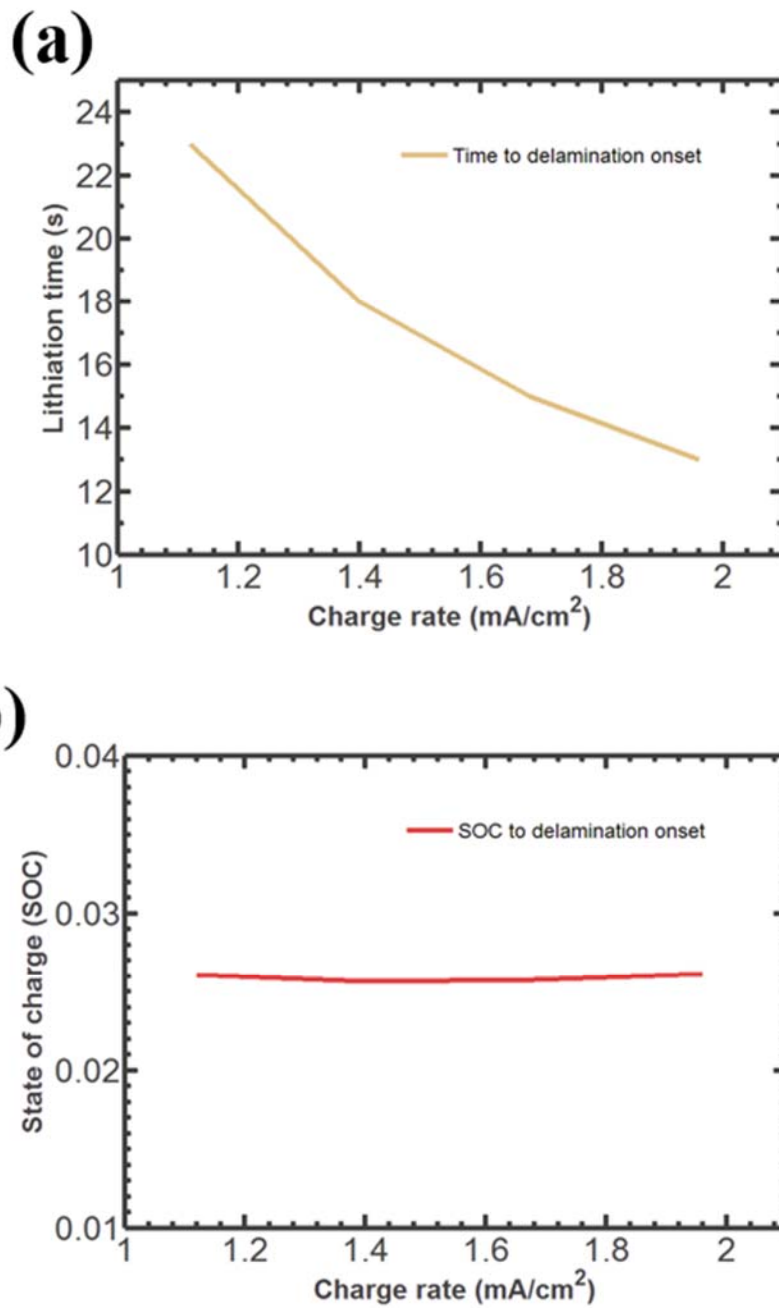


**Fig. 4.6** Time and SOC to crack onset at the central point with respect to the charge rate.

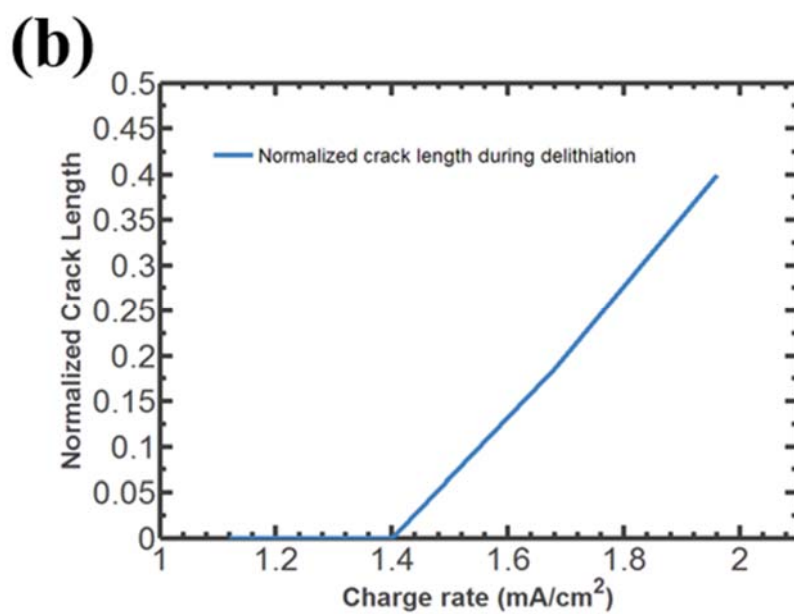
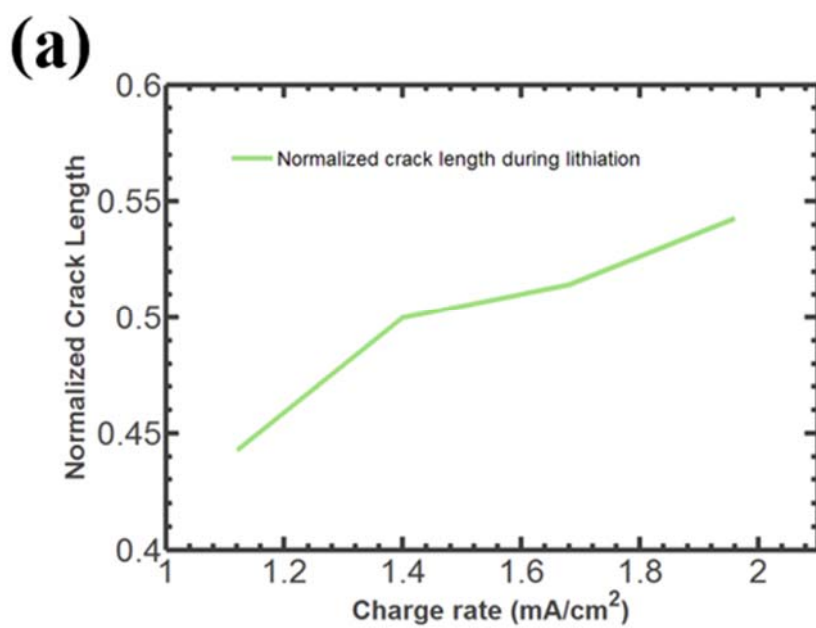


**Fig. 4.7** Crack length with respect to the charge rate: during lithiation (a), during delithiation (b) and during cycling (c).

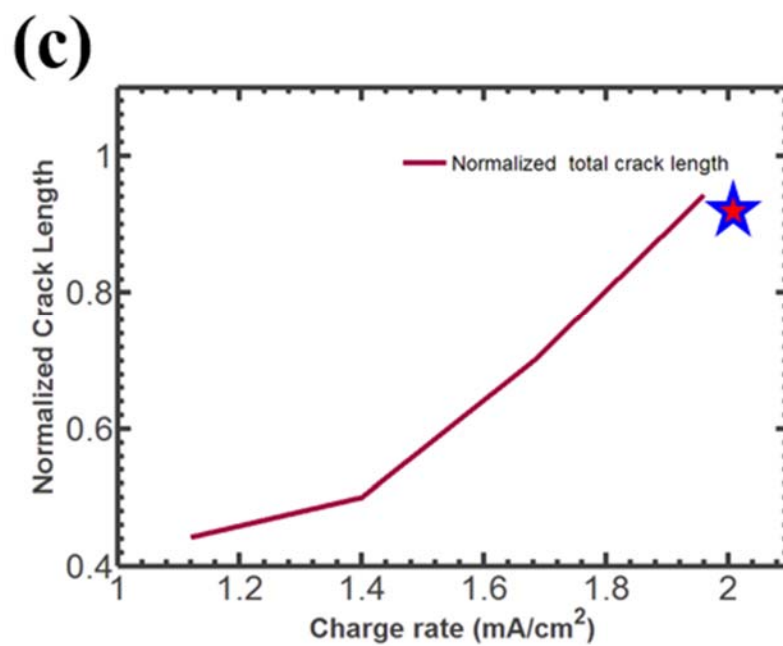


**Fig. 4.7** Crack length with respect to the charge rate: during lithiation (a), during delithiation (b) and during cycling (c).

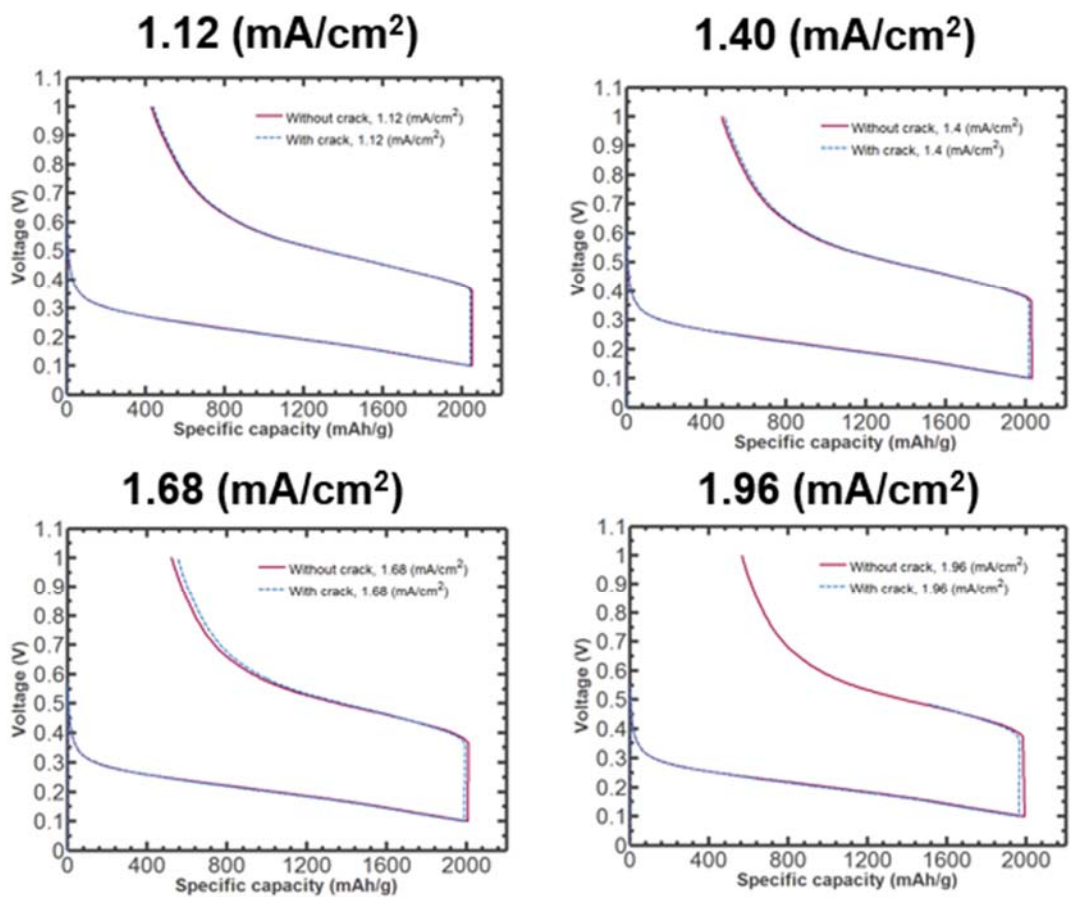


**Fig. 4.8** Electrochemical comparison of the patterned Si with different charge rate.

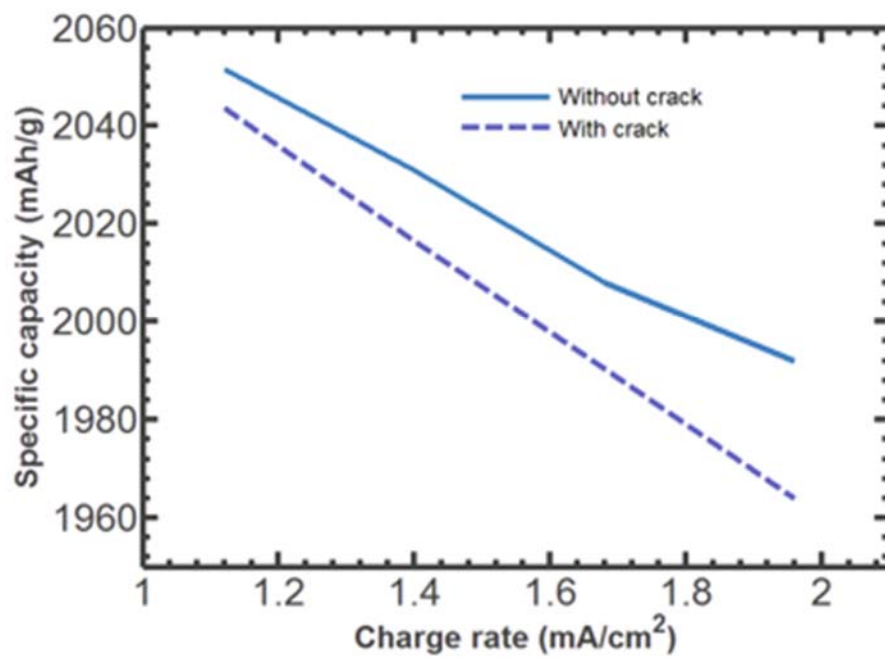


**Fig. 4.9** Capacity loss increases with a charge rate.

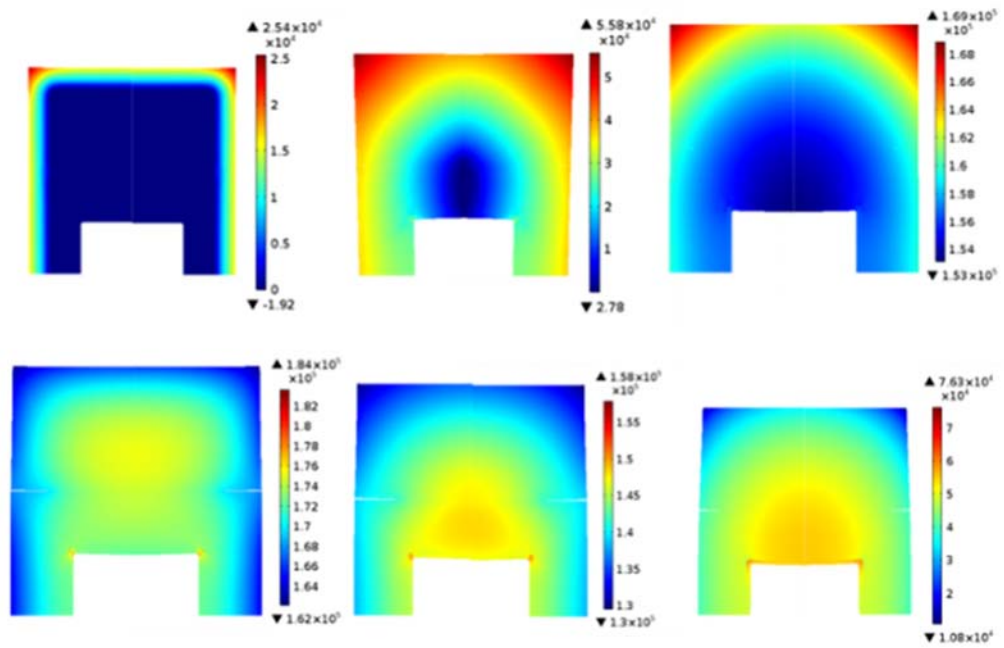


**Fig. 4.10** New shape of the patterned Si is proposed to overcome the identified drawbacks.

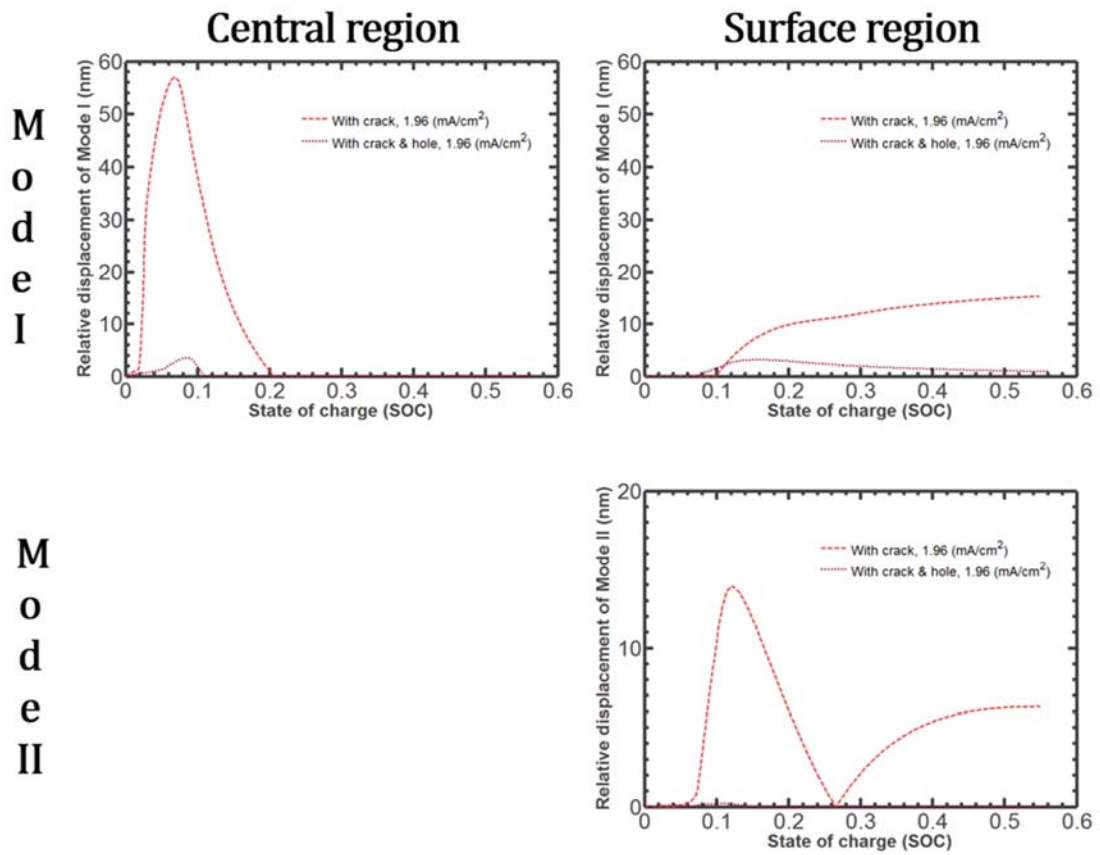


**Fig. 4.11** Comparison of Mode I and Mode II debonding during lithiation, when there is a hollow space in the bottom or not.

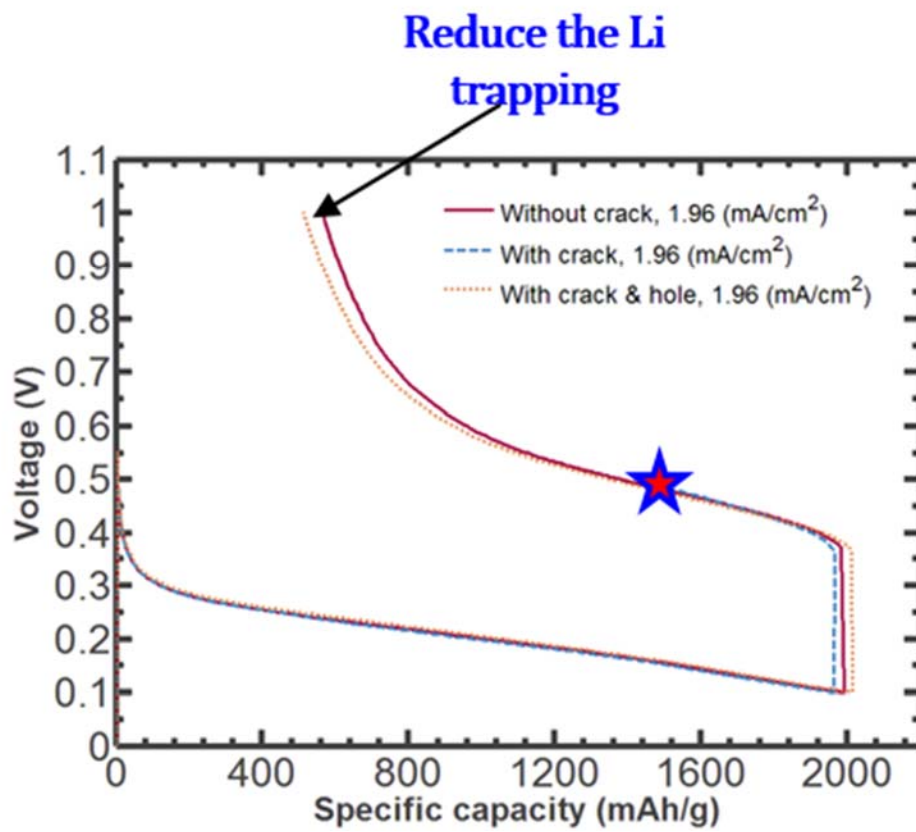


**Fig. 4.12** Comparison of hollow structure model with “without crack” and “with crack” model.

# Chapter 5

## Conclusion

This chapter summarizes the main conclusions describing in the preceding chapters and discusses the contribution of this dissertation. Future work for continuing battery research is suggested.

In this dissertation, diffusion-induced stress model, cohesive zone model, and the multiscale electrochemical model are proposed to better understand the physical phenomena takes place in the Li-ion battery system. In particular, the mechanical and electrochemical degradation in Si anode materials for the LIB are investigated.

In chapter 2, The fracture mechanism of crystalline Si nanowires is analyzed based on the nonlinear large deformation theory and bi-linear cohesive zone model. The crack is initiated on its surface of Si NWs and propagates to the center after the amount of Li inserted depending its size. Simulation results demonstrate that a

critical size of Si NW to avoid the crack nucleation is the radius of  $\sim 50\text{nm}$ , which is reasonable agreement with experimental results. In addition, we identify the safe range of state of charge in Li. When Si is lithiated within the safe amount of Li, mechanical and electrochemical performances will be improved because the core Si acts as the mechanical backbone for electrode material and the electrical pathway for electrons from the substrate to the lithiated Si.

In chapter 3, we proposed and discussed an electrochemical multiscale model to understand the electrochemical behavior of Si thin film anodes during discharge/charge cycling. In the multiscale framework, the stress-dependent energy barrier for the migration of lithium and the molar excess Gibbs free energy are considered. These effects significantly influence on the nonlinear distribution of the Li concentration and macroscopic kinetics. Multiscale simulation results predict the hysteresis of a potential capacity of a-Si thin film anode, matching well with the experimental data. We found that our multi-scale model is especially applicable to a high-capacity anode undergoing a high C-rate condition.

In chapter 4, We investigate the relation between the electrochemical performance of LIB and the crack growth with taking into account the impacts of charge/discharge rate condition in the patterned Si. A crack in silicon is regarded as the critical reason for the capacity reduction in lithium ion batteries due to the

inhomogeneity of Li within the Si and the isolation of Si resulting from complete debonding. The mixed-mode failure is applied for the fracture behavior of the patterned Si and Butler-Volmer equation for electrode kinetics is used to obtain the cell's voltage and capacity. As a result, it is found that Mode I debonding is the main factor to induce the crack within the Si and the SOC to crack onset at the central point keeps almost constant value no matter what charge rate are considered. But, the final crack length during the lithiation is directly proportional to the charge rate. In an electrochemical response of the patterned Si, it should be noted that even if the internal crack generated within the Si, the capacity loss is not significant because Li-ion can move around the crack and Li is inserted (extracted) from every exposed surface of the body. From our simulation results, we propose a new shape of the patterned Si that enhances the mechanical and electrochemical. The proposed hollow-core cube relaxes the internal stress and prevents the crack generation during the lithiation and delithiation. In particular, Mode I debonding at the central point decreases significantly during the lithiation, which brings favorable influence on a whole debonding mechanism. Furthermore, new shape reduces the Li trapping within the Si by decreasing in the transfer path of the lithium, so that the specific capacity of the battery is increased during the charge and the discharge.

The most important contributions of this dissertation are the improved understanding of the physical phenomena such as the mechanical and the electrochemical behavior in Si anode materials and providing the optimized electrochemical reaction condition and the design of Si anode for the better performance LIB systems.

For future work, the anisotropic expansion observed in recently experimental study should be considered. The lithiation reaction rate oriented along (110) crystallographic planes is the fastest in Li diffusion for the crystalline Si [111]. The crack is initiated and propagates at the tilted direction between two (100) planes during lithiation because of the stress concentration in this plane [46].

In addition, the coating layer effects on the structural stability of Si during lithiation should be explored. Applying surface coatings mitigate the expansion of  $\text{Li}_x\text{Si}$  and influence on the fracture behavior. The coating method reveals the improvement of rate capability and cycle life of LIBs. The type of coating material and the coating thickness could exhibit different mechanical and electrochemical response of Si. Recently it is reported that as the coating thickness increases, the volume expansion shows isotropic with one randomly oriented longitudinal crack because the large stress slows down the reaction kinetics [112]. But the detailed mechanical and electrochemical mechanism is largely unclear. The advanced

simulation model should be developed to give a better understanding of the failure mechanisms and to identify unknown phenomena affecting the battery performance.

And the formation of the solid electrolyte interface (SEI) needs to be considered for accurately predict the battery performance. The SEI not only affects the Li diffusion but also contributes to the early capacity loss. Therefore, we should implement the contribution of the SEI to the advanced simulation model.

# A. Appendix

## A.1 Cohesive zone model for a one phase lithiation

One phase diffusion model is commonly used to predict diffusion induced swelling of amorphous silicon (a-Si) with a gradually varying Li distribution [113, 114]. To investigate the difference between fracture mechanisms of c-Si and a-Si, we perform a one-phase diffusion simulation for nanowire of the radius  $R = 200\text{ nm}$ . Herein, we consider the general Hook's law to mimicking a one-phase lithiation process. Li concentration-dependent Young's modulus for an a-Li<sub>x</sub>Si varies from 90GPa (raw) to 40GPa (fully lithiated) and the yield strength,  $\sigma_y$  is set to be 2 GPa. Figure. A1(b) shows the variation of the hoop stresses over a radius of the nanowire that corresponds to the Li profiles in Fig. A1(a). As lithiation begins from the nanowire surface, the silicon near the surface becomes lithiated. Volumetric strain associated with Li diffusion is constrained by the present of adjacent materials, which induces compressive stresses for some distance beneath the surface (i.e., suppressing the fracture therein). While the hoop stress at the inner

region is tensile resulting from the concentration gradient in the nanowire. The corresponding stress distribution is also evaluated using the same cohesive zone method. However, it should be noted that this tensile stress at the inner part is not sufficient to induce the cracking of a-Si.

As lithium diffuses further into the center, the volumetric growth inside nanowire pushes against the material closer to the surface. This “push-out” effect gradually relaxes the compressive stresses near the surface, and it reverses initial compressive stress into tensile from 24 seconds. In addition, the hoop stresses in inner part are also relaxed due to the reduced gradient of Li. Such one phase lithiation model results are dramatically different to those obtained previously from two-phase modeling. The physical reason is as follows: As the discussion above, the Li induced stresses are determined in terms of competition of “differential expansion” effect and “push-out” effect with the curved phase boundary. The differential expansion effect results from the chemical strain mismatching in Si. The element near the surface elongates more than the element near the center because the Li concentration near the surface over that in the interior region is relatively high due to the inward flux of Li. Therefore, the element near the surface undergoes a compressive hoop stress under the strain misfit. The push-out effect is

the result of an additional chemical strain of newly lithiated inner part of  $\text{Li}_x\text{Si}$ . This effect relaxes the hoop compressive stress previously generated by the differential expansion effect and sometimes it contribute the transition from compressive stress to the hoop tensile stress at the outer electrode surface. However, in the case of the nanowire of radius  $R = 200 \text{ nm}$ , the contribution of push-out does not provide large enough tensile stress to induce the crack on its surface. This is a contrast to the two-phase model for c-Si, where this push out effect is sufficient to generate the crack in the surface layer.

When the nanowire size is large, the internal cracking arising from the hoop tensile stress caused by the differential expansion effect is observed in nanowire of radius  $R = 500 \text{ nm}$  (Fig. A2). The crack is initiated from a center instead of a surface of the nanowire and propagates toward the surface at the early stage of lithiation.

## **A.2 Energy release rate partitions in cohesive zone model**

Although energy release rate partitions are included in the cohesive element, their individual values are not identified in COMSOL Multiphysics Package so cohesive energy release rate has to be obtained by integrating tractions and

separations. The integrating method can be classified as a local and global approach based on the cohesive zone size in literature.

The Mode I energy release rate partitions with a global approach which is integrating of energy over the entire cohesive zone. The following integration in Eq. A1 is performed along the cohesive surface to calculate the global Mode I energy release rates.

$$G_{Ic} = \int_0^l \sigma \frac{\partial \delta}{\partial x} dx \quad (A1)$$

where  $l$  is the entire length of the integrated cohesive surface,  $\sigma$  and  $\delta$  are normal stress and displacement of the cohesive element respectively.

Above integrations are also calculated numerically using output value for cohesive elements.

$$G_{Ic} = \sum_n^{n-1} \frac{\sigma_i + \sigma_{i+1}}{2} (\delta_i - \delta_{i+1}) \quad (A2)$$

where  $n$  is the number of nodes in a cohesive element on the bottom or top surface,  $\sigma$  and  $\delta$  are stress and displacement components.

### **A.3 Effect of the shape of cohesive zone model**

Cohesive process zone where the surface tractions are non-zero is shown in Fig. A3(a). The crack process occurs within this cohesive process zone and it takes into account through the traction-separation relations. The typical traction-separation relation is shown in Fig. A3(b). The length of cohesive process zone is between point A where the maximum value of  $\delta$  and point C where the separation is not taken place yet  $\delta = 0$ . At point A representing the physical crack tip, the material has completely separated and the traction has vanished. The crack tip should be located between two points where the cohesive traction is maximum (i.e., point B). The process zone stretching from point C to point B is defined as ‘forward region’ and the region stretching from point B to point A is defined as ‘wake region’ respectively. The forward area is defined as ‘extrinsic cohesive energy ( $G_{\text{ext}}$ ), it is an inherent property of the material, while the wake area is defined as intrinsic cohesive dissipation ( $G_{\text{int}}$ ) in Fig. A3(b). The crack propagation is generated by extrinsic dissipation resulting from the microstructural damage, while the crack growth is impeded by the intrinsic dissipation and elastic unloading takes place. Both consumed energy dissipated into the material and the crack.

The ratio of extrinsic dissipation compared to intrinsic dissipation influence on the rate of cohesive zone energy absorption. Therefore, we investigate that different shape of CZM on the development of cohesive zone energy absorption to understand fracture processes in a different type of ductile materials.

The slope of traction-separation relations determines the ratio of extrinsic dissipation compared to intrinsic dissipation.

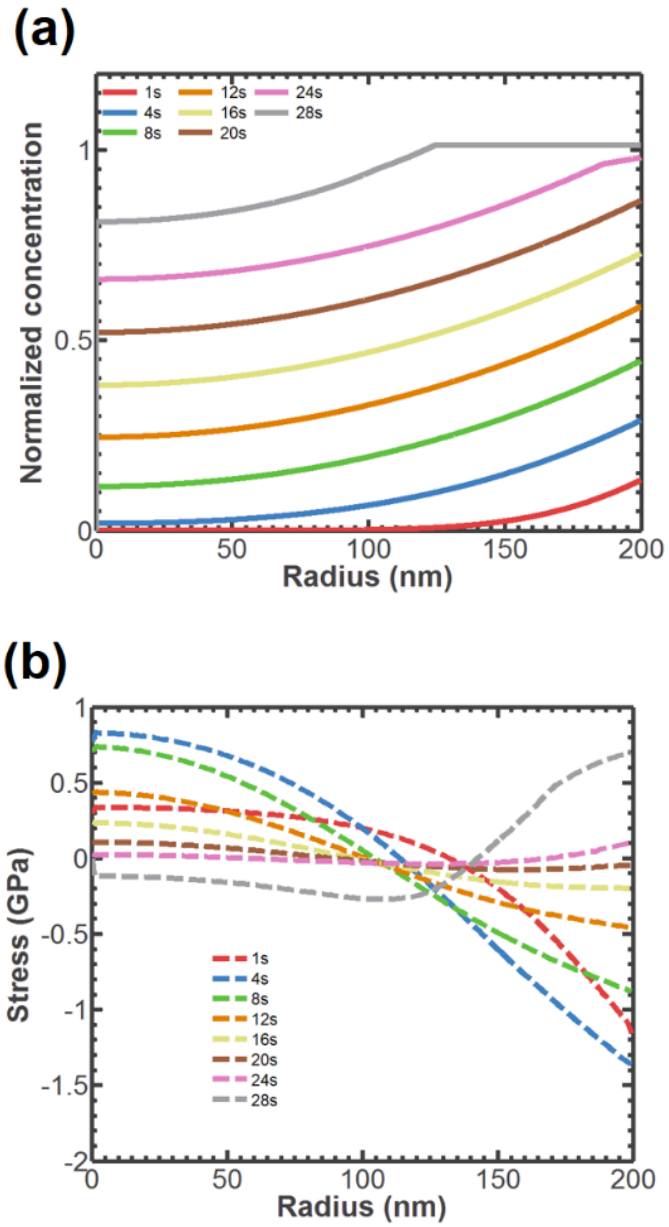
To describe the shape of CZM, we define shape factor  $\Gamma$  as

$$\Gamma = \frac{G_{\text{ext}}}{G_{\text{init}}} \quad (\text{A3})$$

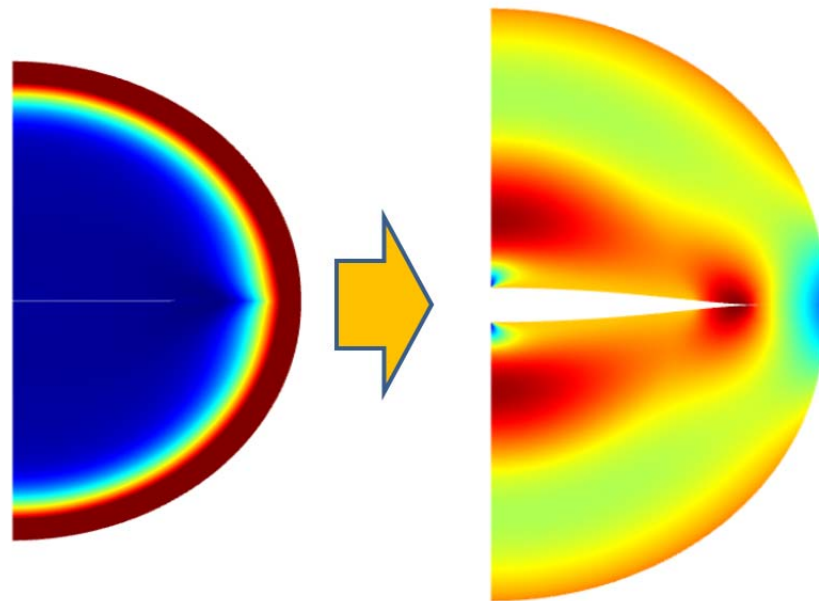
As the slope of traction-separation relation,  $K$  increases, the shape factor  $\Gamma$  decreases. It is obvious that shape factor increase, the load required to initiate the crack also increase.

Figure A5 shows the cohesive energy release rate as a function of lithiation time for  $\Gamma = 0.11, 1, 1.67$ . Even for a fixed material properties (i.e.,  $E(c), \nu, \sigma_y(c), N_s$ ), the effect of the shape factor on cohesive energy release rate cannot be overlooked. The transition region where the slope rises to the horizontal steady state is different depending on the shape factor. The transition region for

$\Gamma = 1.67$  is more narrow (i.e., steeper) than the transition region for  $\Gamma = 0.11$ . Furthermore, the initiation of crack growth is delayed for  $\Gamma = 1.67$  because the larger  $\Gamma$  corresponding to the higher extrinsic energy of dissipation in the forward region means the larger energy needed to initiate the crack. However, after the full development of cohesive zone on the crack face along the crack growth direction, the maximum cohesive release rate is steady state and is not sensitive to the shape factor  $\Gamma$ . When  $\delta = \delta^0$  the cohesive zone is fully developed and the steady state value of  $G$  is reached. During this crack growth, the material also undergoes not cohesive dissipation within the crack tip region but also additional dissipation arising from plasticity consuming of the external work. Before the crack initiated, the plastic zone is occurred that contribute to the energy release rate required for the crack initiation.



**Fig. A1** (a) Radial Li distribution at selected time during lithiation in amorphous silicon, (b) corresponding hoop stress evolution.



**Fig. A2** Von-mises stress contours in the amorphous silicon nanowire of radius  $R = 500 \text{ nm}$  , the crack is initiated from a center instead of a surface of the nanowire and propagates toward the surface.

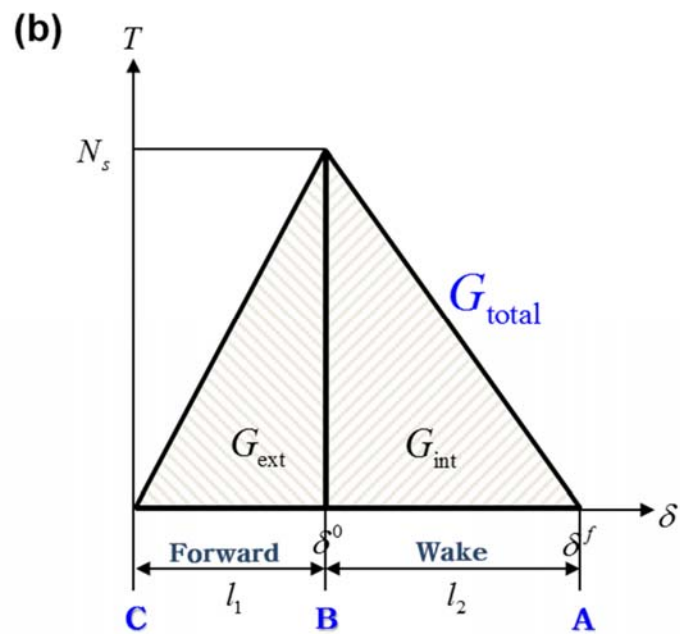
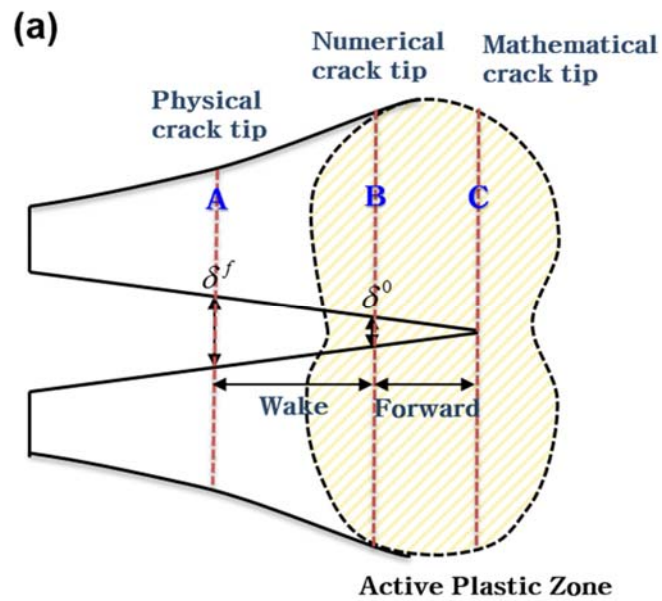


**Fig. A3** (a) Illustration of the embedded cohesive process zone, (b) Bilinear traction-separation constitution of cohesive zone model, it is composed of an intrinsic dissipation ( $G_{\text{int}}$ ) and an extrinsic dissipation ( $G_{\text{ext}}$ ).

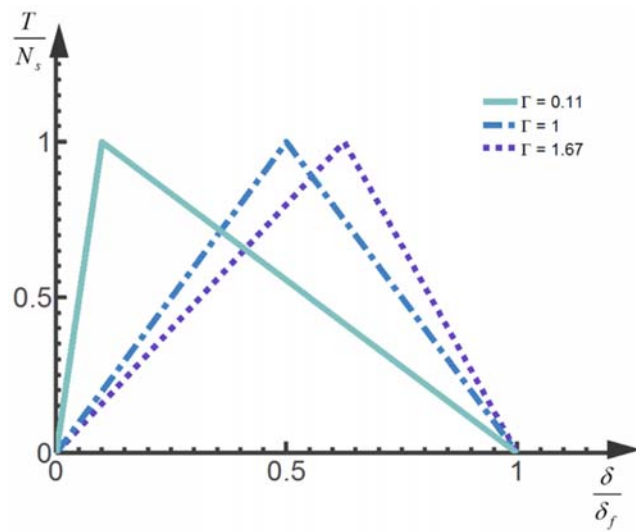


**Fig. A4** Variation of the shape of CZM according to the different shape factor.

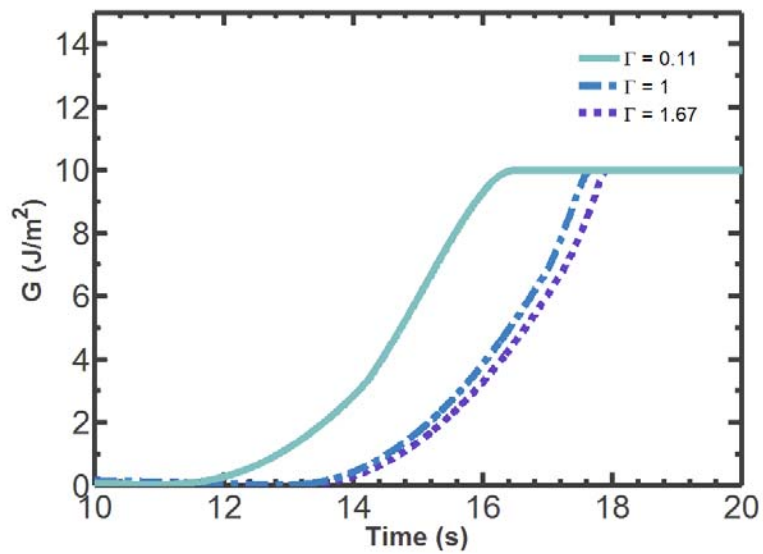


**Fig. A5** The cohesive energy release rate as a function of lithiation time for  $\Gamma = 0.11, 1, 1.67$ .

## Bibliography

- [1] P. Mukherjee, S. Pannala, J. Turner, C. Daniel, J. Besenhard, in, Wiley-VCH Verlag GmbH & Co. KGaA Weinheim, 2011.
- [2] J.M. Tarascon, M. Armand, *Nature*, 414 (2001) 359-367.
- [3] J.C. Hunter, *J Solid State Chem*, 39 (1981) 142-147.
- [4] C. Lin, A.H. Tang, H. Mu, W.W. Wang, C. Wang, *J Chem-Ny*, (2015).
- [5] D.Y. Wang, X.D. Wu, Z.X. Wang, L.Q. Chen, *J Power Sources*, 140 (2005) 125-128.
- [6] H.F. Wang, Y.I. Jang, B.Y. Huang, D.R. Sadoway, Y.T. Chiang, *J Electrochem Soc*, 146 (1999) 473-480.
- [7] A. Chakraborty, N. Ramakrishnan, *Comp Mater Sci*, 69 (2013) 455-465.
- [8] M.B. Pinson, M.Z. Bazant, *J Electrochem Soc*, 160 (2013) A243-A250.
- [9] J.L. Lei, L.J. Li, R. Kostecki, R. Muller, F. McLarnon, *J Electrochem Soc*, 152 (2005) A774-A777.
- [10] D. Aurbach, *J Power Sources*, 89 (2000) 206-218.
- [11] M.N. Obrovac, L. Christensen, *Electrochem Solid St*, 7 (2004) A93-A96.
- [12] C.K. Chan, H.L. Peng, G. Liu, K. McIlwrath, X.F. Zhang, R.A. Huggins, Y. Cui, *Nat Nanotechnol*, 3 (2008) 31-35.
- [13] W.J. Zhang, *J Power Sources*, 196 (2011) 13-24.

- [14] Y.S. Choi, M. Pharr, K.H. Oh, J.J. Vlassak, *J Power Sources*, 294 (2015) 159-166.
- [15] J.L. Goldman, B.R. Long, A.A. Gewirth, R.G. Nuzzo, *Adv Funct Mater*, 21 (2011) 2412-2422.
- [16] X.H. Liu, L. Zhong, S. Huang, S.X. Mao, T. Zhu, J.Y. Huang, *Acs Nano*, 6 (2012) 1522-1531.
- [17] X.H. Liu, L.Q. Zhang, L. Zhong, Y. Liu, H. Zheng, J.W. Wang, J.H. Cho, S.A. Dayeh, S.T. Picraux, J.P. Sullivan, S.X. Mao, Z.Z. Ye, J.Y. Huang, *Nano Lett*, 11 (2011) 2251-2258.
- [18] Y. Yao, M.T. McDowell, I. Ryu, H. Wu, N.A. Liu, L.B. Hu, W.D. Nix, Y. Cui, *Nano Lett*, 11 (2011) 2949-2954.
- [19] C.J. Yu, X. Li, T. Ma, J.P. Rong, R.J. Zhang, J. Shaffer, Y.H. An, Q. Liu, B.Q. Wei, H.Q. Jiang, *Adv Energy Mater*, 2 (2012) 68-73.
- [20] S.P.V. Nadimpalli, V.A. Sethuraman, S. Dalavi, B. Lucht, M.J. Chon, V.B. Shenoy, P.R. Guduru, *J Power Sources*, 215 (2012) 145-151.
- [21] A.S. Arico, P. Bruce, B. Scrosati, J.M. Tarascon, W. Van Schalkwijk, *Nat Mater*, 4 (2005) 366-377.
- [22] M.J. Chon, V.A. Sethuraman, A. McCormick, V. Srinivasan, P.R. Guduru, *Phys Rev Lett*, 107 (2011) 045503.
- [23] X.H. Liu, H. Zheng, L. Zhong, S. Huan, K. Karki, L.Q. Zhang, Y. Liu, A. Kushima, W.T.

- Liang, J.W. Wang, J.H. Cho, E. Epstein, S.A. Dayeh, S.T. Picraux, T. Zhu, J. Li, J.P. Sullivan, J. Cumings, C.S. Wang, S.X. Mao, Z.Z. Ye, S.L. Zhang, J.Y. Huang, *Nano Lett*, 11 (2011) 3312-3318.
- [24] S. Huang, F. Fan, J. Li, S. Zhang, T. Zhu, *Acta Mater*, 61 (2013) 4354-4364.
- [25] X.H. Liu, S. Huang, S.T. Picraux, J. Li, T. Zhu, J.Y. Huang, *Nano Lett*, 11 (2011) 3991-3997.
- [26] K.J. Zhao, M. Pharr, Q. Wan, W.L. Wang, E. Kaxiras, J.J. Vlassak, Z.G. Suo, *J Electrochem Soc*, 159 (2012) A238-A243.
- [27] K.J. Zhao, M. Pharr, S.Q. Cai, J.J. Vlassak, Z.G. Suo, *J Am Ceram Soc*, 94 (2011) S226-S235.
- [28] M. Pharr, K.J. Zhao, X.W. Wang, Z.G. Suo, J.J. Vlassak, *Nano Lett*, 12 (2012) 5039-5047.
- [29] H. Yang, S. Huang, X. Huang, F.F. Fan, W.T. Liang, X.H. Liu, L.Q. Chen, J.Y. Huang, J. Li, T. Zhu, S.L. Zhang, *Nano Lett*, 12 (2012) 1953-1958.
- [30] M.T. McDowell, I. Ryu, S.W. Lee, C.M. Wang, W.D. Nix, Y. Cui, *Adv Mater*, 24 (2012) 6034-6041.
- [31] T.K. Bhandakkar, H.J. Gao, *Int J Solids Struct*, 47 (2010) 1424-1434.
- [32] T.K. Bhandakkar, H.J. Gao, *Int J Solids Struct*, 48 (2011) 2304-2309.

- [33] A.F. Bower, P.R. Guduru, *Model Simul Mater Sc*, 20 (2012).
- [34] P. Zuo, Y.P. Zhao, *Phys Chem Chem Phys*, 17 (2015) 287-297.
- [35] M.E. Gurtin, E. Fried, L. Anand, *The mechanics and thermodynamics of continua*, Cambridge University Press, 2010.
- [36] D.S. Dugdale, *J Mech Phys Solids*, 8 (1960) 100-104.
- [37] G.I. Barenblatt, *Advances in applied mechanics*, 7 (1962) 55-129.
- [38] A. Needleman, *Journal of applied mechanics*, 54 (1987) 525-531.
- [39] H. Li, N. Chandra, *Int J Plasticity*, 19 (2003) 849-882.
- [40] V. Shenoy, P. Johari, Y. Qi, *J Power Sources*, 195 (2010) 6825-6830.
- [41] S.W. Lee, M.T. McDowell, L.A. Berla, W.D. Nix, Y. Cui, *P Natl Acad Sci USA*, 109 (2012) 4080-4085.
- [42] I. Ryu, J.W. Choi, Y. Cui, W.D. Nix, *J Mech Phys Solids*, 59 (2011) 1717-1730.
- [43] L.Q. Zhang, X.H. Liu, Y. Liu, S. Huang, T. Zhu, L.J. Gui, S.X. Mao, Z.Z. Ye, C.M. Wang, J.P. Sullivan, J.Y. Huang, *Acs Nano*, 5 (2011) 4800-4809.
- [44] B. Hertzberg, A. Alexeev, G. Yushin, *J Am Chem Soc*, 132 (2010) 8548-+.
- [45] M.H. Park, M.G. Kim, J. Joo, K. Kim, J. Kim, S. Ahn, Y. Cui, J. Cho, *Nano Lett*, 9 (2009) 3844-3847.
- [46] I. Ryu, S.W. Lee, H.J. Gao, Y. Cui, W.D. Nix, *J Power Sources*, 255 (2014) 274-282.

- [47] M. Pharr, Z.G. Suo, J.J. Vlassak, *Nano Lett*, 13 (2013) 5570-5577.
- [48] M.T. McDowell, S.W. Lee, W.D. Nix, Y. Cui, *Adv Mater*, 25 (2013) 4966-4984.
- [49] M.N. Obrovac, V.L. Chevrier, *Chem Rev*, 115 (2015) 2043-2043.
- [50] B. Hertzberg, J. Benson, G. Yushin, *Electrochem Commun*, 13 (2011) 818-821.
- [51] A. Mukhopadhyay, B.W. Sheldon, *Prog Mater Sci*, 63 (2014) 58-116.
- [52] T. Moon, C. Kim, B. Park, *J Power Sources*, 155 (2006) 391-394.
- [53] P. Arora, R.E. White, M. Doyle, *J Electrochem Soc*, 145 (1998) 3647-3667.
- [54] M.R. Zamfir, H.T. Nguyen, E. Moyon, Y.H. Lee, D. Pribat, *J Mater Chem A*, 1 (2013) 9566-9586.
- [55] J.K. Yoo, J. Kim, H. Lee, J. Choi, M.J. Choi, D.M. Sim, Y.S. Jung, K. Kang, *Nanotechnology*, 24 (2013).
- [56] S.P.V. Nadimpalli, V.A. Sethuraman, G. Bucci, V. Srinivasan, A.F. Bower, P.R. Guduru, *J Electrochem Soc*, 160 (2013) A1885-A1893.
- [57] J. Christensen, J. Newman, *J Solid State Electr*, 10 (2006) 293-319.
- [58] K.J. Zhao, G.A. Tritsarlis, M. Pharr, W.L. Wang, O. Okeke, Z.G. Suo, J.J. Vlassak, E. Kaxiras, *Nano Lett*, 12 (2012) 4397-4403.
- [59] A.F. Bower, P.R. Guduru, V.A. Sethuraman, *J Mech Phys Solids*, 59 (2011) 804-828.
- [60] J. Moon, B. Lee, M. Cho, K. Cho, *J Power Sources*, 272 (2014) 1010-1017.

- [61] S. Chang, J. Moon, K. Cho, M. Cho, *Comp Mater Sci*, 98 (2015) 99-104.
- [62] V.B. Shenoy, P. Johari, Y. Qi, *J Power Sources*, 195 (2010) 6825-6830.
- [63] J. Newman, W. Tiedemann, *Aiche J*, 21 (1975) 25-41.
- [64] L. Cai, R.E. White, *J Electrochem Soc*, 156 (2009) A154-A161.
- [65] K.A. Smith, C.D. Rahn, C.Y. Wang, *Energ Convers Manage*, 48 (2007) 2565-2578.
- [66] D. Di Domenico, A. Stefanopoulou, G. Fiengo, *J Dyn Syst-T Asme*, 132 (2010).
- [67] M. Doyle, J. Newman, A.S. Gozdz, C.N. Schmutz, J.M. Tarascon, *J Electrochem Soc*, 143 (1996) 1890-1903.
- [68] M. Jagannathan, K.S.R. Chandran, *J Power Sources*, 247 (2014) 667-675.
- [69] X. Zhang, W. Shyy, A.M. Sastry, *J Electrochem Soc*, 154 (2007) S21-S21.
- [70] A.A. Franco, *Rsc Adv*, 3 (2013) 13027-13058.
- [71] G. Richardson, G. Denuault, C.P. Please, *J Eng Math*, 72 (2012) 41-72.
- [72] G. Kresse, J. Hafner, *Phys Rev B*, 48 (1993) 13115-13118.
- [73] G. Kresse, J. Furthmuller, *Phys Rev B*, 54 (1996) 11169-11186.
- [74] P.E. Blochl, *Phys Rev B*, 50 (1994) 17953-17979.
- [75] G. Henkelman, B.P. Uberuaga, H. Jonsson, *J Chem Phys*, 113 (2000) 9901-9904.
- [76] V.L. Chevrier, J.R. Dahn, *J Electrochem Soc*, 156 (2009) A454-A458.
- [77] V.I. Levitas, H. Attariani, *J Mech Phys Solids*, 69 (2014) 84-111.

- [78] Y.H. An, H.Q. Jiang, *Model Simul Mater Sc*, 21 (2013).
- [79] Z.W. Cui, F. Gao, J.M. Qu, *J Mech Phys Solids*, 61 (2013) 293-310.
- [80] Stanley I. Sandler, "Chemical and Engineering Thermodynamics" by 2nd ed., , Wiley Subscription Services, Inc., A Wiley Company, 1989.
- [81] H. Haftbaradaran, J. Song, W.A. Curtin, H.J. Gao, *J Power Sources*, 196 (2011) 361-370.
- [82] J. Chen-Min Li, *MTA*, 9 (1978) 1353-1380.
- [83] H. Yang, F.F. Fan, W.T. Liang, X. Guo, T. Zhu, S.L. Zhang, *J Mech Phys Solids*, 70 (2014) 349-361.
- [84] N. Munichandraiah, L.G. Scanlon, R.A. Marsh, *J Power Sources*, 72 (1998) 203-210.
- [85] D. Danilov, P.H.L. Notten, *Electrochim Acta*, 53 (2008) 5569-5578.
- [86] T.D. Hatchard, J.R. Dahn, *J Electrochem Soc*, 151 (2004) A838-A842.
- [87] N. Ding, J. Xu, Y.X. Yao, G. Wegner, X. Fang, C.H. Chen, I. Lieberwirth, *Solid State Ionics*, 180 (2009) 222-225.
- [88] S. Pal, S.S. Damle, S.H. Patel, M.K. Datta, P.N. Kumta, S. Maiti, *J Power Sources*, 246 (2014) 149-159.
- [89] L. Chen, F. Fan, L. Hong, J. Chen, Y.Z. Ji, S.L. Zhang, T. Zhu, L.Q. Chen, *J Electrochem Soc*, 161 (2014) F3164-F3172.

- [90] V. Boovaragavan, V.R. Subramanian, *Electrochem Commun*, 9 (2007) 1772-1777.
- [91] M.N. Obrovac, L. Christensen, D.B. Le, J.R. Dahnb, *J Electrochem Soc*, 154 (2007) A849-A855.
- [92] X.H. Liu, J.W. Wang, S. Huang, F. Fan, X. Huang, Y. Liu, S. Krylyuk, J. Yoo, S.A. Dayeh, A.V. Davydov, S.X. Mao, S.T. Picraux, S. Zhang, J. Li, T. Zhu, J.Y. Huang, *Nat Nano*, 7 (2012) 749-756.
- [93] M.J. Chon, V.A. Sethuraman, A. McCormick, V. Srinivasan, P.R. Guduru, *Phys Rev Lett*, 107 (2011).
- [94] P. Arora, M. Doyle, A.S. Gozdz, R.E. White, J. Newman, *J Power Sources*, 88 (2000) 219-231.
- [95] V.A. Sethuraman, V. Srinivasan, J. Newman, *J Electrochem Soc*, 160 (2013) A394-A403.
- [96] S. Ohara, J.J. Suzuki, K. Sekine, T. Takamura, *Electrochemistry*, 71 (2003) 1126-1128.
- [97] U. Kasavajjula, C.S. Wang, A.J. Appleby, *J Power Sources*, 163 (2007) 1003-1039.
- [98] Y.H. Wang, Y. He, R.J. Xiao, H. Li, K.E. Aifantis, X.J. Huang, *J Power Sources*, 202 (2012) 236-245.
- [99] R. Teki, M.K. Datta, R. Krishnan, T.C. Parker, T.M. Lu, P.N. Kumta, N. Koratkar, *Small*, 5 (2009) 2236-2242.

- [100] N.T. Hieu, J. Suk, D.W. Kim, O.H. Chung, J.S. Park, Y. Kang, *Synthetic Met*, 198 (2014) 36-40.
- [101] V.A. Sethuraman, M.J. Chon, M. Shimshak, V. Srinivasan, P.R. Guduru, *J Power Sources*, 195 (2010) 5062-5066.
- [102] H.B. Chew, B.Y. Hou, X.J. Wang, S.M. Xia, *Int J Solids Struct*, 51 (2014) 4176-4187.
- [103] C.M. Park, J.H. Kim, H. Kim, H.J. Sohn, *Chem Soc Rev*, 39 (2010) 3115-3141.
- [104] B. Lu, Y.C. Song, J.G. Zhang, *J Power Sources*, 289 (2015) 168-183.
- [105] H. Haftbaradaran, X.C. Xiao, M.W. Verbrugge, H.J. Gao, *J Power Sources*, 206 (2012) 357-366.
- [106] J.P. Maranchi, A.F. Hepp, A.G. Evans, N.T. Nuhfer, P.N. Kumta, *J Electrochem Soc*, 153 (2006) A1246-A1253.
- [107] P. Barai, P.P. Mukherjee, *J Electrochem Soc*, 160 (2013) A955-A967.
- [108] C.G. Dávila, P.P. Camanho, M.F. de Moura, in: *Proceedings of the 42nd AIAA/ASME/ASCE/AHS/ASC structures. Structural dynamics and materials conference, Seattle, Washington, 2001*, pp. 16-19.
- [109] W.C. Cui, M.R. Wisnom, M. Jones, *Composites*, 23 (1992) 158-166.
- [110] M.L. Benzeggagh, M. Kenane, *Compos Sci Technol*, 56 (1996) 439-449.
- [111] S.W. Lee, M.T. McDowell, J.W. Choi, Y. Cui, *Nano Lett*, 11 (2011) 3034-3039.

[112] G. Sandu, L. Brassart, J.F. Gohy, T. Pardoën, S. Melinte, A. Vlad, *Acs Nano*, 8 (2014) 9427-9436.

[113] R. Chandrasekaran, A. Magasinski, G. Yushin, T.F. Fuller, *J Electrochem Soc*, 157 (2010) A1139-A1151.

[114] G. Bucci, S.P.V. Nadimpalli, V.A. Sethuraman, A.F. Bower, P.R. Guduru, *J Mech Phys Solids*, 62 (2014) 276-294.

## 국문 요약

본 논문에서는 리튬이온 전지의 음극재료 중 하나인 실리콘의 기계적, 전기화학적 성능저하에 대해 연구결과이다. 실리콘의 경우, 현재 상용화된 흑연에 비해 많은 양의 리튬을 흡수 할 수 있어, 이론적인 용량이 매우 크다. 그러나, 많은 양의 리튬흡수로 인한 대변형과 그에 따른 내부응력의 증가로 충전과 방전을 거치는 동안 파단이 발생해, 전기적인 성능저하를 야기시키는 것으로 알려져 있다. 실리콘의 파단이 전기적인 용량에 미치는 영향은 크게 두 가지로, 먼저, 실리콘 입자의 완전한 파단으로 인해 더 이상 리튬과 반응할 수 없는 실리콘 입자의 수를 증가 시키기 때문이고, 다른 이유는 실리콘 내부 파단으로 인해 리튬이온의 불균일성 증가로 인한 표면에서의 전기화학 반응을 조기에 단절 시키는데 있다. 따라서, 실리콘이 리튬흡수 시 일어나는 기계적 거동 및 전기화학적 거동을 예측하고 그에 대한 대안을 제시하는 것이 중요하다.

본 논문의 내용은 크게 세가지로, 첫 번째는 이상화 반응을 하는 실리콘 나노선의 리튬흡수에 따른 응력해석과 그에 따른 파단현상을 모델링 하여 분석하였다. 제안된 모델에서는 비선형 대변형 이론과 Cohesive zone model 을 적용하여 모델을 구성하였다. 이상화 반응을 하는 실리콘은 내부의 급격한 화학적 부피팽창이 실리콘 나노선의 표면을 밀어내면서 외부로부터 크랙이 발생된다. 또한 이런 크랙의 진전 정도는 나노선의 크기에 비례한다. 따라서 이와 같은 해석 결과를 토대로 안정적인 실리콘 나노선의 크기와 크기에 따른 안정적인 리튬 양을 제시하였다.

두 번째는 멀티 스케일, 멀티 피직스 기법을 응용하여, 실리콘 박막의 전기화학 현상을 모델링 하였다. 기존 전기화학 모델의 경우, 충전과 방전 속도에 따라, 실리콘 입자 내 리튬확산 계수를 테일러링(tailoring) 해야 했지만, 실험과 유사한 결과를 얻을 수 있었다. 그러나 본 연구에서 제시한 멀티스케일 모델에서는 이러한 방법을 쓰지 않고,

원자스케일에서 일어나는 현상을 DFT 해석을 통해 업스케일링 하여 리튬확산 현상에 반영하는 방법을 이용해 이러한 비 물리적인 접근법(Non-physics based approach)의 문제점 해결하였다. 제안된 해석방법은 다양한 충방전 속도에서 실제 실험결과와 유사한 경향성을 보여 주었으며, 리튬과 실리콘과의 반응현상을 구체적으로 설명해 준다.

세번째는 패터화된 실리콘 큐브에서의 기계적 및 전기화학적 성능저하 현상을 앞서 제시한 두 모델을 기반으로 구성하고 분석하였다. 패터화된 실리콘에서의 리튬확산 및 전기화학현상은 멀티 스케일/멀티 피직스 모델을 그대로 적용하였고, 내부 균열진전은 Mixed-mode cohesive zone model 에 기반하여 구성하였다. 패터화된 실리콘은 리튬이 들어갈 때 내부에 생기는 Mode I 디본딩에 의해 크랙이 쉽게 발현된다. 그리고 이런 크랙은 리튬 확산의 단절을 야기시켜, 실리콘 내의 리튬이온 분포의 불균일성을 증대 시킨다. 전기화학적 면에서는 리튬이온의 불균일성으로 인한 전기용량의 저하를 일으킨다. 또한 충방전 속도가 빠를수록 크랙의 진전 정도가 크고 이에 따른 전기적인 용량의 저하도 크게 나타난다. 그리고 크랙의 발생은 추가적인 크랙의 진전을 돕기 때문에, 애초부터 크랙이 발생하지 않는 것이 중요하다. 위의 결과를 바탕으로 패터화된 실리콘의 기계적 및 전기화학적 성능을 개선하고자, 바닥에 구멍이 있는 새로운 형상의 패터화된 실리콘을 제시하고 그에 따른 기계적 및 전기화학적 성능을 계산하여 비교 분석하였다.

주요어: 리튬이온전지, 실리콘 음극재, 확산용력모델, Cohesive zone mode, 다차원모델, 전기화학모델, 기계적 성능저하

학번: 2013-30768